Effect of Winglet Integration and Rudder Deflection on Flying-V Aerodynamic Characteristics

Nelson A. Johnson

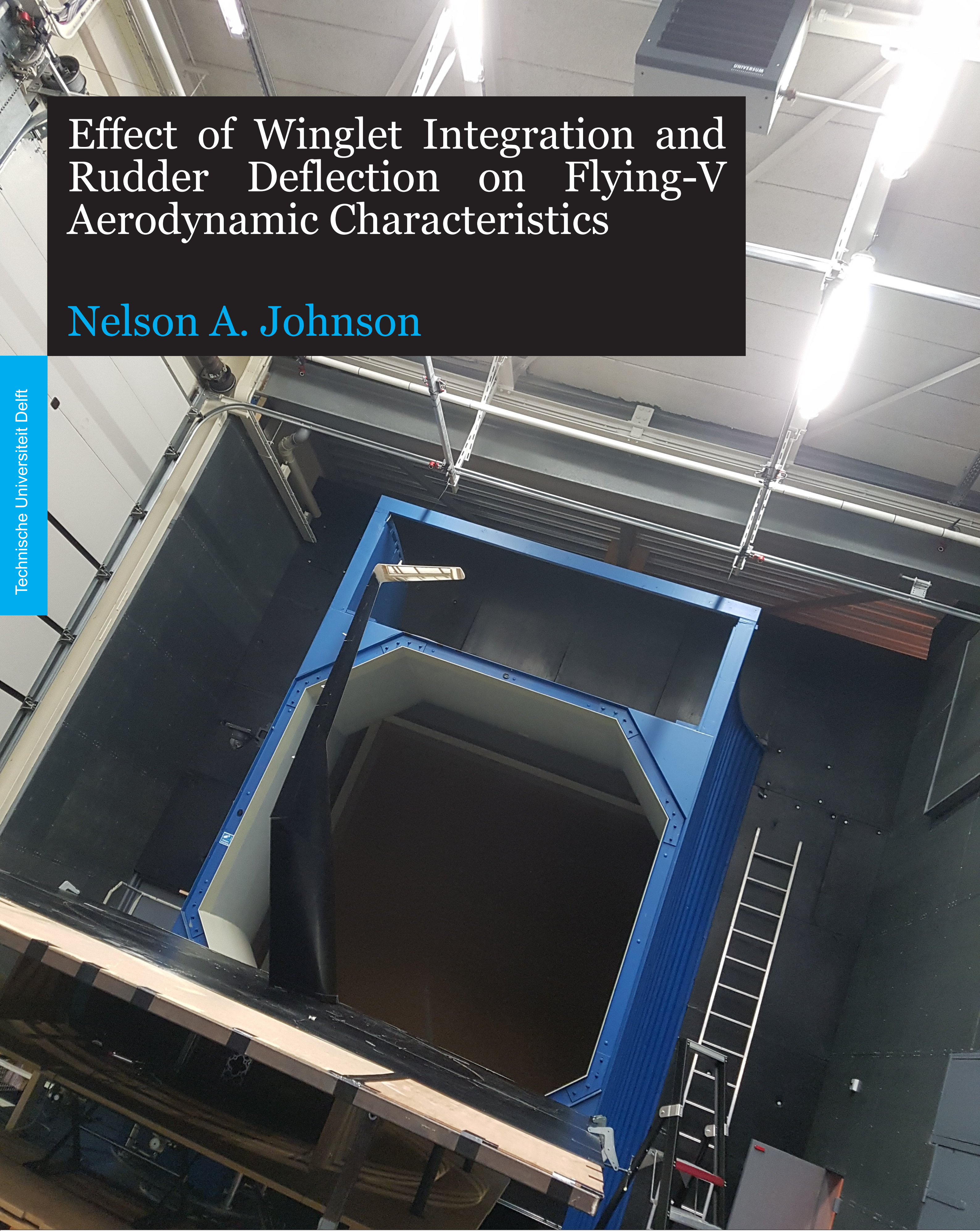

Technische Universiteit Delft

Delft University of Technology

Challenge the future

Effect of Winglet Integration and Rudder Deflection on Flying-V Aerodynamic Characteristics

Master Thesis Report

by

Nelson A. Johnson

to obtain the degree of

Master of Science
in Aerospace Engineering

at
Delft University of Technology,

to be defended publicly on
Tuesday January 19, 2021 at 1:00 PM.

Student number:	4195787	
Duration:	February, 2020 - January, 2021	
Thesis Committee:	Dr.ir. R. Vos,	TU Delft (Supervisor)
	Prof.dr.ir. L.L.M. Veldhuis,	TU Delft
	Dr. F. Avallone,	TU Delft

Summary

The Flying V is an unconventional tailless aircraft concept being researched at TU Delft which has previously been found to have a 25% higher lift-to-drag ratio in cruise than a similar benchmark aircraft. The Flying V was scaled down by researchers to 4.6% to build both a wind tunnel and free flight test model. The wind tunnel model had been successfully tested by a number of researchers but the tip mounted winglet and rudder were not yet installed. Therefore, the aim of this research is to quantify the aerodynamic effects of installing the winglet/rudder combination and deflecting the rudder. Additionally, the change in the rudder effectiveness for various aileron deflections and airspeeds have been quantified.

The wind tunnel model is the left half of the flying wing aircraft and it is mounted vertically in the OJF wind tunnel at TU Delft. There is a reflection plane with an elliptical leading edge at the root of the half-model to split the flow and act as a symmetry plane. The effects of closing two gaps found in the setup were quantified and the data obtained with the gaps open were corrected. The sample standard deviations of the all aerodynamic coefficients were below 0.004 for the dual-wing results and below 0.0029 for half-wing results. Comparison of results from this research project with those of another researcher yielded close results and nearly identical trends.

Without control surface deflections, the winglet integration has been found to slightly increase the lift coefficient by a maximum of about 0.0035 for angles of attack below $10°$ and slightly decrease the lift coefficient by a maximum of about 0.016 for higher angles. The decrease in lift is thought to occur due to high pressure on the newly introduced swept leading edge of the winglet and the winglet promoting separation on the wing's tip region. The winglet has been found to increase the drag of the model by a maximum of about 0.004 until around $28°$ angle of attack. This is thought to be due to the skin-friction and pressure drag of the additional structure. Furthermore, the winglet has reduced the maximum untrimmed lift-to-drag ratio from around 14.4 to 12.3 at $10°$ angle of attack.

The winglet increases the pitching moment acting on the model for most of the tested angles of attack. Considering only the left wing of the model, for angles of attack below $5°$ and above $25°$, the winglet has reduced the side-force acting on the left wing and increased the side-force for angles of attack between these. The results imply that the local flow near the winglet is closely aligned with the winglet chord near $5°$ angle of attack. Below $2.5°$ and above $20°$ angle of attack, the winglet has been found to increase the yawing moment of the left wing while decreasing it between $2.5°$ and $15°$.

Almost all of the rudder deflections have been found to reduce the lift coefficient at all angles of attack, by a maximum of around 0.0024 when considering the left wing. There are only a few conditions in which deflecting the rudder marginally increases the lift. Rudder deflections have been found to increase the drag coefficient at all positive angles of attack, by a maximum of around 0.0024 when considering the left wing. Positive (trailing edge outward) and negative rudder deflections oppositely affect the side-force of the left wing until higher angles of attack. Beyond about $25°$ angle of attack, the smaller three of the four negative rudder deflections have the opposite effect on the half-wing side-force coefficient than desired. The Flying V does not encounter a control reversal condition here because the other wing still generates larger magnitude increments in side-force in the intended direction at these angles of attack. The maximum change in side-force coefficient due to one wing's rudder deflection is around 0.008.

Positive and negative rudder deflections also oppositely affect the rolling moment of the left wing until higher angles of attack. For almost all rudder deflections and angles of attack, both rudder deflection directions increase the pitching moment coefficient. Negative rudder deflections provide larger increases in pitching moment than positive ones. The maximum increase in the aircraft pitching moment due to one rudder is around 0.0035. Finally, positive and negative rudder deflections oppositely affect the yawing moment of the left wing for all angles of attack, as expected. The maximum change to the yawing moment due to one wing's rudder deflection is around 0.004 and positive rudder deflections cause a larger change in yawing moment than negative ones.

With the wing control surfaces at null deflection, the side-force, yawing moment and rolling moment rudder control derivatives have been extracted from the data and linearized. Increases to the angle of attack have been found to significantly reduce the slopes of these control derivatives (effectiveness) in a non-linear fashion. Going from $0°$ to $20°$ AoA yields 49%, 50% and 37% reductions in the side-force, yawing moment and rolling moment rudder control derivatives, respectively.

Positive outboard control surface (CS3) deflections have been found to increase the lift coefficient and negative deflections reduce the lift in all but three CS3 and angle of attack conditions. The largest magnitude change to the lift coefficient due to one wings CS3 deflection is a reduction of around 0.011. For positive angles of attack, positive CS3 deflections always increase the drag coefficient while negative CS3 deflections have been found to reduce the drag of the model for angles of attack above $10°$. This drag imbalance causes an adverse yawing moment on the dual-wing model when the ailerons are deflected. Opposite CS3 deflections have an opposite effect on the half-wing pitching moment coefficient, as intended. One wing's CS3 deflection has been found to increase the pitching moment by a maximum of around 0.016 at $5°$ AoA.

Dual-wing aileron deflections have been found to shift the curves of rudder control derivatives up or down, depending on the sign of the aileron input. The slopes of the control derivatives are largely unaffected by aileron deflections, only decreasing by a maximum of 4.8% with respect to the undeflected case at $10°$ AoA. Increasing the airspeed has been found to moderately increase the rudder effectiveness at low angles of attack. The maximum changes in side-force, yawing moment and rolling moment rudder control derivatives due to airspeed are around 11%, 12% and 32%, respectively.

Acknowledgements

I would like to thank my supervisor, Roelof Vos, for his guidance and feedback through each stage of the thesis work. Thank you for the opportunity to work on such an interesting project. I also would like to thank Jeroen, Sjoerd, Malcom, Alberto, Daniel and Marco. You have all helped me in various ways with the completion of this project. To the technicians in the aircraft hall and the wind tunnel facilities, thank you for your assistance and guidance.

Last but not least, I would also like to thank my parents and family who have always been supportive and encouraging throughout my academic experience.

Nelson A. Johnson
Delft, January 2021

Nomenclature

Acronyms

AoA	Angle of Attack
CAD	Computer Aided Design
CFD	Computational Fluid Dynamics
CS	Control Surface
CS1	Main Wing Inboard Control Surface
CS2	Main Wing Middle Control Surface
CS3	Main Wing Outboard Control Surface
CSD	Computational Structural Dynamics
CSR	Rudder Control Surface
EDF	Electric Ducted Fan
GPS	Global Positioning System
KBE	Knowledge Based Engineering
MDO	Multidisciplinary Design Optimization
MMG	Multi Model Generator
MR	Moment Reference
NACA	National Advisory Committee for Aeronautics
NASA	National Aeronautics and Space Administration
NWL	Winglet Not Installed Configuration
OEI	One Engine Inoperative
OJF	Open Jet Facility (Wind Tunnel)
RANS	Reynolds Averaged Navier Stokes
RC	Radio-Controlled
RSW	Rudder Sweep Test
SFTM	Scaled Flight Test Model
w.r.t.	With Respect To
WL	Winglet Installed Configuration
WLI	Winglet Integration
WTM	Wind Tunnel Model

Greek Symbols

α	Angle of Attack	[°]
$\hat{\alpha}$	Significance Level	[-]
β	Angle of Sideslip	[°]
Δ	Change/Delta Between Variables/Results	[-]
Δ_{Gap}	Gap Effect Used to Correct Open Results	[-]
δ	Control Surface Deflection	[°]
$\overline{\delta}$	Normalized Control Surface Deflection	[%]
ϵ	Wing Section Twist w.r.t $x - y$ Plane	[°]
γ	Confidence Level	[-]
Λ	Sweep Angle	[°]
λ	Taper Ratio	[-]
μ	Population Mean	[-]
ϕ	Winglet Cant Angle	[°]
$\hat{\rho}_{\overline{XY}}$	Correlation Coefficient Between $\overline{X}$ and $\overline{Y}$	[-]
ρ	Atmospheric Density	[kg · m^{-3}]
σ	Population Standard Deviation	[-]

Roman Symbols

A	Aspect Ratio	[-]
b	Wing Span	[m]
c	Chord Length	[m]
$\overline{c}$	Mean Geometric Chord	[m]
C_D	Drag Coefficient	[-]
C_L	Lift Coefficient	[-]
C_l	Aerodynamic Rolling Moment Coefficient	[-]
C_m	Aerodynamic Pitching Moment Coefficient	[-]
C_n	Aerodynamic Yawing Moment Coefficient	[-]
C_Y	Side-Force Coefficient	[-]
D	Drag Force	[N]
e	External Balance Error	[%]
F	Force	[N]
h	Cruise Altitude	[km]
K	Winglet Induced Angle Constant of Proportionality	[rad]
L	Lift Force	[N]
l	Aerodynamic Rolling Moment	[N · m]

M	Moment	[N · m]
m	Aerodynamic Pitching Moment	[N · m]
Ma	Mach Number	[-]
N	Sample Size	[-]
n	Aerodynamic Yawing Moment	[N · m]
P	Static Pressure	[Pa]
p	Right Tail Probability	[-]
q	Dynamic Pressure	[Pa]
R	Reference Frame	[-]
S	Wing Area	[m^2]
s_N	Sample Standard Deviation	[-]
T	Test Statistic	[-]
t	Time	[s]
$t_{k,p}$	Critical t Value of Student's t-Distribution	[-]
V	Flow Velocity	[m · s^{-1}]
v_i	Induced Velocity	[m · s^{-1}]
x	X Coordinate	[m]
$\bar{x}_N$	Sample Mean	[-]
Y	Side Force	[N]
y	Y Coordinate	[m]
z	Z Coordinate	[m]

Subscripts

A	Aileron
a	Aerodynamic Reference Frame
b	Body Reference Frame
BAL	External Balance Reference Frame
c	Gaps Closed
corr	Corrected Value
f	Final Time (Bias Measurement)
i	Initial Time (Bias Measurement)
IB	Inboard (Wing)
k	Leading Edge Kink
LW	Left Wing
RW	Right Wing

meas	Measurment Time
MR	Moment Reference
o	Gaps Open
OB	Outboard (Wing)
R	Rudder
r	Root
t	Tip
WL	Winglet
x	Along X-Axis
$\overline{X}$	Random Variable Set $\overline{X}$
$\overline{X}+\overline{Y}$	Random Variable Set $\overline{X}+\overline{Y}$
y	Along Y-Axis
$\overline{Y}$	Random Variable Set $\overline{Y}$
z	Along Z-Axis
MAX	Maximum Value

List of Figures

List of Tables

Contents

1 Introduction

In this chapter, the motivation for the Flying V aircraft configuration is first discussed in Section 1.1. Next, the Flying V design and previous analyses are summarized in Section 1.2. Background information on winglet design and analysis is given in Section 1.3 and the research objectives and questions for this project are explained in Section 1.4. Finally, the report structure is briefly described in Section 1.5.

1.1. Unconventional Aircraft Configurations

Throughout history, different types of aircraft configurations have been investigated by aerospace engineers. The main configuration types include the canard (such as the Wright Flyer), tailless and conventional configuration types. For a canard aircraft, the horizontal stabilizer is positioned in front of the main wing while tailless aircraft do not possess a horizontal stabilizer. Canard and tailless aircraft are most prevalent in the civil and military sectors of the aircraft industry. In the commercial transportation sector, most aircraft in operation are of the conventional configuration, consisting of a tubular fuselage with cantilevered wings and aft mounted tails. The conventional configuration dates back to the Boeing B47 aircraft, after which, engineers started their designs from a similar concept [6]. For the conventional configuration, the average lift-to-drag ratio has increased over 30%, the specific fuel consumption reduced by around 50% and the structural weight reduced by about 40% through innovations made since the dawn of the jet airliner [6]. However, the performance improvements of the conventional configuration now seem to be approaching an asymptote and are hardly increasing [6]. This has given rise to the design and analysis of unconventional aircraft configurations which can meet stricter regulation and performance goals [6]. Blended wing body (BWB) aircraft seem to be a viable alternative aircraft configuration and have been estimated to increase the maximum lift-to-drag ratio by around 20% relative to that of the conventional configuration [7]. However, various aircraft designers believe that the ultimate aircraft configuration consists of only a pure wing and the BWB has not completely removed the fuselage body [8].

1.2. The Flying V

The Flying V is an unconventional aircraft configuration proposed by Justus Benad during an internship project at Airbus [1]. The Flying V consists of a highly swept inboard wing segment connected to a less swept outboard wing segment with winglets attached to it shown in Figure 1.1. The layout stems from the idea to connect two cylindrical fuselage pressure vessels for passenger seating at the wing root and allow them to travel aftward within the swept inboard wings [1]. A wing section view of the concept parallel with the flow direction in Figure 1.2 reveals an efficient use of volume within the wing due to the sweep angle of the inboard wing and circular fuselage. Since the pressurized section is nearly circular, a large weight penalty is not expected [1].

The Flying V concept was sized for 315 passengers in a dual-class seating layout and was found to reduce the structural mass by 2% and increase the aerodynamic efficiency by 10% with respect to a reference Airbus A350-900 [1]. The internal volume of the aircraft is efficiently used by positioning the passenger and cargo compartments within the wings [1]. Since the release of Benad's report, faculty and students at TU Delft became involved in the Flying V project and this is briefly discussed in the next sections.

Figure 1.1: The Flying V by Justus Benad [1]

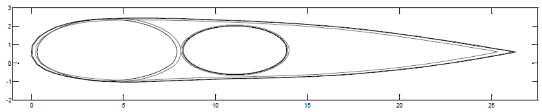

Figure 1.2: Proposed Profile in the Streamwise Direction Showing Front Cabin and Aft Cargo Hold. [1]

1.2.1. Further Aerodynamic Design

Impressed with the potential aerodynamic and weight improvements found by Benad, Faggiano focused on assessing and improving the aerodynamic performance of the Flying V concept in a cruise condition of $Ma = 0.85$, $C_L = 0.26$, $h = 13$ km [2, 9]. A feasible design space was first explored using the SU2 flow solver to reduce induced drag, pitch down, supersonic flow and to improve the isobars [2]. The baseline configuration was parameterized, sized to meet a number of requirements, meshed, analyzed by a flow solver and successively improved [2]. This was performed using the ParaPy Knowledge Based Engineering framework which allows the creation, CAD display, and automated manipulation and analysis of products through the Python coding language. Rules and constraints may all be programmed into the KBE application and the Flight Performance and Propulsion Department has made a KBE app called the Multi Model Generator (MMG) to develop, analyze and modify unconventional aircraft.

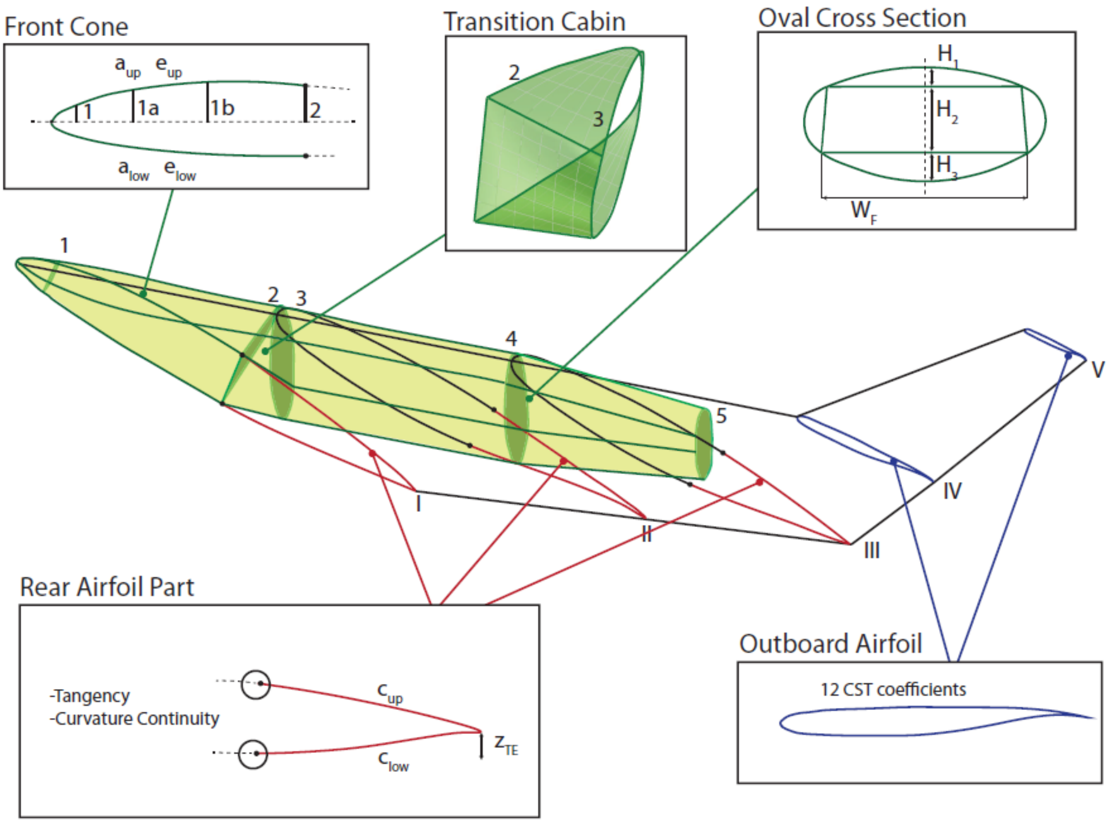

Figure 1.3: The Flying V Parametrization [2]

Faggiano utilized a single oval fuselage concept within the Flying V design shown in Figure 1.3 instead of two separated passenger and cargo bays like Benad [2]. In relation to to the NASA common research model (a modern long-range airliner benchmark), the resulting design of Faggiano is 25% more efficient at the cruise condition [2]. Faggiano's Preliminary Flying V design yields a lift-to-drag ratio at cruise of 23.7 and the planform is shown in Figure 1.4 compared to Benad's conceptual design [2]. The preliminary aerodynamic design derived by Faggiano is used in the current research projects at TU Delft and will be referred to as the full-scale Flying V. Pascual performed research on the effect of various engine positions and orientations on the cruise performance of the full-scale Flying V using numerical simulations in Ref. [10].

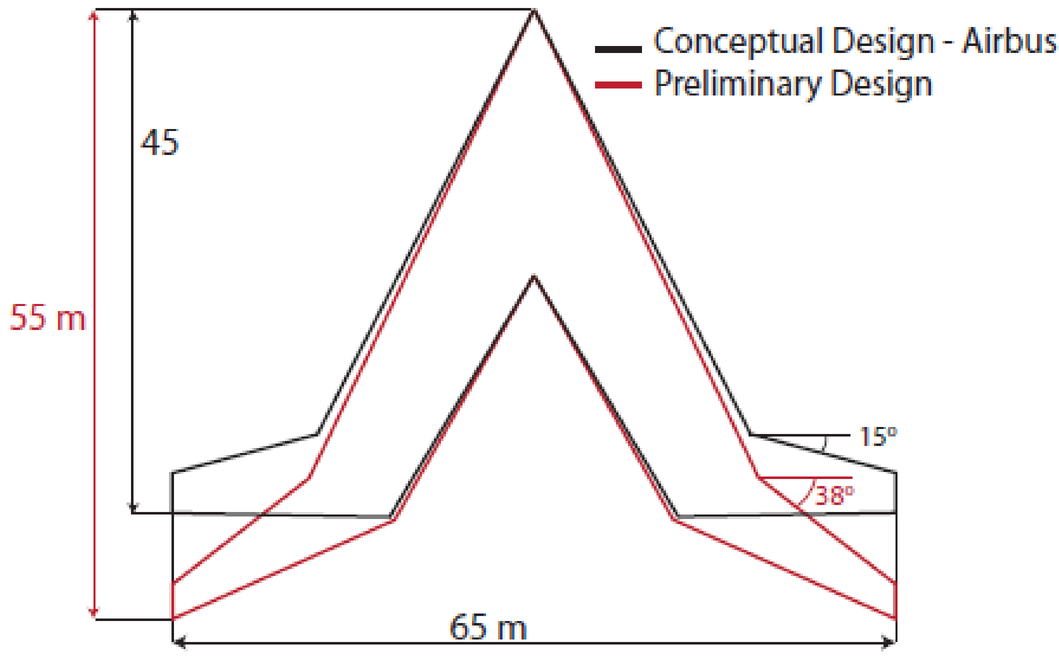

Figure 1.4: Faggiano's Preliminary Flying V Design Compared to Benad's Conceptual Design [2]

1.2.2. Wind Tunnel Testing

The preliminary Flying V shape derived by Faggiano in Ref. [2] was scaled to 4.6% using Froude scaling laws so that a model can be used for wind tunnel testing by Palermo and Viet in Refs. [11, 12]. Palermo and Viet constructed a half-wingspan model at this 4.6% scale factor and placed it in the TU Delft Open Jet Facility to quantify the low speed aerodynamic performance and determine the flight mechanics behavior of a flight test model of the same scale [11, 12]. Since the Flying V is tailless, the moment reference (MR) position will influence the required elevator deflection to trim and thus the maximum achievable lift coefficient. The trailing edge control surfaces have been sized by Palermo in Ref. [11] and deflected in the wind tunnel campaign. Palermo found the moment reference (center of gravity) position for the scaled flight test model to achieve the maximum trimmed lift coefficient and at this position, the maximum trimmed lift-to-drag ratio is 10.4 [11]. A flight mechanics analysis for the scaled flight test model in a power-off condition has also been constructed in Ref. [11]. Furthermore, Palermo performed RANS CFD simulations using various meshes of the wing in the same flow conditions as the wind-tunnel model. The lift coefficient results were in good agreement with the experiment but the pitching moment results were not [11]. Palermo recommends additional wind-tunnel campaigns to quantify integration effects of landing gear, engines and winglets [11]. Viet found similar results to those of Palermo, both measuring an unstable pitch break around $20°$ angle of attack [11, 12]. Furthermore, Viet performed flow visualization with smoke, tufts and oil flow showing vortex separation and attachment behavior changing with angle of attack [12].

Ruiz Garcia created an aerodynamic model identification using wind tunnel data which can be used to find the forces and moments acting on the Flying V scaled model at any flight condition within the model's region of validity [13]. This model is a helpful tool for the flight testing team as it can be used for flight control system design, takeoff calculations, etc [13]. Additionally, Ruiz Garcia investigated the implementation of lift interference and blockage corrections on the wind tunnel data in Ref. [13]. Due to questionable assumption validity or negligible effects on the results, the corrections were neglected until additional flight and/or wind tunnel test data are obtained [13]. Finally, Van Empelen used the scaled wind tunnel model with an electric ducted fan (EDF) installed to quantify the interference effects due to engine installation in Ref. [14].

1.2.3. Scaled Flight Test Model

With the same geometry as the the 4.6% scale Flying V wind tunnel model, a scaled flight test model (SFTM) is under development by faculty at TU Delft. The wingspan is 3 meters and its structure consists of a glass fiber skin locally stiffened with foam core sandwich panels for ribs and spars. Instrumentation is mounted to the internal structure using multiplex wood, mechanical fasteners and epoxies. The SFTM has a pitot tube emanating from its nose-tip and the aircraft will use a Pixhawk PX4 flight controller with GPS, accelerometer and magnometer sensors. The model is being manufactured with tight tolerances using a FARO 3D measurement arm and it will be piloted from the ground by a skilled radio-controlled (RC) pilot with a standard RC transmitter.

1.2.4. Conclusions of Previous Research

The main conclusions from the wind tunnel test campaign of Palermo in Ref. [11] are that there is a presence of vortex lift and and unstable pitch break. Furthermore, since the control surfaces do not suffer from drastic loss of effectiveness throughout the angle of attack range tested ($-10° \leq \alpha \leq 35°$), the Flying V does not have deep stall tendencies [11]. For angles between $-10°$ and $20°$, the aerodynamic center was found to be between 1.42 m and 1.32 m aft of the nose. The most forward and most aft allowable moment reference position limits for the scaled flight test model have been found at 1.33 m and 1.39 m, respectively [11]. While maintaining slight static stability and using the two inboard control surfaces as elevators, the optimal moment reference to maximize the achievable lift coefficient has been found at a position 1.336 m aft with respect to the nose [11]. The corresponding maximum lift coefficient is 0.7 and the maximum trimmed lift-to-drag ratio was found to be 10.4 [11]. The reduction of (elevator) control authority was found to generally reduce the maximum achievable lift coefficient of the Flying V [11]. Finally, the experimental results were compared to those from numerical CFD simulations with different grids [11].

The oil flow visualization by Viet in Ref. [12] showed that the wing exhibits a combination of cross-flow, attachment and separation lines on the wing's surface which change with angle of attack. Beyond $11°$ angle of attack, a leading edge separated vortex is formed at the kink in the leading edge and spreads over the outboard wing [12]. Beyond $13°$, a set of vortices was identified over the inboard wing, flowing from root to tip which were thought to cause the vortex lift behavior [12]. Beyond $22°$, the inboard wing vortices were found to form a stable leading edge vortex and this was confirmed with smoke visualization outside of the boundary layer [12]. Viet also calculated the moment reference position limits for the SFTM and they were similar to those found by Palermo [12].

Ruiz Garcia used wind tunnel data to construct a model which can determine the aerodynamic forces and moments of the Flying V at any flight condition inside the region of validity of the model [13]. The effect of thrust was included in the model, updated moment reference position limits were found and the planned moment reference position for the SFTM was updated to be 1.36 m.

Finally, in the wind tunnel test campaign of Van Empelen, the isolated performance of the electric ducted fan to be used on the SFTM were measured, as well as the interference effects due to engine integration onto the wind tunnel model [14]. The powered engine was found to increase the lift coefficient by 400 counts at full thrust and $10°$ angle of attack [14]. At 20 m/s and angles of attack above $5°$, the engine operation was found to have a detrimental effect on the drag, with a maximum penalty of 60 counts at full thrust and $10°$ angle of attack [14]. However, at 15 m/s and angles above $10°$, the drag is reduced due to interference with a maximum reduction in drag coefficient of 100 counts at $20°$ [14].

1.3. Winglet Design and Analysis

Winglets are a way to reduce the induced drag of an aircraft without increasing the aspect ratio (span) [15]. For swept and delta wing planforms, winglets can also be installed on wingtips to provide directional stability (like the Flying V) [16]. Installing a winglet on the wingtip of an existing wing will change the spanwise circulation distribution along the span and thus the downstream trailing edge vortex structure [15]. The reduction of induced drag could be found by analyzing the wake, or Treffetz plane and this shows that a properly designed winglet diffuses the tip vortex, just aft of the wingtip [4, 15, 16]. The exact details of the aerodynamic phenomena leading to the benefits are difficult to explain and CFD is often used to analyze the winglet flow field and optimize the winglet design [17]. The Reynolds number has a large impact on the flow field near the winglet and there hasn't been an effective correlation between low Reynolds wind tunnel tests and high Reynolds number flight tests [17].

In 1887, the idea of placing vertical surfaces at the wingtips to reduce induced drag was patented by Lanchester and this led to a number of theoretical and experimental analyses of end plates on wingtips [16]. Richard Whitcomb realized in Ref. [16] that the vertical surface at the wingtip must *efficiently* produce significant side forces, even at supercritical conditions. As these end plates turned into small wings, it led to the term winglets being used to describe them [16]. The effect of the winglets on the overall aircraft performance must consider the impact of their installation on the structural weight [16]. Thus, in Ref. [16], the objective was to obtain a larger decrease in lift induced drag using a winglet than from using a wingtip extension for the same additional bending moment.

In the 1970s, theoretical calculations and iterative experimental analysis were mainly used to design the winglets [16]. These winglet integration wind tunnel studies focused on high Reynolds number flows and some examples can be found in Refs. [3, 4, 18–23]. Later, panel methods were used in the early design phase to develop winglets for induced drag reduction, using wind tunnel testing to validate profile and wave drag predictions [24]. Then, structural issues such as increased weights and flutter characteristics would be considered sequentially [24]. Due to the advancement of CFD, computational structural dynamics (CSD) and multidisciplinary design optimization (MDO), there are currently more tools available to the designer [24]. Modern approaches to winglet design, as explained in Refs. [24, 25] use aircraft parameterizations and CFD codes to iteratively design and analyze the winglet and wind-tunnel tests to validate these designs. In Ref. [17], an inverse design method is used to design the winglet such that the aircraft has an idealized spanwise load distribution for minimum drag. Furthermore, a winglet design methodology using the vortex lattice method for low speed UAVs can be found in Ref. [26]. In the remaining part of this section, a simplified flow field will be considered to explain general winglet integration effects and design guidelines found experimentally by Whitcomb in Ref. [16].

Due to the pressure difference between the upper and lower surfaces of the main wing, there is an induced velocity around the wingtip shown in the top of Figure 1.5a causing a tip vortex. These induced velocities have largest magnitude just outside the boundary layer and toward the wingtip [15]. The effective velocity seen by the winglet is the vector sum of the freestream velocity (V) and the induced velocity (v_i) shown in the bottom of Figure 1.5a. This vector sum causes the winglet to operate at an angle of attack while the aircraft in straight, non side-slipping flight. Furthermore, when one looks at the resultant force on the winglet due to the effective velocity acting on it, one can see that it is tilted forward, ultimately causing a thrust force or a negative drag increment. The winglet is effectively acting as a sail [17]. In addition to the negative drag/sail effect of the winglet, the tip vortex strength is also reduced, further reducing induced drag [17]. However, as the winglet may cause increases in the wing root bending moments and the viscous drag, a trade-off in the winglet design exists [17]. In the next paragraphs, the drag contribution of the winglet is derived in Equations 1.1 through 1.7.

$$-\,\mathrm{d}D = \mathrm{d}L_{\mathrm{WL}}\alpha_{\mathrm{WL}} - \mathrm{d}D_{\mathrm{WL}} \tag{1.1}$$

$$\Delta D = -L_{\mathrm{WL}}\alpha_{\mathrm{WL}} + D_{\mathrm{WL}} \tag{1.2}$$

$$\Delta C_D = -\frac{S_{\mathrm{WL}}}{S}\left(C_{L_{\mathrm{WL}}}\alpha_{\mathrm{WL}} - C_{D_{\mathrm{WL}}}\right) \tag{1.3}$$

$$C_{D_{\mathrm{WL}}} = C_{D_{0,\mathrm{WL}}} + \frac{C_{L_{\mathrm{WL}}}^2}{\pi A_{\mathrm{WL}}} \tag{1.4}$$

$$\Delta C_D = -\frac{S_{\mathrm{WL}}}{S}\left(C_{L_{\mathrm{WL}}}\alpha_{\mathrm{WL}} - C_{D_{0,\mathrm{WL}}} - \frac{C_{L_{\mathrm{WL}}}^2}{\pi A_{\mathrm{WL}}}\right) \tag{1.5}$$

$$C_{L_{\mathrm{WL}}} = 2\pi\frac{A_{\mathrm{WL}}}{A_{\mathrm{WL}}+2}\alpha_{\mathrm{WL}} \tag{1.6}$$

$$\Delta C_D = -\frac{S_{\mathrm{WL}}}{S}\left[2\pi\left(\frac{A_{\mathrm{WL}}}{A_{\mathrm{WL}}+2}\right)^2 K^2 C_L^2 - C_{D_{0,\mathrm{WL}}}\right] \tag{1.7}$$

Considering the winglet section in Figure 1.5b and assuming small induced angles of attack at the winglet, the negative drag component or thrust force due to the winglet can be expressed in Equation 1.1. Note that the α_{WL} terms in this section are small angle approximations of the 'sin()' term associated with the winglet lift of Figure 1.5b in radians. In this section, the subscript 'WL' denotes the winglet quantities. Assuming an average induced velocity across the winglet yields Equation 1.2 and 1.3 in coefficient form. Using the relation between the lift and drag coefficient in Equation 1.4 yields Equation 1.5. Furthermore, assuming the induced angle is proportional to the lift coefficient ($\alpha_{\mathrm{WL}} = KC_L$) and by assuming the lift curve slope of the winglet follows the relation in Equation 1.6, the change in aircraft drag due to the winglet can be approximated with Equation 1.7 as a function of the aircraft lift coefficient. Note that the winglet lift in Equation 1.6 is in the winglet reference frame which translates to a side-force in the aircraft reference frame. This process is explained in Ref. [15].

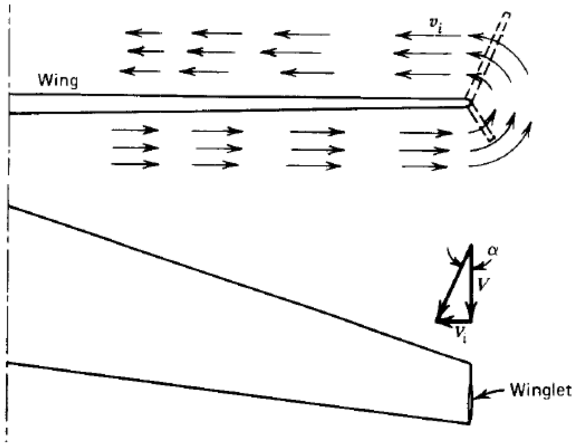

(a) Rear and Top Views of Planform Illustrating the Flow Field into Which the Winglet is Placed [15].

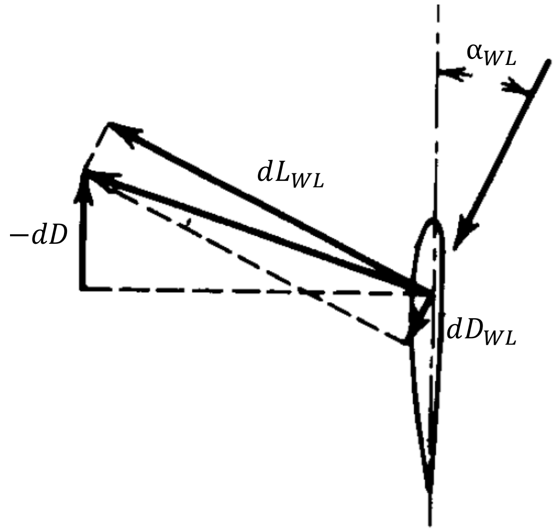

(b) Forces Acting on the Right Wing's Winglet [15].

Figure 1.5: Winglet Flow Field and Forces Acting on the Winglet Section.

Equation 1.7 shows that the aircraft drag coefficient due to the winglet (ΔC_D) decreases in a linear fashion with the square of the aircraft lift coefficient (C_L^2). Furthermore, at low lift coefficients, the change in aircraft drag coefficient is positive, due to the winglet's zero-lift drag coefficient ($C_{D_{0,\mathrm{WL}}}$). Thus, the winglet zero-lift drag coefficient must be minimized. Higher winglet aspect ratios (A_{WL}) are desired to maximize the winglet lift-curve slope and minimize its induced drag. The winglet should be installed as far aft along the wingtip chord as possible to experience the largest induced velocities for a given lift coefficient [15]. Also, winglets are expected to be more effective in reducing induced drag for highly tip loaded wings [15]. From Equation 1.7 it would appear that an increased winglet aspect ratio (A_{WL}) will always lead to a reduction in C_D, but this is not the case because the constant of proportionality (K) will decrease with increasing A_{WL} [15]. There is a similar phenomena for increasing S_{WL}/S.

As mentioned, Whitcomb compares the benefits of winglets to that of wingtip extensions for the same additional wing root bending moments In Ref. [16] by analyzing theoretical calculations and experimental results. The investigations found that placement of the winglet more aft along the wingtip chord will minimize the interference effects due to the superposition of the inner winglet surface and upper wing surface supervelocities, especially in supercritical conditions [16]. However, the corresponding reduced winglet root chord reduces its effectiveness and the structural attachment of the winglet wing-box to that of the main wing becomes a problem, so there again exists a trade-off [16]. To maximize the winglet's aerodynamic efficiency, it should be tapered to obtain a constant normal force coefficient along the winglet span [16]. The most satisfactory results were obtained with the winglet operating at normal force coefficients limited to the same order of magnitude as the lift coefficients of the wing [16]. Furthermore, the effective sweep of the winglet should be approximately the same as the wing for satisfactory winglet effectiveness at supercritical conditions [16].

The winglet airfoils should be chosen to efficiently generate the inward normal forces at the design lift coefficient and Mach number [16]. For supercritical design conditions, the cambered airfoil shape is designed to avoid a strong shock wave on its surface and to minimize the additional induced velocities imposed on the outboard wing [16]. Furthermore, the winglet airfoil should be chosen such that significant boundary layer separation is delayed until conditions where there is such separation on the wing [16]. This objective should be met for low speed flight conditions with high-lift devices extended [16]. The winglet thickness-to-chord ratio should be minimized without degrading the low-speed stall characteristics or causing a large weight penalty to maximize the high speed performance [16].

The winglet is most often toed-out because the effective winglet inflow angle of attack in Figure 1.5b is greater than that required to generate the desired normal force coefficient at the design condition [16]. The desired spanwise load distribution with a swept wing in an undistorted flow field requires geometric twist, however, since the inflow angle reduces along the winglet height, this approximately provides the required aerodynamic twist [16]. Finally, the winglet cant angle must also be chosen from a trade-off including induced drag reduction, wing root bending moments and skin-friction [16]. Outward cant will reduce the flow interference effects from the winglet and wing, especially at supercritical conditions [16].

For a first-generation transport aircraft operating near its design condition of $Ma = 0.78$ and $C_L = 0.44$, an increase in lift-to-drag ratio of around 9% and a reduction of induced drag of about 20% with respect to the baseline planar wing was found experimentally by Whitcomb in Ref. [16]. The improvement in lift-to-drag ratio is more than twice that of the wingtip extension for the same increase in wing root bending moment [16]. The overall performance benefit due to the winglets with respect to the wingtip extensions is found to be significantly dependent on the winglet incidence angle and the corresponding loads on the winglet and outboard wing section [16]. Finally, washout of the wing has been found to diminish the benefits of both the winglet and wing tip extensions in Ref. [27]. As previously mentioned, it is not an objective of the current study to design the winglet, only to document the installation effects of the existing one.

In Ref. [3], winglets were found to slightly increase the lift coefficient (and lift-curve slope) and reduce the pitching moment for a first generation jet transport at various Mach numbers. This is shown in Figure 1.6a for the design Mach number of 0.78. The longitudinal instability is also slightly reduced with the addition of the upper winglet [3]. The kinks in the lift and pitching moment curves correspond to increases in boundary layer separation on the wing, offloading the outboard wing behind the moment reference location [3]. For lift coefficients above 0.2, the reduction of induced drag outweighs the increase in skin-friction and form drag due to the winglet integration [3]. Beyond this lift coefficient, the reduction in drag coefficient increases with lift and this is shown in Figure 1.6b. Finally, winglets and wingtip extensions have been found to slightly increase the wing root bending moment by around $3 - 4\%$ near the design lift coefficient [3].

Similar results have been found in Ref. [4] for a second generation jet transport shown in Figures 1.7a and 1.7b. Note that in Ref. [4], the results are for an aircraft with both upper and lower winglets. These winglets also slightly increase the lift coefficient and this is due to the winglets increasing the outboard wing section's normal force coefficient [4]. Near the cruise lift coefficient of 0.53, the pitching moment coefficient after winglet integration is reduced by about 0.008 in Figure 1.7b [4]. Furthermore, the aircraft is more stable with the winglets (more negative sloping C_{m_α}) and at low lift coefficients, the (zero-lift) pitching moment coefficient is slightly increased [4]. The increase in zero-lift moment coefficient was attributed to the winglet reducing the outboard wing section lift coefficient with respect

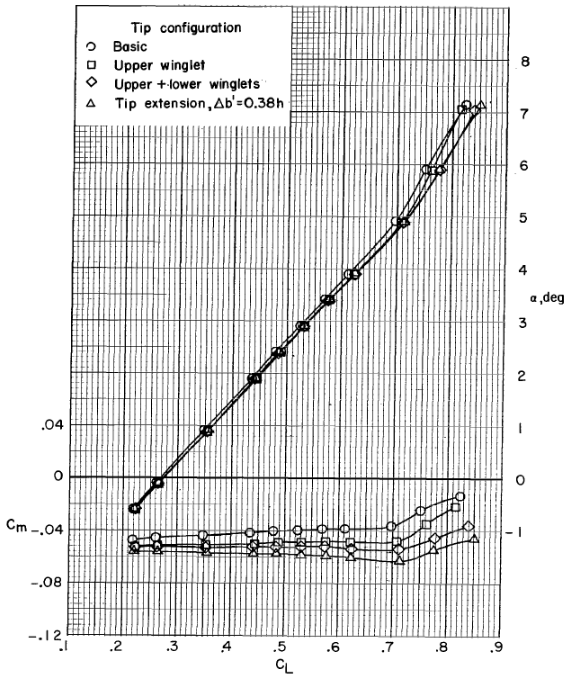

(a) Variation of Pitching Moment Coefficient and Angle of Attack with Lift Coefficient for a First Generation Jet Transport at $Ma = 0.78$ [3].

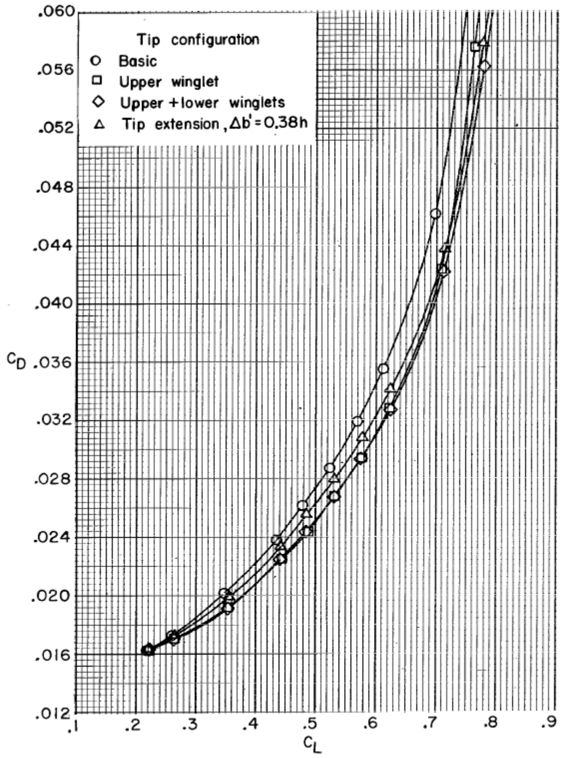

(b) Variation of Drag Coefficient with Lift Coefficient for a First Generation Jet Transport at $Ma = 0.78$ [3].

Figure 1.6: Pitching Moment Coefficient, Lift Coefficient and Drag Coefficient Variations With Lift Coefficient for a First Generation Jet Transport With Various Wing Tip Devices at $Ma = 0.78$ [3].

to the baseline wing in Ref. [4]. The winglet installation was found to increase the wing root bending moment by 1.4% at the design lift coefficient, and no more than 2% for higher lift coefficients shown in Figure 1.7b [4]. The increases in wing root bending moment are attributed to the increased tip loading of the wing and the substantial side forces on the winglet [4]. Finally, the incremental drag coefficient due to the winglet integration is shown for three Mach numbers in Figure 1.8 [4]. At low lift coefficients, the additional form and skin-friction drag increase the total drag coefficient [4]. At the design lift coefficient, the winglet integration has reduced the drag coefficient with respect to the baseline aircraft by 0.0015, and the drag reduction increases with higher lift conditions [4]. Since the lift and drag coefficients change for each AoA after winglet integration, this rotates the drag polar and there is now a higher optimum cruise lift coefficient (or AoA) [4].

1.4. Research Objective

As mentioned before, the previous wind tunnel experiments in Refs. [11–14] occurred using a model which did not have the winglet and rudder attached. Thus, the objective of this research project is to quantify the effects on the aerodynamic behavior of the Flying V aircraft due to the integration of the winglet and deflection of the rudder control surface by carrying out a wind tunnel test campaign. This objective may be split into sub-goals described in the next paragraph. Finally, the research questions are given in the final paragraph.

The sub-goals of this research project are to gather aerodynamic coefficient data using the Flying V wind tunnel model both with and without the winglet installed. Also, aerodynamic coefficient data for the wind tunnel model with various main wing and rudder control surface deflections are to be found. The next goals are to verify the data's validity and then to compare the various experimental results to answer the research questions. The research questions are given in the list below and have been derived to solve the research objective.

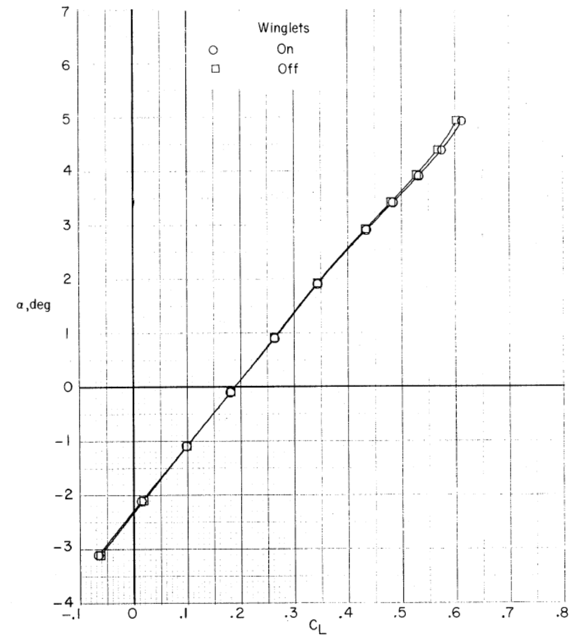

(a) Variation of Angle of Attack with Lift Coefficient for a Second Generation Jet Transport at $Ma = 0.8$ [4].

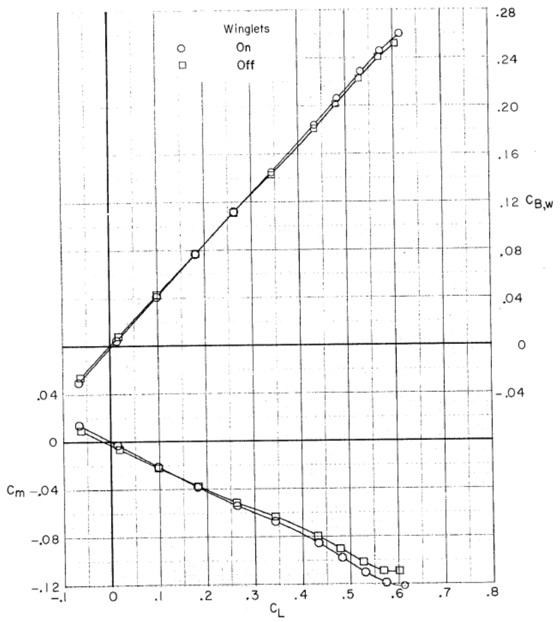

(b) Variation of Wing Root Bending Moment and Pitching Moment Coefficients with Lift Coefficient for a Second Generation Jet Transport at $Ma = 0.8$ [4].

Figure 1.7: Wing Root Bending Moment and Pitching Moment Coefficient Variations With Lift Coefficient for a Second Generation Jet Transport With and Without Winglets at $Ma = 0.8$ [4].

1. How does the winglet integration influence the aerodynamic coefficients?
2. How does the rudder deflection influence the aerodynamic coefficients?
3. What is the impact of the outboard control surface deflection on the rudder effectiveness?

1.5. Report Structure

The research methodology is described in Chapter 2 which includes a description of the wind tunnel model and sign conventions in Section 2.1. Next, the wind tunnel setup is described in Section 2.2 with the aerodynamic force and moment derivation given in Section 2.3. The tested configurations and testing strategy are explained in Sections 2.4 and 2.5, respectively. Finally, the method used to account for measurement bias is explained in Section 2.6.

In Chapter 3, the verification and validation activities are discussed. First, the method to correct for the effects of gaps found in the wind tunnel setup are described in Section 3.1. The maximum standard deviations of the results are presented in Section 3.2 and the method used to calculate confidence intervals are given in Section 3.3. The results of this research project are the compared to that of previous researchers in Section 3.4 and the control surface deflection measurements are given in Section 3.5.

The results of this research project are presented in Chapter 4, beginning with the effect of integrating the winglet on the the aerodynamic coefficients in Section 4.1. Next, the effects of deflecting the rudder on the aerodynamic coefficients are given in Section 4.2 with the rudder control derivatives presented in Section 4.3. The effect of the outboard control surface deflections on the aerodynamic coefficients are explained in Section 4.4 and the effect of aileron deflections on the rudder control derivatives are discussed in Section 4.5. Lastly, the effect of changing the airspeed on the rudder control derivatives are given in Section 4.6 and the conclusions and recommendations are given in Chapter 5.

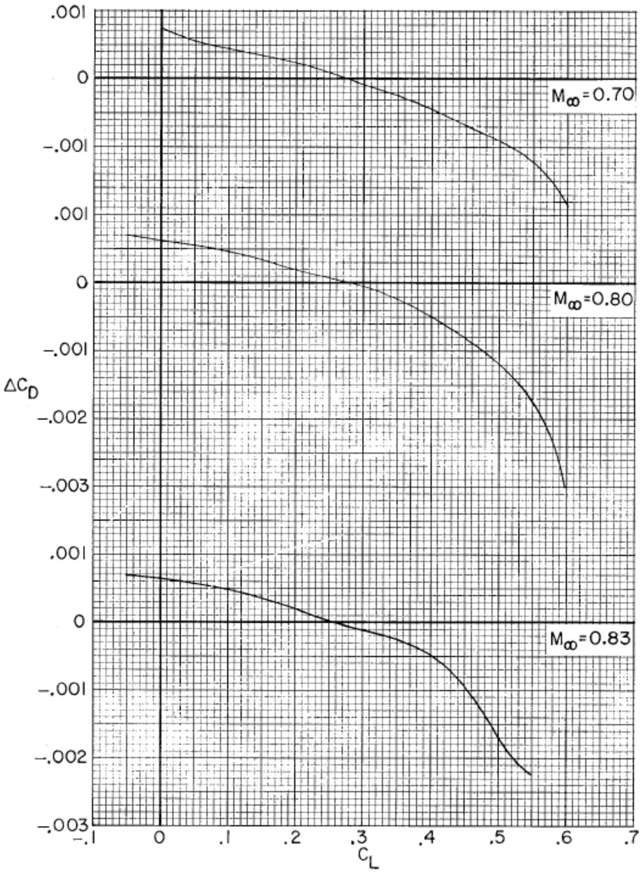

Figure 1.8: Variations of Incremental Drag Coefficient With Lift Coefficient for a Second Generation Jet Transport [4].

2
Research Methodology

This chapter first describes the Flying V wind tunnel model and the sign conventions used in this research project in Section 2.1. Next, the wind tunnel setup and method to calculate the aerodynamic force and moment coefficients are described in Sections 2.2 and 2.3, respectively. The nomenclature of the various tested configurations are explained in Section 2.4 while the testing strategy to answer the research questions is given in Section 2.5. Finally, the methodology to account for the measurement bias for each test case is explained in Section 2.6.

2.1. Flying V Wind Tunnel Model

The Flying V wind tunnel model used in this research project is shown in Figure 2.1. The next subsections will explain the main wing and winglet planform characteristics along with the sign convention.

2.1.1. Main Wing Planform

The Flying V wind tunnel model is a Froude scaled representation of the Flying V designed by Faggiano in Refs. [2, 9] at 4.6% scale. This scale factor was chosen while considering the production of a wind tunnel and flight test model in Ref. [11]. Choosing a larger scale factor reduces flight dynamics frequencies during flight (good for RC pilot), it increases the internal volume making it easier to build and install systems, but it also increases the take-off and landing speed (bad for RC pilot), so there exists a trade-off [11]. The planform geometry of the Flying V wind tunnel model is shown in Figure 2.1. Note that this image is of the right wing, while the wind tunnel model is a left wing. The dimensions for the left and right wings are equal due to symmetry. The inboard wing (IB) is referring to the highly swept ($\Lambda_{\mathrm{IB}} = 64.4°$) wing section and the outboard wing (OB) is referring to the less swept ($\Lambda_{\mathrm{OB}} = 37.8°$) wing section beyond the kink in the leading edge.

The planform variables are given in Table 2.1 and it should be noted that the wingspan indicated extends to the outboard wing section, not the winglet. Figures 2.1 and 2.2 show the additional 17.5 mm in the spanwise direction from the main wing's tip section to the root chord line of the canted winglet. The twist of the wing sections at the root, leading edge kink and wingtip with respect to the $x_{\mathrm{b}} - y_{\mathrm{b}}$ Plane are also given in the table. The sign conventions and explanation of the twist angles are mentioned in Section 2.1.3. It should be noted that the scaled flight test model has a slightly different planform than the wind tunnel model, namely, the outboard wing of the SFTM has been shortened by 16 mm which also causes the winglet to be slightly different size (due to the taper of outboard wing). There is no dihedral applied to the inboard wing, but there is around $5.6°$ of dihedral applied to the outboard wing of the model. This is the angle of the outboard wing's leading edge with respect to the $x_{\mathrm{b}} - y_{\mathrm{b}}$ Plane mentioned in Section 2.1.3 and was measured with the CAD model.

The main wing control surface nomenclature is shown in the left of Figure 2.1. The three main wing control surfaces from the root toward the tip are referred to as CS1, CS2 and CS3, respectively. These control surface dimensions can be seen in the right of Figure 2.1. These are physical measurements made on the model, and are subject to an estimated tolerance of ± 1 mm. The gaps between the control surfaces are about 2 mm wide and are perpendicular to the trailing edge. More details about the sizing of these control surfaces can be found in Ref. [11]. In this research project, either the three main wing control surfaces moved together or the two inboard control surfaces were at null deflections while the third was deflected. The two inboard control surfaces (CS1 and CS2) have been defined to act as elevators with equal normalized deflections in % ($\overline{\delta}_{\mathrm{E}}$). The third control surfaces (CS3) are defined to act as ailerons, with that of the left and right wings moving in opposite directions but to the same normalized deflection in % ($\overline{\delta}_{\mathrm{A}}$). Sometimes only the left or right wing is being considered in this report and it will be clearly indicated if that is the case. The sign conventions and deflection measurements for all control surfaces are described in Sections, 2.1.3 and 3.5, respectively.

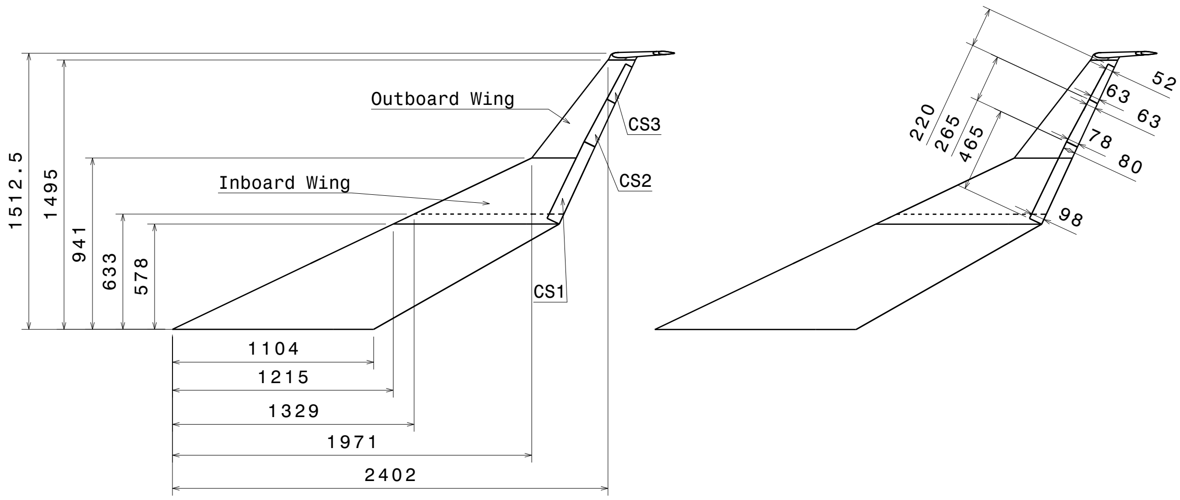

Figure 2.1: Wind Tunnel Model Planform Characteristics. The Mean Geometric Chord is Depicted With a Dashed Line. All Dimensions in mm.

2.1.2. Winglet and Rudder Planforms

The vertical stabilizers were sized for the full-scale Flying V in Ref. [2] to fulfill three main requirements. The first was a requirement of a slightly positive yawing moment derivative, which is a requirement of static directional stability which was estimated using an empirical relation [2]. Dynamic stability was not accounted for in the fin sizing in Ref. [2]. The second requirement for the fin size was to be able to balance a OEI condition for the aft moment reference position at the take-off speed using less than $20°$ of rudder deflection [2]. Here, another empirical relation for the rudder control effectiveness was used in the calculation [2]. The last requirement applied to the sizing of the Flying V vertical stabilizers was to be able to land in a 'maximum crosswind condition' with wind speed of 20% of the take-off speed [2]. This was found to be equivalent to flying at a sideslip angle of $11.5°$ in Ref. [2]. For a given configuration resulting from the planform optimization of Faggiano, the fin with smallest wetted area while fulfilling the mentioned requirements is chosen [2]. The rudder was assumed to span the full stabilizer trailing edge, the rudder chord ratio used was 0.3 and the directional static stability requirement was found to be driving [2]. The vertical stabilizer variables of the full-scale Flying V design include a sweep angle of $36°$, aspect ratio of 2.3, a taper ratio of 0.45 and the NACA 0012 airfoil [2].

The winglet geometry used on the WTM is shown in Figure 2.2 and is slightly different from the one designed for the full-scale Flying V. Also, note that this image is of the right winglet, while the wind tunnel model has a left winglet installed. The dimensions for the left and right winglets are equal due to symmetry. The winglet planform variables used are also listed in Table 2.1; the winglet is not twisted and it is canted 2 degrees outward. The airfoil used on the winglet of the WTM and SFTM is the NACA 0020 because the 0012 was found to be too small to fit servos at this scale factor and there is not a large difference in drag between the two. The winglet interface shape was made in CAD by interpolating between the winglet and outboard wing surfaces with edge tangency. The rudder chord ratio is about 44% and the hinge line is depicted by a red dotted line in Figure 2.2. The hinge line is about 1 mm in front of the rudder spar at the lower rudder section (I) and about 0.5 mm in front of it at the upper

Table 2.1: Flying V Wind Tunnel Model Planform Variables

Item	**Value**	**Units**	**Description**
S	1.869 [11]	[m^2]	Total Planform Area of the Dual-Wing Flying V Scaled Model.
$b/2$	1.495 [11]	[m]	Semi-span of the Flying V Scaled Model.
$\bar{c}$	0.820 [11]	[m]	Mean Geometric Chord.
c_{r}	1.104 [11]	[m]	Root Chord.
ϵ_{r}	1.44	[°]	Root Twist Angle.
c_{k}	0.318 [11]	[m]	Chord Length at LE Kink.
c_{t}	0.145 [11]	[m]	Chord Length at Wing Tip.
Λ_{IB}	64.4 [11]	[-]	Inboard Wing LE Sweep.
ϵ_{k}	-4.3 [2]	[°]	Twist Angle at LE Kink Section.
Λ_{OB}	37.8 [11]	[°]	Outboard Wing LE Sweep.
ϵ_{t}	-4.4 [2]	[°]	Tip Twist Angle.
$c_{\mathrm{r,WL}}$	0.145	[m]	Winglet Root Chord.
λ_{WL}	0.6	[-]	Winglet Taper Ratio.
Λ_{WL}	36.4	[°]	Winglet LE Sweep.
ϵ_{WL}	0	[°]	Winglet Twist Angle.
A_{WL}	2.97	[-]	Winglet Aspect Ratio.
ϕ_{WL}	2.0	[°]	Winglet Cant Angle.

rudder section (II). There is a gap between the winglet and the rudder surfaces shown in Figure 2.2 which decreases in size toward the tip of the rudder. A section view of the winglet depicting the gap as a function of deflection is shown in Figure 2.3. Finally, a fairing was hand made out of foam to terminate the rudder; its shape was manually tuned to to be tangent to the rudder surface and to have it's thickest point at the same chordwise location as the rudder. The selection of the winglet design variables were not part of this research project, but were chosen earlier for the scaled flight test model by the construction engineers. The normalized rudder deflection (in %) is indicated by $\overline{\delta}_{\mathrm{R}}$.

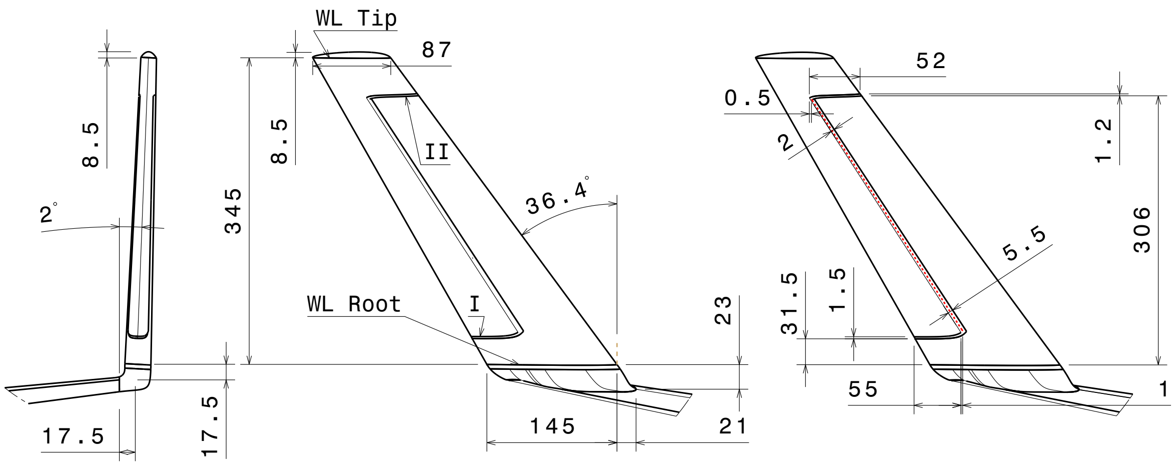

Figure 2.2: Wind Tunnel Model Winglet and Rudder Dimensions (in mm).

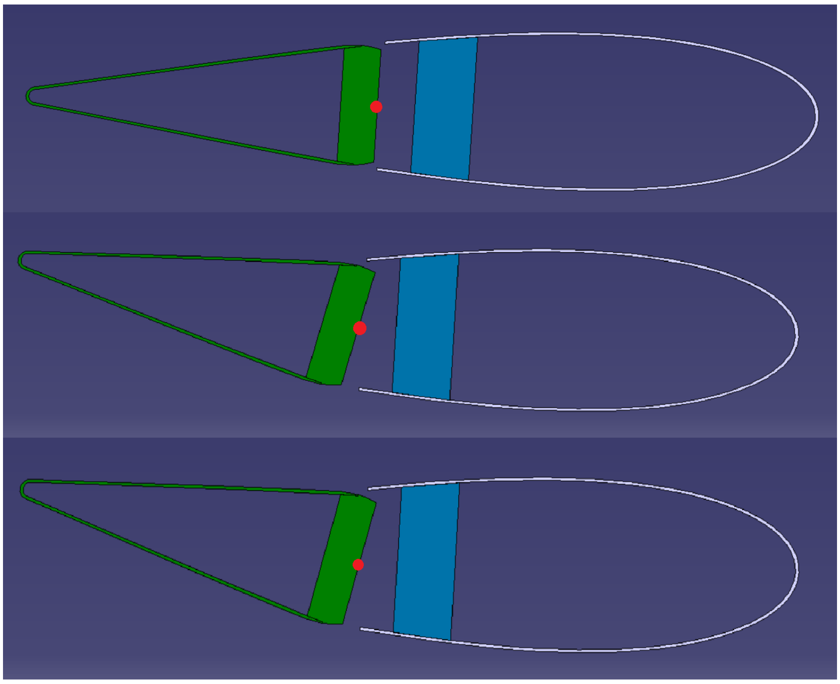

Figure 2.3: Rudder Section View Showing Gaps as Function of Deflection. 0, $15°$ and $23°$ Deflections are Shown from Top to Bottom with the Hinge Line in Red.

2.1.3. Sign Convention

There will be two reference frames used in this research project, the body fixed reference frame (R_{b}) and the aerodynamic (air-path) reference frame (R_{a}), both shown in Figure 2.4. The b and a subscripts define which of the two respective reference frames a certain distance belongs to. The body-fixed reference frame is fixed to the aircraft at a certain reference position and remains fixed during perturbed motions [28]. In this case, the origin for this reference system (moment reference position) is at the proposed center of gravity of the SFTM shown in Figures 2.6 and 2.7. The x_{b} direction is defined to point in the direction of the nose, the y_{b} direction is toward the right wing tip and the z_{b} direction is toward the ground (during flight) [28]. This is a right-handed orthogonal reference system and due to the construction of the Flying V model's (CAD) geometry, the root chord is not in line with the x_{b} axis, but it is at a $1.44°$ angle to it, shown in Figure 2.7. In this research project, the model is defined to be at $0°$ angle of attack when the $x_{\mathrm{b}} - y_{\mathrm{b}}$-Plane in Figure 2.7 is aligned with the tunnel flow direction.

The aerodynamic (air-path) reference frame is linked to the aerodynamic velocity V and has the same origin as the body-fixed reference frame. The x_{a}-axis is in the direction of the aerodynamic velocity and the z_{a}-axis is in the symmetry plane of the aircraft, as shown in Figure 2.4. Finally, the y_{a}-axis is orthogonal to the $x_{\mathrm{a}} - z_{\mathrm{a}}$ plane, completing the right handed orthogonal reference frame [28]. The angles of attack (α) and sideslip (β) denote the orientation of the aerodynamic reference frame with respect to the body-fixed reference frame [28]. It should be noted that the wind tunnel model is not able to be tested in sideslip conditions due to the half-model approach (explained in the next section), so the only variable between the two reference frames is the angle of attack.

Since the model is mounted to the external load balance, the balance is measuring the body (-fixed) forces and moments as the model and balance are rotated over an angle of attack *together*. These (body-fixed) external balance forces and moments must be translated twice, first to the correct moment reference position from the balance center and then onto the aerodynamic reference frame. With the forces and moments described in the aerodynamic frame, the results are expressed in terms of lift, drag, side-force, pitching moment, rolling moment and yawing moments. These transformations of the measured balance forces and moments onto the aerodynamic reference frame will be explained in Section 2.3.

The CS1 and CS2 main wing control surfaces are deflected to *positive* elevator deflections when the trailing edge is deflected down, causing a negative (nose down) pitching moment. A *positive* aileron deflection has the trailing edge down (positive) CS3 deflection on the right wing and the opposite (negative CS3 deflection) on the left, causing a *negative*, right wing up rolling moment [28]. The rudder is deflected to a *positive* angle when the trailing edges are deflected to the left, causing a *negative* yawing moment (nose left) and a positive side force increment (push aircraft to the right) [28]. Since some of the results of this report look at only the left wing, δ_{CS3} is sometimes used to indicate the CS3 position to prevent confusion with the aileron deflection sign. Here, the sign of δ_{CS3} for both wings follows that of the elevator, trailing edge down positive.

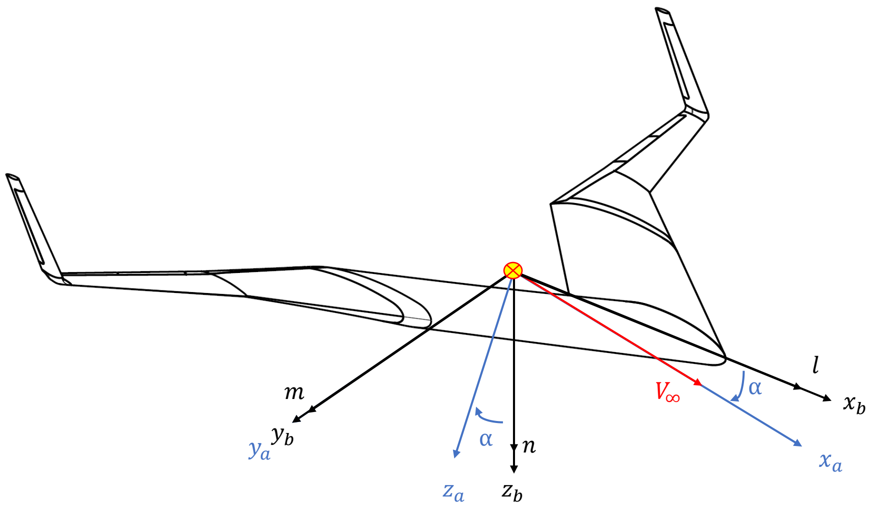

Figure 2.4: Body-Fixed and Aerodynamic Reference Frames, $\beta = 0$. The Rolling, Pitching and Yawing Moments are Indicated with l, m and n, respectively.

2.2. Wind Tunnel Setup

An isometric view of the model mounted to the external balance within the OJF wind tunnel is shown in Figure 2.5. In this figure, the nomenclature of the wind tunnel test components are also given. The OJF exit is shown, with the splitting plate flush with the bottom exit. The reflection plane with an elliptical leading edge is used to simulate a symmetry condition at the wing root. Below the reflection plane, one can see the aerodynamic shield, which is isolating the “L”-shaped boikon connection piece used to connect the model to the load balance from the flow. In Figure 2.6, the shield is hidden and one can see the boikon connection. The ‘attachment plate’ is used to attach the wing to the top of the “L”-shaped boikon connection and is shown in Figure 3.1, from below. In Ref. [14], the aerodynamic shield was found not to cause spillage from under the reflection plane using smoke visualization. The external load balance is mounted to a rotating table which allows the manipulation of the angle of attack.

It is crucial to accurately know where the “balance center” of the load balance is with respect to the aircraft reference position. This is because the balance center is the position at which the measured forces and moments are referenced [5]. Thus, to translate these forces and moments to another position, for example, the moment reference of the SFTM, the relative positions of these locations must be known. The x and y distances from the balance center to the model leading edge (in the body reference frame) are shown in Figure 2.6. Furthermore, the distance from the model leading edge to the reference location used in this text ($x_{MR} = 1.36$ m) is shown.

The offset of the moment reference with respect to the balance center in the z direction is slightly more laborious. Figure 2.7 shows a CAD view from the top of the OJF showing the root section, balance center, moment reference position and two lines. The horizontal purple line is aligned with the $x_{\mathrm{b}} - y_{\mathrm{b}}$-Plane and thus the wind tunnel tunnel when the rotating table is set at 0 degrees and the other black dotted line is aligned with the root chord. Toward the rear of the root section near the suction surface, one can see a green point and this represents the balance center. The point furthest aft in the figure corresponds to the moment reference position, which is 1.36 m aft of the root leading edge, along the $x_b - y_b$-Plane. Thus, the $0°$ angle of attack condition is shown in Figure 2.7 and the root incidence angle at this null angle of attack is around $1.44°$. Finally, the z distance from the moment reference position to the balance center is 8 mm. Note that this z distance (and aerodynamic moment coefficients) will change if the reference position is chosen along the chord line instead. These distances will be used in the next section to translate the measured forces and moments from the balance center to another point on the model.

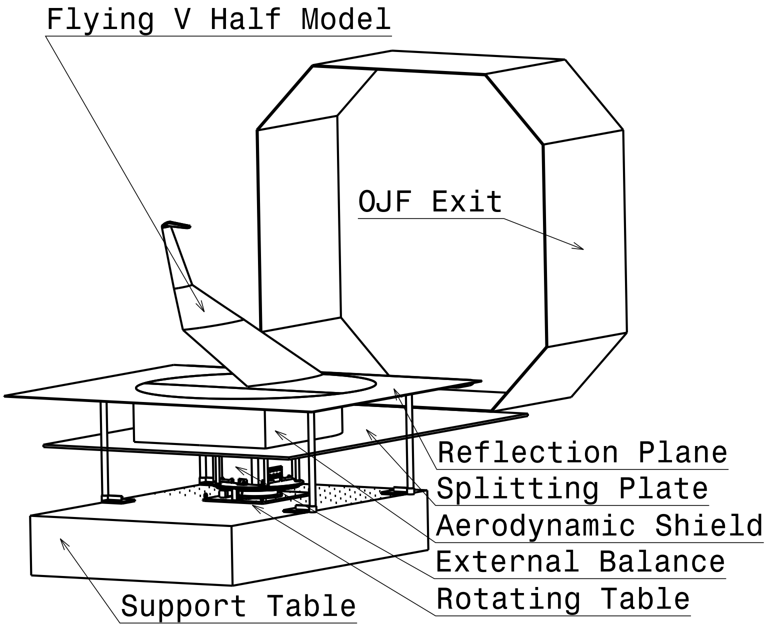

Figure 2.5: Isometric View of Wind Tunnel Setup, Including Nomenclature of Components. Note That The OJF Exit is 2.85 m in Width and Height.

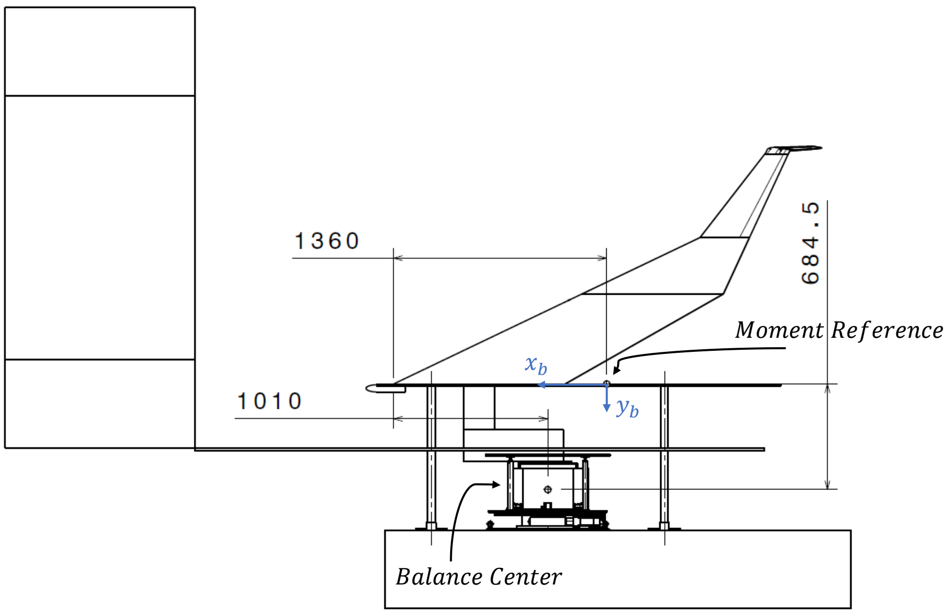

Figure 2.6: Side View of Flying V Wind Tunnel Setup Showing the Balance Center and Reference Positions with Respect to the Model Leading Edge. The Shield is Hidden and the Dimensions are in mm.

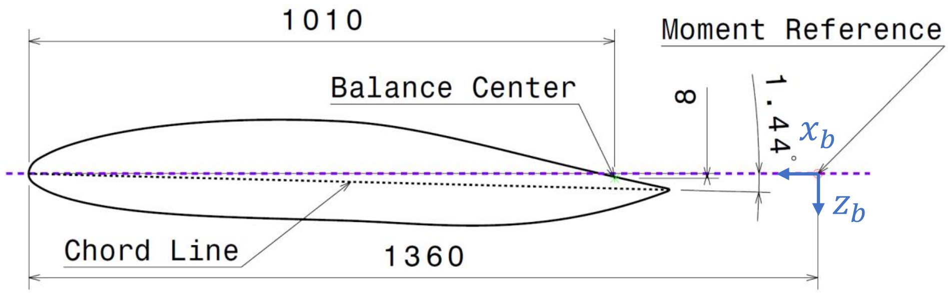

Figure 2.7: Top View of Flying V Wind Tunnel Setup Showing the Root Airfoil, Balance Center, Chord Line, Moment Reference Position and $x_\mathrm{b} - y_\mathrm{b}$-Plane (in Purple). Dimensions are in mm.

2.3. Aerodynamic Force and Moment Calculation

First, the measured forces and moments at the external balance center must be transformed to body forces at another reference position (SFTM MR Position in this case), shown in Figures 2.8 and 2.9. The SFTM MR position 1.36 m aft of the leading edge was chosen by the scaled flight testing team based on previous wind tunnel tests and other considerations. Note that the direction of the x, y and z axes between the two reference frames are shifted and both frames rotate with the same angle of attack. In these figures, the origin for the body frame forces is centered at the SFTM MR position and the origin for the balance forces are centered at the balance center. In conclusion, new body frame forces and moments are drawn at the MR and their values are derived from those measured at the balance center using force and moment equilibrium.

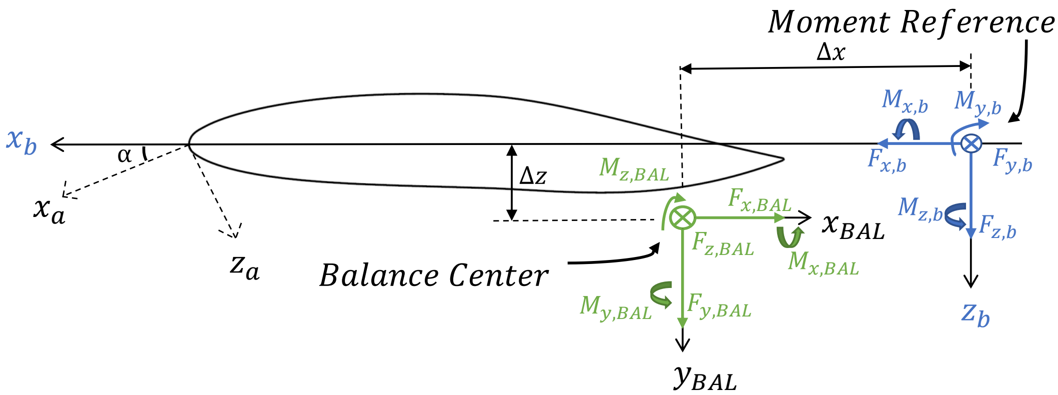

Figure 2.8: Root Airfoil Schematic with the Force and Moment Definitions for the Body and Balance Reference Frames. Note that $F_{y,\mathrm{b}}$ Points Into the Page at the Reference Position and $M_{y,\mathrm{b}}$ Also Acts Here. This is Similar for $F_{z,\mathrm{BAL}}$ and $M_{z,\mathrm{BAL}}$ at the Balance Center.

Using these figures, one can derive the relations in Equations 2.1 through 2.3 between the measured balance forces and those at the new reference location. The moments in the body frame are derived using the same figures in Equations 2.4 though 2.6. Note the moment equations have been derived with respect to the SFTM MR position, so the three distances (Δx, Δy and Δz) are positive. The values of the distances used in the moment Equations 2.4 through 2.6 are given in Table 2.2.

$$F_{x,\mathrm{b}} = -F_{x,\mathrm{BAL}} \quad (2.1) \qquad F_{y,\mathrm{b}} = F_{z,\mathrm{BAL}} \quad (2.2) \qquad F_{z,\mathrm{b}} = F_{y,\mathrm{BAL}} \quad (2.3)$$

$$M_{x,\mathrm{b}} = l = -M_{x,\mathrm{BAL}} - F_{z,\mathrm{BAL}}(\Delta z) + F_{y,\mathrm{BAL}}(\Delta y) \tag{2.4}$$

$$M_{y,\mathrm{b}} = m = M_{z,\mathrm{BAL}} - F_{y,\mathrm{BAL}}(\Delta x) - F_{x,\mathrm{BAL}}(\Delta z) \tag{2.5}$$

$$M_{z,\mathrm{b}} = n = M_{y,\mathrm{BAL}} + F_{z,\mathrm{BAL}}(\Delta x) + F_{x,\mathrm{BAL}}(\Delta y) \tag{2.6}$$

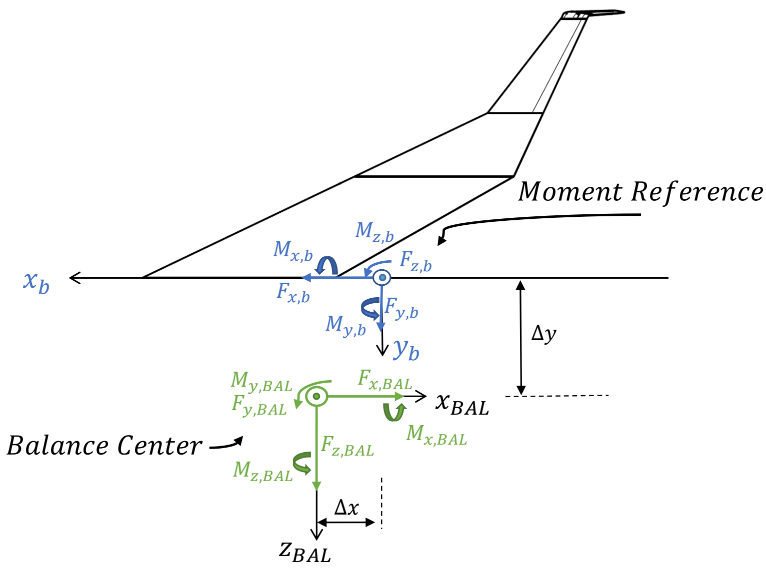

Figure 2.9: Schematic Viewing the WTM from the Pressure Side Again Illustrating the Force and Moment Definitions for the Body and Balance Reference Frames. Note That $F_{z,\mathrm{b}}$ Points Out of the Page at the Reference Position and $M_{z,\mathrm{b}}$ Also Acts Here. This is Similar for $F_{y,\mathrm{BAL}}$ and $M_{y,\mathrm{BAL}}$ at the Balance Center.

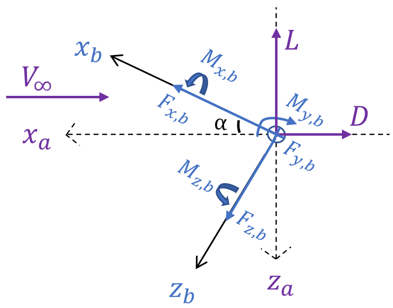

Figure 2.10: Schematic Showing the Transformation of Forces from the Body Reference Frame to the Aerodynamic Reference Frame. Note that $F_{y,\mathrm{b}}$ Points Into the Page at the Vertex of the x_a and z_a Axes. $M_{y,\mathrm{b}}$ Also Acts Here.

It turns out that the body frame moments (about the x_b, y_b and z_b directions) are equal to the rolling, pitching and yawing aerodynamic moments, respectively. The aerodynamic lift, drag and side forces are derived in Equations 2.7 through 2.9 using the diagram in Figure 2.10. Note that these loads are those due to one single wing. Next, these aerodynamic forces and moments are transformed into non-dimensional aerodynamic coefficients to be used in the results. Before this can happen, the manner at which the half-model (single wing) loads are converted to represent the (two-wing) SFTM must be defined. This is explained in the next section.

$$L = F_{x,\mathrm{b}}\, sin(\alpha) - F_{z,\mathrm{b}}\, cos(\alpha) = -F_{x,\mathrm{BAL}}\, sin(\alpha) - F_{y,\mathrm{BAL}}\, cos(\alpha) \tag{2.7}$$

$$D = -F_{x,\mathrm{b}}\, cos(\alpha) - F_{z,\mathrm{b}}\, sin(\alpha) = F_{x,\mathrm{BAL}}\, cos(\alpha) - F_{y,\mathrm{BAL}}\, sin(\alpha) \tag{2.8}$$

$$Y = F_{y,\mathrm{b}} = F_{z,\mathrm{BAL}} \tag{2.9}$$

Table 2.2: Distances Used in Moment Expressions for the SFTM MR Position.

Reference Position	Δx [m]	Δy [m]	Δz [m]
SFTM Moment Reference	0.35	0.6845	0.008

2.3.1. Half-Model to Full-Model Loads

When using the half-model loads to describe the full model's behavior, the half-model loads cannot simply be doubled to arrive at the full model loads for all of the tested conditions. This is the case when the aircraft has asymmetric control inputs or sideslip conditions. For example, when considering an SFTM flight condition with the rudder and/or aileron deflected, the aerodynamic forces on the left wing are *not* the same as those on the right wing. If the ailerons are positively deflected, the left wing's aileron is deflected trailing edge up and the right wing aileron is deflected trailing edge down. This will clearly have an effect on the aerodynamic forces and moments produced by the left and right wings, causing them to be different. The same principle applies for rudder deflections. Conversely, the forces on the left and right wings with Flying V subject to a pure elevator deflection are assumed to be the same, due to the symmetry of the elevator deflections on the left and right wings.

To address this, the aerodynamic forces for a particular SFTM flight condition are calculated for the left wing and right wing separately, then they are added together to form the ‘dual-wing’, complete Flying V aerodynamic coefficients from the half-model tests. Here, it is first assumed that the left wing half-model can accurately represent both the left and right wing separately, due to symmetry. Furthermore, it is assumed that the changes to the flow conditions around one wing due to control surface deflections do not affect the aerodynamics of the other. For example, if the right wing’s rudder is deflected, there is assumed to be no change in the flow field around the left wing. This is a characteristic of the half-model approach as only one half of the wing is tested in the tunnel at a time.

In the next paragraphs, the calculation of the aerodynamic coefficients are explained while considering the dual-wing model with positive rudder, aileron and elevator deflections. Note that this is a generalized method which also applies for negative control surface deflections. As mentioned in Section 2.1.3, the rudders on both wings move to the left under a positive aircraft rudder deflection. The rudder on the left wing will move away from the root and the rudder on the right wing will move towards it. Since only the left wing is used in the tunnel, the right wing conditions are found by using the left wing model with the corresponding rudder deflection of opposite sign. A positive aircraft aileron deflection will deflect the third control surface (CS3) of the left wing to a negative, trailing edge upward, angle. The same positive aircraft aileron deflection corresponds to a positive, trailing edge down deflection of the third control surface on the right wing. Similar to the rudder, the right wing conditions are found by using the left wing model with the corresponding normalized CS3 deflection of opposite sign. Finally, a positive aircraft elevator deflection corresponds to positive CS1 and CS2 deflections (these move together as an elevator) on the left and right wings.

This is expressed mathematically in Equation 2.10 and 2.11 for the lift of each wing. In these expressions, the subscript ’WTM’ refers to the wind tunnel model results, ’LW’ indicates the left wing results and ’RW’ the right wing. Similarly, the expressions for the drag and pitching moment of the left and right wing using the wind tunnel model are shown in Equations 2.12 through 2.15. The aircraft (dual-wing) lift, drag and pitching moment coefficients are approximated by summing the coefficients due to the left and right wings in Equations 2.16, 2.17 and 2.18, respectively. In the calculation of these coefficients, the value of the dynamic pressure measured by the wind tunnel sensors for that specific test is used to account for both the changing atmospheric conditions (ρ) and airspeed (V_∞).

$$L_{\mathrm{LW}} = L_{\mathrm{WTM}}\left(+\overline{\delta}_{\mathrm{R}}, -\overline{\delta}_{\mathrm{A}}, +\overline{\delta}_{\mathrm{E}}, V_\infty\right) \quad (2.10) \qquad L_{\mathrm{RW}} = L_{\mathrm{WTM}}\left(-\overline{\delta}_{\mathrm{R}}, +\overline{\delta}_{\mathrm{A}}, +\overline{\delta}_{\mathrm{E}}, V_\infty\right) \quad (2.11)$$

$$D_{\mathrm{LW}} = D_{\mathrm{WTM}}\left(+\overline{\delta}_{\mathrm{R}}, -\overline{\delta}_{\mathrm{A}}, +\overline{\delta}_{\mathrm{E}}, V_\infty\right) \quad (2.12) \qquad D_{\mathrm{RW}} = D_{\mathrm{WTM}}\left(-\overline{\delta}_{\mathrm{R}}, +\overline{\delta}_{\mathrm{A}}, +\overline{\delta}_{\mathrm{E}}, V_\infty\right) \quad (2.13)$$

$$m_{\mathrm{LW}} = m_{\mathrm{WTM}}\left(+\overline{\delta}_{\mathrm{R}}, -\overline{\delta}_{\mathrm{A}}, +\overline{\delta}_{\mathrm{E}}, V_\infty\right) \quad (2.14) \qquad m_{\mathrm{RW}} = m_{\mathrm{WTM}}\left(-\overline{\delta}_{\mathrm{R}}, +\overline{\delta}_{\mathrm{A}}, +\overline{\delta}_{\mathrm{E}}, V_\infty\right) \quad (2.15)$$

$$C_L = \frac{L_{\mathrm{LW}}}{qS} + \frac{L_{\mathrm{RW}}}{qS} \quad (2.16) \qquad C_D = \frac{D_{\mathrm{LW}}}{qS} + \frac{D_{\mathrm{RW}}}{qS} \quad (2.17) \qquad C_m = \frac{m_{\mathrm{LW}}}{qS\overline{c}} + \frac{m_{\mathrm{RW}}}{qS\overline{c}} \quad (2.18)$$

The SFTM should exhibit zero side force, rolling moment and yawing moment for all angles of attack, unless there is a rudder deflection, aileron deflection or sideslip (asymmetry). Thus, the side force, yawing and rolling moments are defined in terms of their change, or deltas, from the symmetric case due to an aileron or rudder deflection for each wing. Then, the deltas due to the aileron or rudder deflection of the left and right wings are added together to form the remaining aerodynamic coefficients.

The expressions for the side-force acting on the left and right wings are shown in Equations 2.19 and 2.20, respectively. Like the previous coefficients, the side-force coefficients for the left and right wings are added together to estimate the dual-wing side-force coefficient in Equation 2.21. Note that the right wing results have negative sign in this equation; this is because the WTM is a left wing and the change in side-force with a rudder/aileron deflection for the right wing is of equal and opposite sign. The same process used for the side-force coefficient is used for the rolling and yawing moment coefficients with Equations 2.22 and 2.23. Note that the second term on the right hand side of Equations 2.19, 2.20 and the similar ones for the rolling and yawing moment (not given) may be omitted if applying Equations 2.21, 2.22 or 2.23 as they cancel each other out.

$$\Delta Y_{\mathrm{LW}} = Y_{\mathrm{WTM}}\left(+\overline{\delta}_{\mathrm{R}}, -\overline{\delta}_{\mathrm{A}}, +\overline{\delta}_{\mathrm{E}}, V_\infty\right) - Y_{\mathrm{WTM}}\left(\overline{\delta}_{\mathrm{R}} = 0, \overline{\delta}_{\mathrm{A}} = 0, \overline{\delta}_{\mathrm{E}} = 0, V_\infty\right) \tag{2.19}$$

$$\Delta Y_{\mathrm{RW}} = Y_{\mathrm{WTM}}\left(-\overline{\delta}_{\mathrm{R}}, +\overline{\delta}_{\mathrm{A}}, +\overline{\delta}_{\mathrm{E}}, V_\infty\right) - Y_{\mathrm{WTM}}\left(\overline{\delta}_{\mathrm{R}} = 0, \overline{\delta}_{\mathrm{A}} = 0, \overline{\delta}_{\mathrm{E}} = 0, V_\infty\right) \tag{2.20}$$

$$C_Y = \frac{\Delta Y_{\mathrm{LW}}}{qS} - \frac{\Delta Y_{\mathrm{RW}}}{qS} \tag{2.21}$$

$$C_l = \frac{\Delta l_{\mathrm{LW}}}{qSb} - \frac{\Delta l_{\mathrm{RW}}}{qSb} \tag{2.22}$$

$$C_n = \frac{\Delta n_{\mathrm{LW}}}{qSb} - \frac{\Delta n_{\mathrm{RW}}}{qSb} \tag{2.23}$$

The half-wing values for side-force, rolling moment and yawing moment will occasionally be used to illustrate what is occurring on the half-model and it will be clearly indicated when this is the case. The half-wing side-force coefficient is the nondimensionalized first term on the right hand side of Equation 2.19 and this is similar for the rolling and yawing moments. Note that the normalized control surface deflections are used in these equations such that $+\overline{\delta}_{\mathrm{R}} = 25$ % and $-\overline{\delta}_{\mathrm{R}} = -25$ %, for example. As shown in Section 3.5, a given deflection (in degrees) is not of equal magnitude with opposite sign for corresponding positive and negative normalized deflections. For the main wing control surfaces, negative normalized deflections cause larger deflection angles than the corresponding positive ones. For the rudder, negative normalized deflections cause smaller angular deflections than the corresponding positive ones as shown in Section 3.5. Differential aileron deflection is used in the aircraft industry to reduce adverse yaw phenomena due to aileron deflections.

2.4. Configuration Nomenclature

The simplest configuration that was tested is when the model had no winglet (or rudder) installed and had zero control surface deflection. This can be referred to the clean wing with no rudder and is symbolized by 'NWL' (for no winglet) in Table 2.3. Once the winglet was installed, the rudder and main wing control surfaces were deflected in various runs with different combinations. The run with the wing control surfaces at null deflection while the rudder is swept along each deflection at 20 m/s is the run labelled 'WL 1' in Table 2.3. This can be referred to as a clean rudder sweep. Furthermore, clean rudder sweeps at 18 m/s, 25 m/s and 28 m/s are labelled as 'WL V18', 'WL V25' and 'WL V28', respectively, in Table 2.3. Next, the three wing control surfaces identified in Figure 2.1 are deflected in the remaining runs 'WL 2N' though 'WL 9D'. *During the experiments, all three main wing control surfaces were either all deflected to the same percent deflection and direction (sublabel 'D'), OR the two inboard surfaces are at 0 deflection while only the outboard control surface is deflected (sublabel 'N').* This was done to both obtain the full control power and to isolate possible effects of the outboard control surface on the rudder effectiveness. Additional combinations of control surface deflections were not tested in this research project. The analysis of the full control power has been covered in Ref. [11] and is out of the scope of this text. The motivation for the test matrix in Table 2.3 is explained in the next section.

2.5. Testing Strategy and Matrices

The testing matrix in Table 2.3 has been formulated to answer the research questions in Section 1.4. The research questions will be answered for the airspeed of 20 m·s^{-1} as this is near the take-off and landing speed for the SFTM. The first research question may be answered by conducting wind tunnel experiments with the same flow conditions using the WTM without the winglet, then integrating the winglet and repeating the experiments. In terms of the defined configuration nomenclature, this would be comparing the results of NWL to those of 'WL 1' (with the rudder at 0 deflection). The procedure for the 'NWL' run is to take a measurement at each angle of attack in the stated range at 20 m/s.

The second research question may be answered by conducting wind tunnel experiments with the same flow conditions for various rudder deflections using the WTM with the winglet installed. With regards to the defined nomenclature, this is a comparison of the results from within the 'WL 1' run. This is because 'WL 1' contains results with $\overline{\delta}_{\mathrm{CS1}}$ = $\overline{\delta}_{\mathrm{CS2}}$ = $\overline{\delta}_{\mathrm{CS3}}$ = 0 for all rudder deflections and angles of attack. The procedure for the 'WL 1' run is to take a measurement at each rudder deflection for every angle of attack in the stated ranges for these variables. Next, the main wing control surfaces were set to a different position and this procedure was repeated in runs 'WL 2' through 'WL 9'.

The third research question may be answered by comparing the rudder effectiveness from runs with the outboard control surfaces at null deflection ('WL 1') to that from runs with the outboard control surfaces at various other deflections ('WL 2' - 'WL 9'). These results will be contrasted to quantify the influence of the outboard control surface deflection on the rudder effectiveness.

Since the previous Flying V researchers in Refs. [11–14] found an unstable pitch break at an angle of attack of $20°$, it has been decided to keep the SFTM below this angle during flight for risk reduction. Thus, the most important angle of attack range is from $-5°$ to $20°$. With this in mind, the tested angles of attack (for 20 m/s) are from $-5°$ to $30°$ to record data for the flight α range and further angles to identify possible effects of winglet integration on the pitch break. However, as the tunnel airspeed and angle of attack are increased, the loads acting on the external balance also increase and will reach the load limit of the balance. This is why there are lower angle of attack limits for the speeds above 20 m/s in the test matrix. Also, at higher angles of attack the wing tip of the WTM exhibited oscillatory heaving motions, possibly due to the lack of bending rigidity and non-linear vortex shedding. This is another factor limiting the airspeed and angle of attack ranges tested.

Table 2.3: Test Matrix Describing WTT Runs. Note That the Format of the Data in the α and $\overline{\delta}_{\mathrm{R}}$ Columns are $min : max : step$. The Last Column Indicates How Many Repetitions Have Been Performed with Open and/or Closed Gaps as Will Be Discussed in Section 3.1.

Run Name	α [°]	V_∞ [m/s]	$\overline{\delta}_{\mathrm{CS12}}$ [%]	$\overline{\delta}_{\mathrm{CS3}}$ [%]	$\overline{\delta}_{\mathrm{R}}$ [%]	$N_{\mathrm{o}}/N_{\mathrm{c}}$
NWL	$-5:35:5$	20	0	0	N/A	$3/0$
WL 1	$-5:30:5$	20	0	0	$-100:100:25$	$3/3$
WL 2N	$-5:30:5$	20	0	25	$-100:100:25$	$3/0$
WL 2D	$-5:30:5$	20	25	25	$-100:100:25$	$3/0$
WL 3N	$-5:30:5$	20	0	-25	$-100:100:25$	$3/0$
WL 3D	$-5:30:5$	20	-25	-25	$-100:100:25$	$3/0$
WL 4N	$-5:30:5$	20	0	50	$-100:100:25$	$3/2$
WL 4D	$-5:30:5$	20	50	50	$-100:100:25$	$3/2$
WL 5N	$-5:30:5$	20	0	-50	$-100:100:25$	$3/2$
WL 5D	$-5:30:5$	20	-50	-50	$-100:100:25$	$3/2$
WL 6N	$-5:30:5$	20	0	75	$-100:100:25$	$1/1$
WL 6D	$-5:30:5$	20	75	75	$-100:100:25$	$1/1$
WL 7N	$-5:30:5$	20	0	-75	$-100:100:25$	$0/2$
WL 7D	$-5:30:5$	20	-75	-75	$-100:100:25$	$0/2$
WL 8N	$-5:30:5$	20	0	100	$-100:100:25$	$0/2$
WL 8D	$-5:30:5$	20	100	100	$-100:100:25$	$0/2$
WL 9N	$-5:30:5$	20	0	-100	$-100:100:25$	$0/2$
WL 9D	$-5:30:5$	20	-100	-100	$-100:100:25$	$0/2$
WL V18	$-5:35:5$	18	0	0	$-100:100:25$	$0/2$
WL V25	$-5:20:5$	25	0	0	$-100:100:25$	$0/2$
WL V28	$-5:15:5$	28	0	0	$-100:100:25$	$0/1$

2.6. Bias Correction

The external load balance sends continuous signals representing the test variables to a computer running LabVIEW. At the user's request (mouse click) LabVIEW samples from these signals over a period of 10 s and logs the means of the continuous values to a local '.txt' file. The time at which the measurement is taken is recorded along with the average forces, moments, airspeed, dynamic pressure, static pressure and temperature over the sampling interval.

Since the external balance was found to build a bias over time, it was decided to correct this from the data. This bias is found by obtaining a measurement from the balance both before and after the measurement run while the tunnel is off and the wing is in the same position in 3D space (turning table position). The bias is assumed to build linearly with time and is corrected from the data using Equation 2.24. Here, the 'i', 'f' and '$meas$' subscripts indicate the initial time, final time and the time of the measurement being corrected, respectively. This equation was derived using the sketch in Figure 2.11a. The assumed linear bias increase (or decrease) with time is subtracted from the measured force at the corresponding measurement time. Furthermore, the initial bias value is subtracted from each measurement and this corrects the initial bias value to zero (imagine $\Delta t_{meas} = 0$ s). This also works for negative changes in bias with time and negative initial bias measurements.

$$F_{corr} = F_{meas} - \frac{F_f - F_i}{t_f - t_i}\Delta t_{meas} - F_i \tag{2.24}$$

An example plot of the bias measurements for each of the 6 recorded forces and moments recorded by the balance are shown in Figure 2.11b. In this example, $F_{x,\mathrm{BAL}}$ initially was around 0.09 N before the run began and 0.31 N afterward. When considering all 6 measured balance forces and moments, the maximum and minimum bias correction was $\Delta F_{x,\mathrm{BAL}} = 0.275$ N and $\Delta F_{z,\mathrm{BAL}} = -0.462$ N, respectively, over all runs. All of the other bias corrections of the forces and moments used in the results are smaller in magnitude. In Table 2.4, the error between measured and known applied loads found during the balance calibration in Ref. [5] are presented. The maximum error and standard deviation of the error are presented as a percentage of the nominal loads for each of the 6 force/moment components.

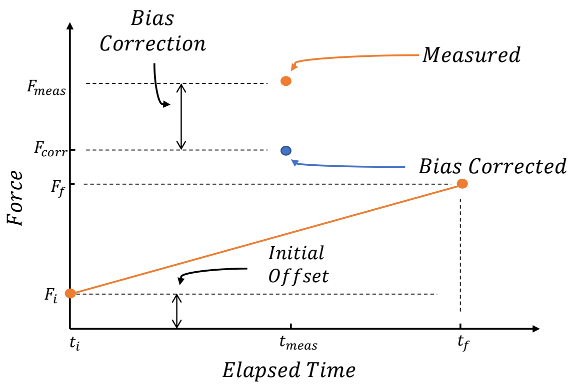

(a) Schematic Used to Derive the Bias Correction.

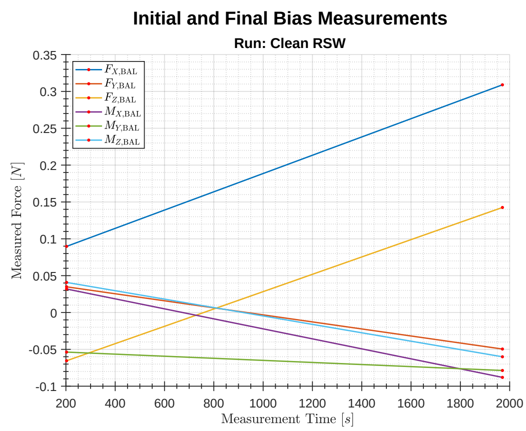

(b) External Balance Measurement Bias Buildup Over Time. Note That the Moment Units are Nm.

Figure 2.11: OJF External Balance Bias Analysis.

Table 2.4: Maximum and Standard Deviation of the External Balance Errors Found in Ref. [5] During Calibration. Both Are Presented as a Percent of the Nominal Load.

Item	$F_{x,\mathrm{BAL}}$	$F_{y,\mathrm{BAL}}$	$F_{z,\mathrm{BAL}}$	$M_{x,\mathrm{BAL}}$	$M_{y,\mathrm{BAL}}$	$M_{z,\mathrm{BAL}}$
e_{MAX} %	0.06	0.23	0.16	0.05	0.05	0.25
σ_e %	0.02	0.05	0.05	0.01	0.01	0.07

3

Verification and Validation

This chapter first describes the process used to correct some of the experimental results from this project for holes found in the reflection plate in Section 3.1. Next, the maximum standard deviations for all experimental runs are given in Section 3.2. The method to calculate the confidence intervals is explained in Section 3.3 and the results of this research project are compared and contrasted to that of previous Flying V wind tunnel studies in Section 3.4. Finally, the measured control surface angles for an input normalized deflection (in %) are presented in Section 3.5.

3.1. Gap Correction

During the wind tunnel campaign undertaken to generate the data for this thesis, two holes discovered in the reflection plane of the wind tunnel setup were closed. The areas of the reflection plate which were closed are shown in Figure 3.1 by the white boxes. Furthermore, photos showing the gap (covering) on the wind tunnel setup are shown in Figures B.1 and B.2 in Appendix B.1. The hole in the front was closed with tape while the one towards the back was closed with an aluminum plate taped onto the bottom of the reflection plane within the shielded volume.

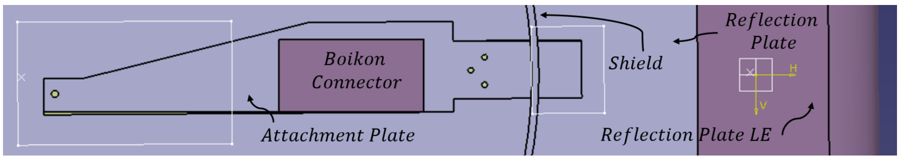

Figure 3.1: Areas of Reflection Plate Which Were Covered During the Wind Tunnel Test Campaign. Here, One is viewing the Reflection Plate From the Bottom and One Can See the Wing Attachment Plate Above it. Here, the Flow is From Right to Left.

A number of configurations were repeated with the two holes open and closed to form a database of the effect of wing configuration on the effect closing these holes on the aerodynamic coefficients. In this report, the effect of closing the two gaps on the aerodynamic coefficients will be referred to as the 'gap effect'. Rudder sweep experiments (sweeping rudder over all nine deflections at each AoA) using configurations with the wing trailing edge control surfaces at 0%, $+50\%$, -50% and $+75\%$ deflection were repeated three times with the holes open and closed. Note that the runs with $+50\%$, -50% and $+75\%$ wing trailing edge deflections include data with $\overline{\delta}_{\text{CS1}}$ = $\overline{\delta}_{\text{CS2}}$ = $\overline{\delta}_{\text{CS3}}$ *and* $\overline{\delta}_{\text{CS1}}$ = $\overline{\delta}_{\text{CS2}}$ = 0% while CS3 is deflected. There are 117 data points included to calculate the gap effect for each aerodynamic coefficient at each angle of attack. The gap effect is found by subtracting the aerodynamic coefficient with the holes open from that with the holes closed. As an example, the gap effect to be added to the open lift results is shown in Equation 3.1. The results with the holes open are corrected and artificially closed by adding the gap effect to the open results in Equation 3.2. The gap effects are calculated and applied to half wing results. Furthermore, all of the gap effects for the various configurations have been grouped together to form one constant set of gap effects to be applied to the open results for each aerodynamic coefficient at each AoA. All gap effects, their means and sample standard deviations are shown in Figures A.1a though A.3b in Appendix A.1. The gap effects change with angle of attack due to the position of these holes with respect to the wind tunnel (shield) varying.

$$\Delta_{Gap\ C_L} = C_{L_\mathrm{c}} - C_{L_\mathrm{o}} \tag{3.1}$$

$$C_{L_\mathrm{corr}} = C_{L_\mathrm{o}} + \Delta_{Gap\ C_L} \tag{3.2}$$

The covering of the holes did affect the balance measurements as shown in the plots of the aerodynamic coefficients before (labelled 'open') and after the holes were closed (labelled 'closed') in Appendix A.2. Appendix A.2 also plots the corrected results as if there were not 'closed' results for the cases. Figures A.4a though A.12b in Appendix A.2 show that the corrected results are very close to the actual closed results for three different trailing edge control surface deflections. These are the $\overline{\delta}_\mathrm{CS1}$ = $\overline{\delta}_\mathrm{CS2}$ = $\overline{\delta}_\mathrm{CS3}$ = 0%, $\overline{\delta}_\mathrm{CS1}$ = $\overline{\delta}_\mathrm{CS2}$ = $\overline{\delta}_\mathrm{CS3}$ = 50% and $\overline{\delta}_\mathrm{CS1}$ = $\overline{\delta}_\mathrm{CS2}$ = $\overline{\delta}_\mathrm{CS3}$ = -50% configurations. The correction of the pitching moment curves exhibit the largest error, or the difference between 'closed' and 'corrected' results. Note that the actual, or 'closed' means all lie within the 95% confidence intervals of the corrected means. Also note that the 'closed' results have a larger confidence interval than the 'corrected' results in some cases due to the lower sample size ($N = 2$) for the closed runs. This is only the case for the $\overline{\delta}_\mathrm{CS1}$ = $\overline{\delta}_\mathrm{CS2}$ = $\overline{\delta}_\mathrm{CS3}$ = $+50\%$ and $\overline{\delta}_\mathrm{CS1}$ = $\overline{\delta}_\mathrm{CS2}$ = $\overline{\delta}_\mathrm{CS3}$ = -50% configurations.

The hole near the leading edge of the reflection plate allowed relatively high pressure air in front of the shield to impinge on the wing attachment plate by flowing through the reflection plate from below, causing a negative side-force. This can be seen in the side-force coefficient plots in Figures A.5a, A.8a and A.11a. After the hole in the reflection plate was closed, the side-force coefficient increased and this is similar for the gap effect on the yawing moment. Finally, part of the hole aft of the boikon connector was also closed. While open, this hole allowed air to travel from above the reflection plate into a closed cavity in which the boikon connector is placed.

The sample standard deviation of the corrected results can be found with the variance sum law in Equation 3.3. Here, $s_{\overline{X}\pm\overline{Y}}$ is the sample standard deviation of the sum or difference of two random variables, $\overline{X}$ and $\overline{Y}$. The sample standard deviations of the $\overline{X}$ and $\overline{Y}$ variables are $s_{\overline{X}}$ and $s_{\overline{Y}}$, respectively. Finally, the correlation coefficient between the two sets is given by $\hat{\rho}_{\overline{XY}}$. The correlation is 0 because the gap effect is assumed to be independent of the coefficient value. For the application of the gap effect, $\overline{X}$ represents the open half-wing results (to be corrected) and $\overline{Y}$ represents the half-wing gap effects. The resulting standard deviation would be that due to one wing. To find the total sample standard of the dual-wing results, Equation 3.3 is applied again. This time, $\overline{X}$ and $\overline{Y}$ correspond to the left and right wing results, respectively. Here, the results of the left and right wings are also assumed to be independent, causing $\hat{\rho}_{\overline{XY}} = 0$. All runs that have results with the gaps open have been corrected. The runs with the gaps open can be identified in Tables 2.3 or 3.1 when $N_\mathrm{o} \neq 0$. It will be indicated in the results as to which (corrected or uncorrected) results are presented.

$$s^2_{\overline{X}\pm\overline{Y}} = s^2_{\overline{X}} + s^2_{\overline{Y}} \pm 2\hat{\rho}_{\overline{XY}} s_{\overline{X}} s_{\overline{Y}} \tag{3.3}$$

3.2. Maximum Deviations of All Results

In this section, the sample standard deviations of the Flying V wind tunnel runs used in the results are reported in Table 3.1. All sample standard deviations are reported for a half-wing Flying V. To obtain the full-wing sample standard deviation, on must use Equation 3.3 with $s_{\overline{X}}$ representing the sample standard deviation of the left wing results and $s_{\overline{Y}}$ is that for the right wing. This allows the dual-wing sample standard deviation to be calculated using left and right wing in non-symmetric flight conditions (aileron, rudder deflected). The results used for the left wing are assumed to be independent of those from the right wing, causing $\hat{\rho}_{XY}$ in Equation 3.3 to again be zero. Note that the deviation due to the shift application is already included in the half-wing sample standard deviations, as explained in Section 3.1. The N/A table entries are present because those configurations were not tested with the open or closed holes/gaps described in Section 3.1. All (maximum) standard deviations in Table 3.1 are regarding the lift coefficient, unless indicated otherwise.

Table 3.1: Maximum Sample Standard Deviations of Half-Wing Tests. The ‘o’, ‘corr’ and ‘c’ Subscripts Indicate a Run Using Open, Corrected or Closed Results, Respectively. The Last Column Indicates How Many Repetitions Have Been Performed With the Open and/or Closed Gaps. The α Columns indicate the Corresponding AoA for the Maximum s. All Standard Deviations Are Regarding the Lift Coefficient, Unless Indicated.

Run Name	$s_{\mathrm{MAX,o}}$ [-]	α_{o} [°]	$s_{\mathrm{MAX,corr}}$ [-]	α_{corr} [°]	$s_{\mathrm{MAX,c}}$ [-]	α_{c} [°]	$N_{\mathrm{o}}/N_{\mathrm{c}}$ [-]
NWL	0.0014	30	0.0019	30	N/A	N/A	3/0
WL 1	0.0014	30	0.002	30	0.0017	20	3/3
WL 2N	0.0022	20	0.0026	20	N/A	N/A	3/0
WL 2D	0.0026	20	0.0029	20	N/A	N/A	3/0
WL 3N	0.0021	20	0.0024	20	N/A	N/A	3/0
WL 3D	0.002	20	0.0024	20	N/A	N/A	3/0
WL 4N	0.0017	20	0.0021	20	$s_{C_m} = 0.0018$	30	3/2
WL 4D	0.0019	20	0.0023	20	0.0025	25	3/2
WL 5N	0.0019	15	0.0024	15	0.0017	30	3/2
WL 5D	0.0022	0	0.0025	0	0.0015	15	3/2
WL 6N	N/A	N/A	N/A	N/A	N/A	N/A	1/1
WL 6D	N/A	N/A	N/A	N/A	N/A	N/A	1/1
WL 7N	N/A	N/A	N/A	N/A	0.0022	20	0/2
WL 7D	N/A	N/A	N/A	N/A	0.0024	20	0/2
WL 8N	N/A	N/A	N/A	N/A	0.0029	20	0/2
WL 8D	N/A	N/A	N/A	N/A	0.0017	20	0/2
WL 9N	N/A	N/A	N/A	N/A	0.0017	25	0/2
WL 9D	N/A	N/A	N/A	N/A	0.0014	30	0/2
WL V18	N/A	N/A	N/A	N/A	$s_{C_Y} = 0.0029$	35	0/2
WL V25	N/A	N/A	N/A	N/A	0.0025	20	0/2
WL V28	N/A	N/A	N/A	N/A	N/A	N/A	0/1

3.3. Confidence Intervals

Since the sample sizes of the repeated experiments were small and the population mean and variance are both unknown, the t-distribution must be used to construct the confidence intervals for the population mean [29]. Assuming the results gathered form a random sample from a $N(\mu, \sigma^2)$ distribution, the studentized mean in Equation 3.4 has a $t(k)$ distribution, depending on the degrees of freedom $(k = N - 1)$ and not the population mean (μ) or population standard deviation (σ) [29]. Here, the sample standard deviation (s_N) is being used as an estimator for the population standard deviation [29]. Like the normal distribution, the $t(k)$ distribution is also bell shaped, symmetric and centered at zero [29]. As the degrees of freedom or number of tests (N) go to infinity, the $t(k)$ distribution approaches the normal distribution [29]. For lower k, the $t(k)$ distribution has fatter tails with respect to the normal distribution to compensate for the estimation of the population standard deviation from the sample [29]. As the degrees of freedom are reduced, the critical $t_{k,p}$ value for a given level of significance increases, widening the confidence interval.

The critical $t_{k,p}$ value is the number satisfying the condition in Equation 3.5 [29]. This says that the probability to obtain a value of T greater than or equal to the critical value $(t_{k,p})$ is equal to the right tail probability $p = (1 - \gamma)/2$. The critical $t_{k,p}$ value is a number read from a t-distribution table for a given number of degrees of freedom and right tail probability p. In this report, the confidence level (γ) used is 95%. The significance level $(\hat{\alpha})$ is split into two-tails to account for both underestimation and overestimation of the true mean. Equation 3.6 states that the studentized mean will lie between the critical $t_{k,p}$ values with probability $\gamma = 1 - \hat{\alpha}$ [29]. Therefore, a $100(1-\hat{\alpha})\%$ confidence interval for the population mean (μ) is given by Equation 3.7 [29]. This equation is used in the results to construct the confidence intervals in this report.

If considering the open, uncorrected results, s_N used in the Equation for the confidence interval is the sample standard deviation of the open, uncorrected results. If considering the (gap) corrected results, the s_N used in the confidence interval calculation is the standard deviation of the corrected results explained in Section 3.1. The usage of the half-wing or full-wing sample standard deviation (explained in Section 3.1) corresponds to whether the half-wing or full-wing sample means are plotted.

$$T = \frac{\bar{x}_n - \mu}{s_N/\sqrt{N}} \tag{3.4}$$

$$P(T \geq t_{k,p}) = p = \hat{\alpha}/2 \tag{3.5}$$

$$P(-t_{k,\hat{\alpha}/2} < \frac{\bar{x}_N - \mu}{s_N/\sqrt{N}} < t_{k,\hat{\alpha}/2}) = 1 - \hat{\alpha} \tag{3.6}$$

$$(\bar{x}_N - t_{k,\hat{\alpha}/2}\frac{s_N}{\sqrt{N}}\ ,\ \bar{x}_N + t_{k,\hat{\alpha}/2}\frac{s_N}{\sqrt{N}}) \tag{3.7}$$

3.4. Comparison To Previous Research

In this section, the results of this wind tunnel campaign will be compared to those of the previous researchers. The comparison includes the results from Palermo [11], Ruiz Garcia [13] and Van Empelen [14]. The results from these projects using the consistent MR position 1.36 m aft of the nose have been assembled in Figure 4.2 of the report by Van Empelen in Ref. [14]. Note that a zig-zag strip *was* installed on the wind tunnel model in those campaigns while it *was not* installed on the results of this campaign. To address this difference, two more sets of results are included in this chapter. These are results from Van Uitert in Ref. [30] and are obtained using the model both with and without the zig-zag strip. The research of Van Uitert [30] will investigate the effects of the zig-zag strip in more detail and is yet to be published.

The lift coefficients obtained from this campaign and those of the previously mentioned researchers are shown in Figure 3.2a. One can see that all of the results of the four wind tunnel campaigns *with* the zig-zag strip installed see the same trend in the lift coefficient with angle of attack. Around $10°$, all of the results with the zig-zag strip see a non-linearity increasing C_{L_α}. This is thought to be due to vortex lift. After the zig-zag strip was removed, this vortex lift increment seems to have disappeared, with the lift coefficient increasing linearly with AoA. This is shown with the 'Van Uitert (ZZ Off)', 'NWL' and 'WL' curves in Figure 3.2a. Thus, the lift coefficient results of the Flying V without the winglet from this research project ('NWL') match very well with those of Van Uitert without the zig-zag strip installed ('Van Uitert (ZZ Off)'), suggesting good repeatability. Without the zig-zag strip, the lift curve slope only begins to decrease around $30°$ AoA. Among other phenomena, the effect of the zig-zag strip will be investigated in more depth within the research of Van Uitert in Ref. [30], which is yet to be published.

The pitching moment coefficients obtained from this campaign and those of the previously mentioned researchers are shown in Figure 3.2b. One can see that all of the results of the four wind tunnel campaigns *with* the zig-zag strip installed see a similar trend with angle of attack. With the zig-zag, the pitching moment curves are relatively flat from $-5°$ to $5°$ AoA. There seems to be some variance between the ZZ On results of Ruiz Garcia, Palermo, Van Empelen and Van Uitert (ZZ On) between $5°$ and $20°$. However, around $20°$ all results with the zig-zag on become pitch unstable. After the zig-zag strip was removed, the pitching moment curve follows a different trend.

After the zig-zag was removed, the pitching moment curve slopes down in the range of AoA from $-5°$ to $10°$ for for the three cases. When the winglet was not installed (cases 'Van Uitert (ZZ Off)' and 'NWL'), the pitching moment curve slope remains negative until around $20°$. Here, the pitching moment curve slope does not become positive/unstable until $20°$. Between $25°$ and $30°$, there is another change in sign of the slope of the pitching moment curve, ultimately becoming unstable for angles beyond $30°$.

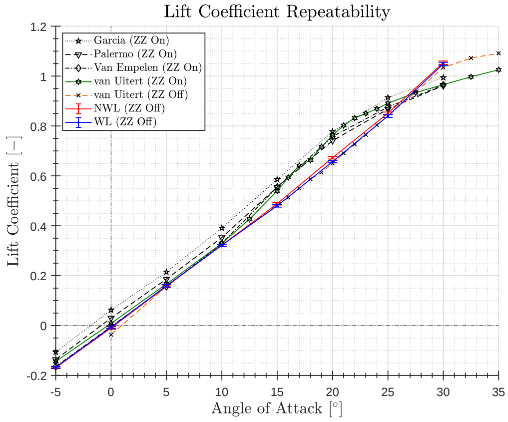

(a) Lift Coefficient Repeatability. The WL and NWL Results Include 95% Confidence Intervals. [14]

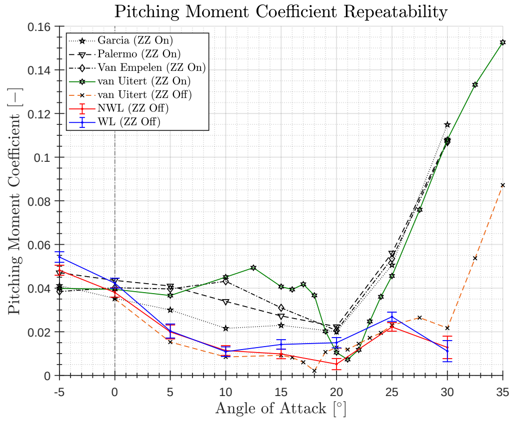

(b) Pitching Moment Coefficient Repeatability. The WL and NWL Results Include 95% Confidence Intervals. [14]

Figure 3.2: Lift and Pitching Moment Coefficient Repeatability.

The effect of installing the winglet on the pitching moment curve will be discussed in Section 4.1. In conclusion, the comparison of the 'Van Uitert (ZZ Off)' results with the 'NWL' ones from this project suggest good repeatability.

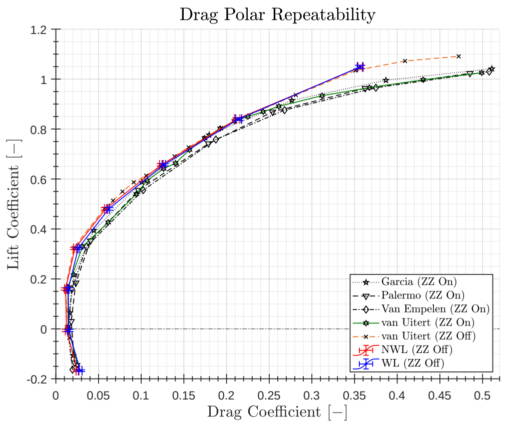

(a) Drag Polar Repeatability. The WL and NWL Results Include 95% Confidence Intervals. [14]

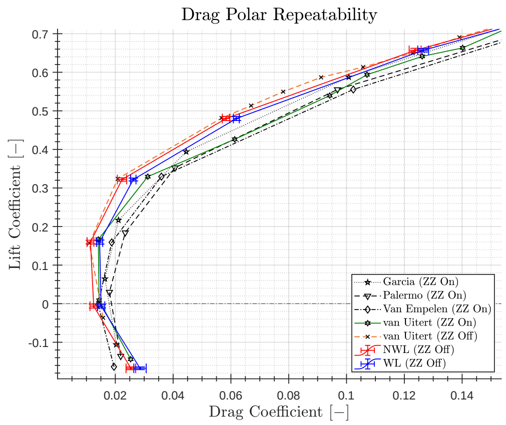

(b) Zoomed in Drag Polar Repeatability. The WL and NWL Results Include 95% Confidence Intervals. [14]

Figure 3.3: Drag Polar Repeatability.

The drag polars found in this research project and the previous ones are shown in Figures 3.3a and 3.3b. Those from this research project are plotted with 95% confidence intervals. One can immediately see that most of the results with the zig-zag strip installed had higher values of drag for the same lift coefficient. Thus, installing the zig-zag strip reduces the aerodynamic efficiency. Furthermore, in Figure 3.3a, one can see that the drag polar found by Van Uitert without the zig-zag very closely matches that of the NWL results, indicating good repeatability. The effects of installing the winglet will be described in Section 4.1.

3.5. Control Surface Deflection Measurements

To measure the control surface deflections that were tested in the wind tunnel, there were flat wooden profiles attached to them. The angles and change in angle of the control surfaces were measured by placing a angle meter on these wooden profiles. There were two profiles on each control surface and each measurement was repeated three times. This yields six measurements per control surface. Since the third control surface shown in Figure 2.1 had a broken servo during the wind tunnel test, it was manually fixed to the position of the second control surface during the campaign.

The measured control surface angles are plotted in Figure 3.4. In this figure, one can see each of the six measurements for each control surface, for each of the nine deflections. The mean (μ) and error bars spaced three times the sample standard deviation ($3s$) from the means are also shown in the plot. Finally, the mean and standard deviation of these measurements are reported in Table 3.2. This shows that the sample standard deviation for the measurements of the first and second control surface are below $0.1265°$ and below $0.608°$ for the rudder. The larger deviations can also be seen in the plot. Note that these measurements were made without aerodynamic loading on the wing.

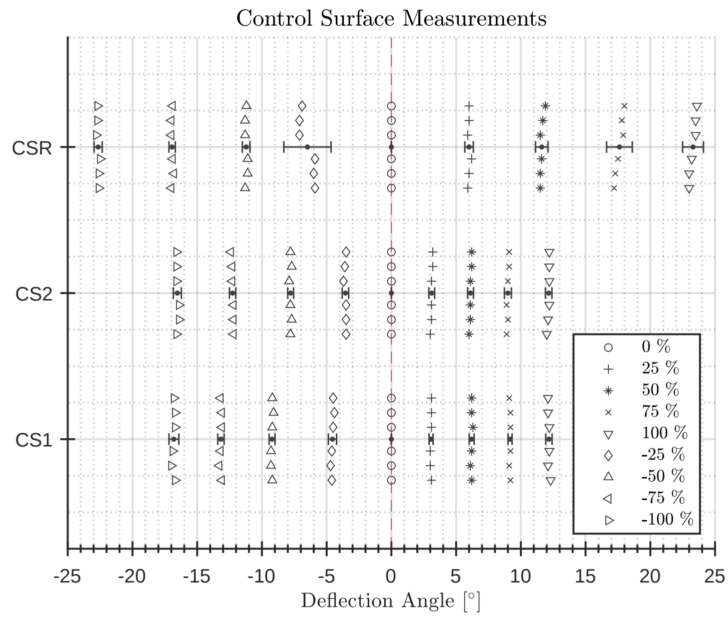

Figure 3.4: Control Surface Measurements, Including Mean and $3s$ Error Bars

Table 3.2: Control Surface Data Summary. CS3 Has Not Been Measured and is Assumed to be Equal to the CS2 Positions.

CS #	**Measure**	**Normalized CS Deflection (%)**								
		0	25	50	75	100	−25	−50	−75	−100
δ_{CS1}	μ [°]	0.00	3.07	6.20	9.17	12.17	−4.55	−9.22	−13.17	−16.80
	s [°]	0.00	0.0516	0.0632	0.0516	0.0816	0.1049	0.0753	0.0816	0.1265
δ_{CS2}	μ [°]	0.00	3.12	6.12	9.00	12.15	−3.55	−7.78	−12.27	−16.53
	s [°]	0.00	0.0753	0.0753	0.0894	0.0837	0.0837	0.0753	0.0816	0.1033
δ_{R}	μ [°]	0.00	6.00	11.62	17.62	23.30	−6.48	−11.22	−16.93	−22.65
	s [°]	0.00	0.1095	0.1602	0.3312	0.2683	0.6080	0.0983	0.0816	0.1049

4

Results

In this chapter, the effect of integrating the winglet on the aerodynamic coefficients of the Flying V are first described in Section 4.1. Next, the effect of deflecting the rudder on the aerodynamic coefficients are presented in Section 4.2. Then, rudder control derivatives for null CS1, CS2 and CS3 deflections are explained in Section 4.3. In Section 4.4, the effect of deflecting CS3 on the aerodynamic coefficients are calculated and in Section 4.5, the effect of deflecting the ailerons on the rudder control derivatives are presented. In Section 4.6, the effect of changing the airspeed on the rudder control derivatives are briefly considered. All sections other than 4.6 consider results obtained at the airspeed of $20\ \mathrm{m{\cdot}s{-}1}$.

4.1. Winglet Integration Effects

In this section, the winglet integration (WLI) effects on the aerodynamic coefficients are reported answering the first research question. The effects are shown by plotting the Flying V wind tunnel model's aerodynamic coefficients both with and without the winglet installed. Also, deltas are found by subtracting the results without the winglet installed from those with it. In this section, the rudder and main wing trailing edge control surfaces (CSR, CS1, CS2, CS3) are all set to zero and all results are 'corrected' according to Section 3.1.

4.1.1. Lift Coefficient

The lift coefficient of the Flying V before and after winglet integration can be seen in Figure 4.1a and the delta between the two is shown in Figure 4.1b. The delta referred to in this section is shown in Equation 4.1 and is the difference between the WL and NWL results. Note that the deltas for all coefficients in this section (4.1) are calculated in a similar fashion. Also note that Figures 4.1a and 4.1b plot the lift coefficient for the dual-wing Flying V as discussed in Section 2.3.1. As shown in the figures, the lift coefficient is not drastically affected by the winglet integration. The winglet integration seems to slightly decrease the lift coefficient at the higher angles of attack. This is thought to occur due to two phenomena. First, the increased pressure drag on the downward facing leading edge of the winglet could lower the lift and/or the winglet could contribute to increased separation at the tip of the outboard wing. According to Ref [31], the winglet and wing-winglet junction may be critical for low speed stall, in the absence of slats. It should be noted that neither the winglet or wing-winglet junction of this Flying V wind tunnel model have been optimized aerodynamically. In an experimental analysis of fences, droop and wingtip devices on a BWB configuration, a similar small reduction in lift was found for moderate angles of attack after the winglet was integrated [32]. As mentioned in Section 1.3, a properly designed winglet has been found to slightly increase the lift coefficient for first and second generation transport jets at transonic Mach numbers.

$$(\Delta_{C_L})_{\mathrm{WLI}} = (C_L)_{\mathrm{WL}} - (C_L)_{\mathrm{NWL}} \tag{4.1}$$

4.1.2. Drag Coefficient

The drag coefficient of the Flying V before and after winglet integration can be seen in Figure 4.2a and the delta between the two is shown in Figure 4.2b. WLI has slightly increased the drag coefficients for all

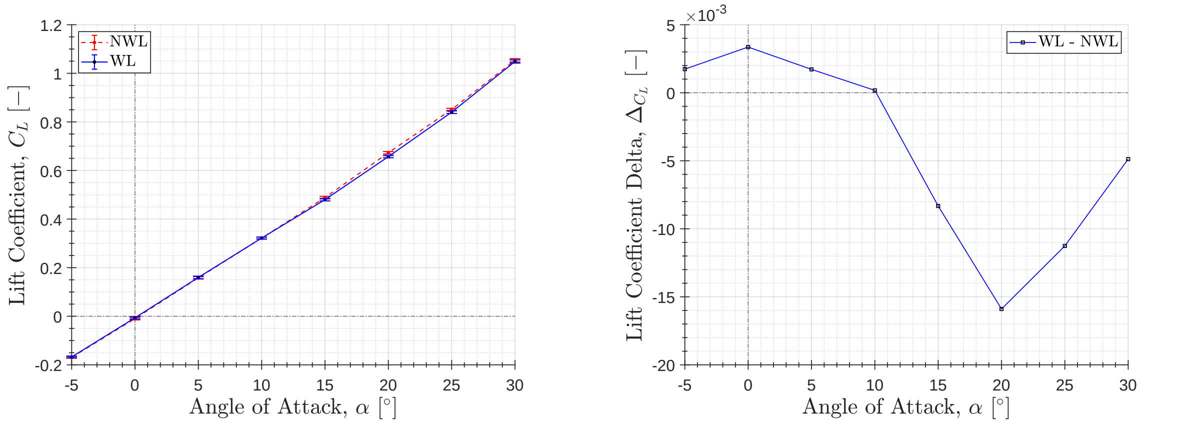

(a) Flying V Model Lift Coefficient Before and After WLI with 95 % Confidence Intervals. Corrected Dual-Wing Results.

(b) Flying V Model Lift Coefficient Delta Due to WLI. Corrected Dual-Wing Results.

Figure 4.1: Winglet Integration Effects on Lift Coefficient. Both Results are Corrected According to Section 3.1.

tested angles of attack until around 28° as shown in the figures. Additionally, the (untrimmed) drag polar is shown in Figure 4.3a. The increased drag at low angles of attack after WLI could be due to the airflow impinging on the newly introduced winglet structure, causing pressure and skin-friction drag on this aircraft component. This should be the reason for the increased zero-lift drag seen in the drag polar and this follows the theoretical and experimental trends explained in Section 1.3. Beyond 28°, it is thought that the winglet causes a reduction in the lift-induced (tip-vortex) drag by about the same amount as the increases in pressure and skin-friction drag due to itself. As explained in Section 1.3 the winglet effectiveness (amount of induced drag reduction) typically increases with lift coefficient. In Ref [32], two wingtip devices (winglet and C-Wing) were found to increase the zero-lift drag coefficient with respect to a baseline BWB configuration and lower the drag at higher lift coefficients. The untrimmed aerodynamic efficiency ($\frac{C_L}{C_D}$) plotted in Figure 4.3b shows that the winglet integration reduces the maximum lift-to-drag ratio from 14.4 to 12.3.

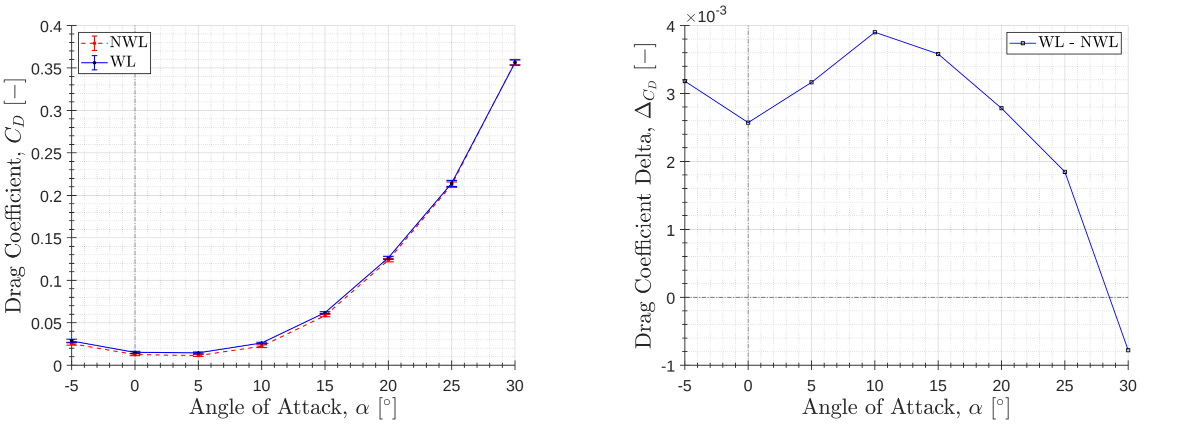

(a) Flying V Model Drag Coefficient Before and After WLI with 95% Confidence Intervals. Corrected Dual-Wing Results.

(b) Flying V Model Drag Coefficient Delta Due to WLI. Corrected Dual-Wing Results.

Figure 4.2: Winglet Integration Effects on Drag Coefficient. Both Results are Corrected According to Section 3.1.

4.1.3. Side-Force Coefficient

The side-force coefficient of the Flying V left wing before and after winglet integration can be seen in Figure 4.4a and the delta between the two is shown in Figure 4.4b. Note that the side-force coefficient and delta acting on only the left wing are plotted in the figures. As mentioned in Section 2.3.1, this is done because the side-force coefficient of the complete dual-wing Flying V is equal to 0 at all angles

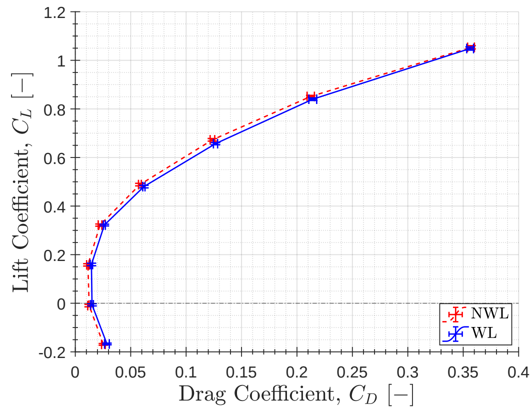

(a) Flying V Model Untrimmed Drag Polar Before and After WLI with 95% Confidence Intervals. Corrected Dual-Wing Results.

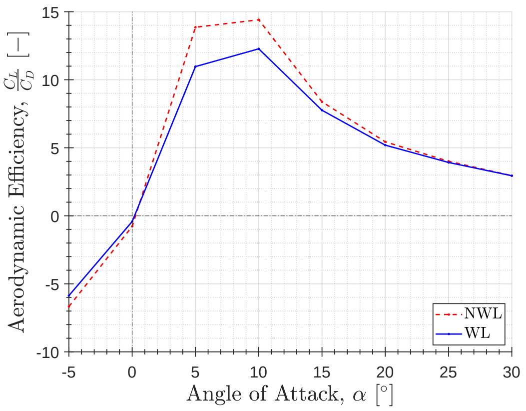

(b) Flying V Model Untrimmed Aerodynamic Efficiency Curves Before and After WLI. Corrected Dual-Wing Results.

Figure 4.3: Flying V Drag Polar and Aerodynamic Efficiency in Untrimmed Conditions. Both Results are Corrected According to Section 3.1.

of attack in symmetric conditions (no aileron or rudder input). Beyond $5°$ AoA, one can see that the side-force on the left wing generally decreases with increasing angle of attack. This means the left wing wants to translate leftward more and more with increasing angle of attack. This could be due to increasing suction near the highly swept leading edge of the left wing, pulling the wing to the left.

Below $5°$ angle of attack, WLI has decreased the side force acting on the left wing (causing leftward force). This is thought to be from an outboard flowing cross-flow on the upper surface impinging on the inner surface of the left wing's winglet. This could be due to a negative local angle of attack from the outboard wing twist $(-4.4°)$ and the low model angle of attack. Due to the outboard wing twist, the outboard wing chord should be aligned with the tunnel flow direction when the model is around $4.4°$ AoA and will generate little to no lift/circulation. Indeed, there seems to be no change to the side-force coefficient when the model is near $4.4°$ AoA in Figure 4.4b, indicating that the local flow is aligned with the winglet at this angle.

Between $5°$ and $25°$ WLI has increased the side-force acting on the left wing half-model (causing rightward force). This could be due to a tip-vortex emanating from the wingtip curling around and impinging the outer surface of the winglet as described in Section 1.3. This situation is illustrated in Figures 1.5a and 1.5b, showing the local flow direction, lift, drag and resultant forces acting on the winglet with the wing in a lifting condition. It is thought that this winglet side-force is increasing the model side-force. It should be noted that the winglet chord line on the Flying V WTM is not toed in or out, but is parallel with the root chord. Finally, beyond $25°$ angle of attack, WLI again reduces the side-force. This could be due to (parts of) the outboard wing beginning to stall, reducing the strength of the mentioned tip vortex impinging on the outer winglet surface. It seems that the tunnel flow is aligned with the winglet near the $5°$ and $25°$ angles of attack as there is little difference in left wing's side-force at these angles.

4.1.4. Rolling Moment Coefficient

The rolling moment coefficient of the Flying V before and after winglet integration can be seen in Figure 4.5a and the delta between the two is shown in Figure 4.5b. Note that the rolling moment coefficient and delta acting on only the left wing are plotted in the figures. As mentioned in Section 2.3.1, this is done because the rolling moment coefficient of the complete dual-wing Flying V is equal to 0 at all angles of attack in symmetric conditions (no aileron or rudder input). The difference between the rolling moment before and after WLI follows a similar trend as the difference in lift coefficient due to WLI for angles beyond $10°$. Assuming a constant spanwise center of pressure location before and after WLI, reduced lift on the left wing will reduce the rolling moment due to that wing. At angles below $5°$, the WLI has increased the lift but decreased the rolling moment (Figures 4.1b and 4.5b)! This is thought to be due to the outboard wing exhibiting an outward flowing crossflow which impinges on the left wing's inner winglet surface, causing a negative rolling moment. This outward crossflow in low lift conditions

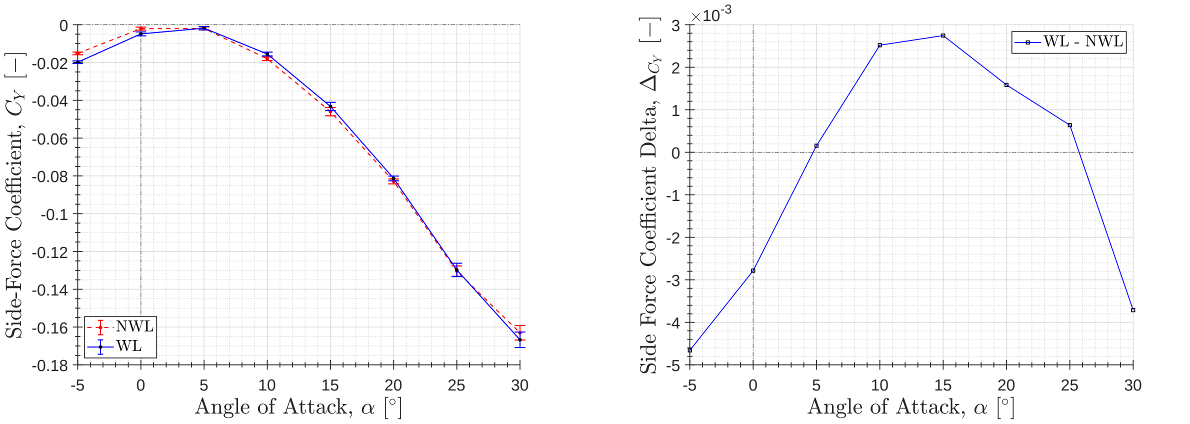

(a) Flying V Model Side-Force Coefficient Before and After WLI with 95% Confidence Intervals. Corrected Left Wing Only Results.

(b) Flying V Model Side-Force Coefficient Delta Due to WLI. Corrected Left Wing Only Results.

Figure 4.4: Winglet Integration Effects on Side-Force Coefficient. Both Results are Corrected According to Section 3.1.

was also mentioned when discussing the WLI effect on the side-force in Section 4.1.3.

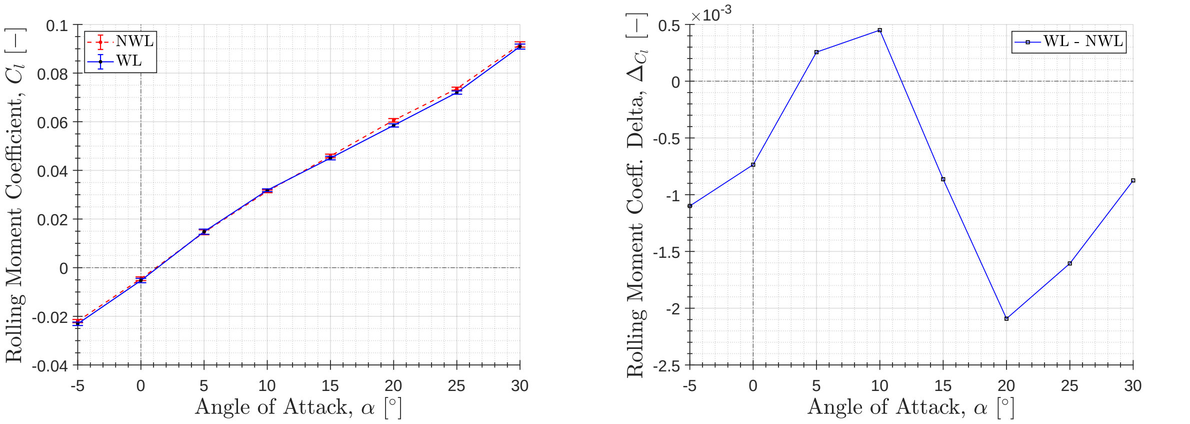

(a) Flying V Model Rolling Moment Coefficient Before and After WLI with 95% Confidence Intervals. Corrected Left Wing Only Results.

(b) Flying V Model Rolling Moment Coefficient Delta Due to WLI. Corrected Left Wing Only Results.

Figure 4.5: Winglet Integration Effects on Rolling Moment Coefficient. Both Results are Corrected According to Section 3.1.

4.1.5. Pitching Moment Coefficient

The pitching moment coefficient of the Flying V before and after winglet integration can be seen in Figure 4.6a and the delta between the two is shown in Figure 4.6b. Note that the pitching moment coefficient and delta acting on both wings are plotted in the figures. Below $5°$ angles of attack, the pitching moment coefficient is increased, perhaps due to the increased drag due to the WLI acting above the MR, pitching the aircraft upward. The WLI has also increased the pitching moment coefficient at the $15°$, $20°$, and $25°$ angles of attack. This could be due to reduced lift on the outboard wing at these angles of attack due to WLI as noted in Section 4.1.1. The Flying V WLI could lead to earlier separation of the main wing near the tip due to interference as the Flying V winglet has not (yet) been aerodynamically optimized. As noted in Section 1.3, the performance benefit due to the winglet depends on the toe angle, which in turn affects the tip loading of the main wing [16].

WLI has caused the angle of attack for pitch instability $(\frac{dC_m}{d\alpha} > 0)$ to be reduced to $10°$ *at this MR position*. This is attributed to the reduced lift on the outboard wing as previously mentioned. Note that if the MR is moved forward to $x_{MR} = 1.33$ m, similar differences in pitching moment due to WLI are present, but there is only a very slight pitching moment instability at $20°$. This is plotted in Figure A.13a, shown in Appendix A.3. At angles beyond $30°$ AoA, the pitching moment starts to steeply increase again for both MR positions, but this is not shown in this report.

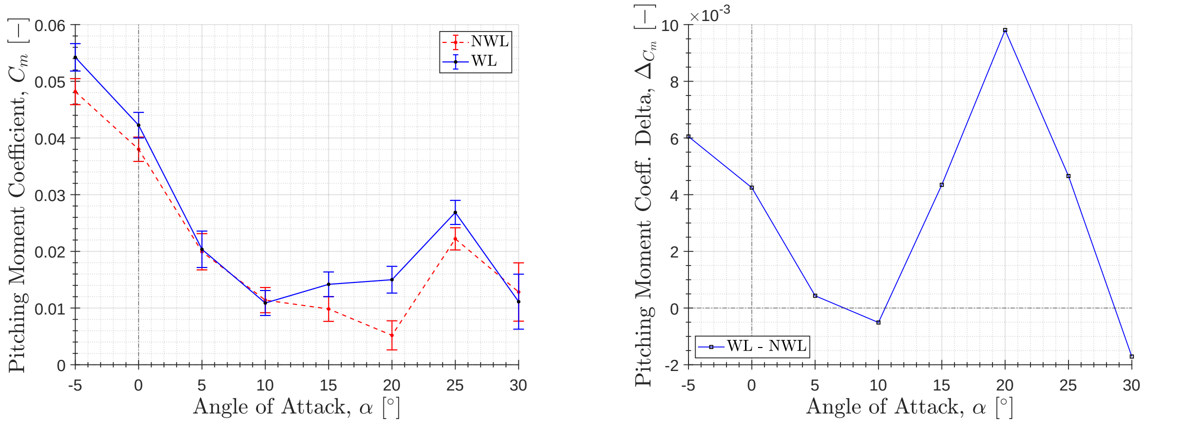

(a) Flying V Model Pitching Moment Coefficient Before and After WLI with 95% Confidence Intervals. Corrected Dual-Wing Results.

(b) Flying V Model Pitching Moment Coefficient Delta Due to WLI. Corrected Dual-Wing Results.

Figure 4.6: Winglet Integration Effects on Pitching Moment Coefficient. Both Results are Corrected According to Section 3.1.

4.1.6. Yawing Moment Coefficient

The yawing moment coefficient of the Flying V before and after winglet integration can be seen in Figure 4.7a and the delta between the two is shown in Figure 4.7b. Note that the yawing moment coefficient and delta acting on only the left wing are plotted in the figures. Below around 2.5° angle of attack, WLI has increased the yawing moment coefficient (nose right), which is in line with the reduction of side-force coefficient in Figure 4.4a. It was argued that an outboard flowing cross-flow on the upper wing surface was impinging on the inner winglet surface of the left wing, decreasing the side-force and increasing the yawing moment at negative/low angles of attack. Since this reduction in side-force is assumed to act at the winglet (force pushing left winglet leftward), aft of the MR, the yawing moment is increased and the aircraft wants to yaw right. The opposite is thought to occur between 2.5° and 15° angle of attack.

Furthermore, at 5° AoA, the side-force before and after WLI are nearly identical but this is not the case for the yawing moment. At 5° AoA the yawing moment after WLI is lower, most likely due to the newly introduced drag of the winglet acting far outboard with respect to the MR, causing a negative (nose-left) yawing moment. From 15° to 20°, the yawing moment of the left wing before and after WLI are very similar. Beyond 20°, WLI has increased the yawing moment coefficient of the left wing.

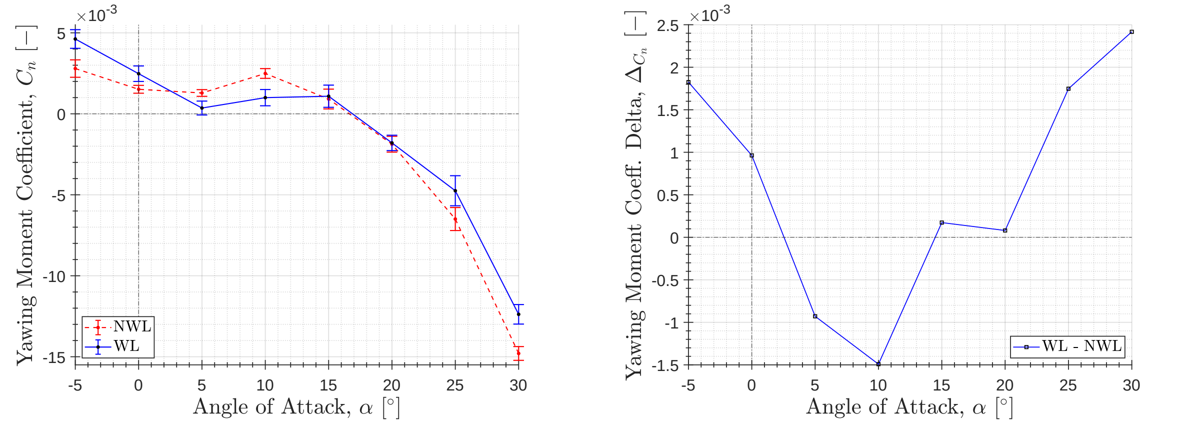

(a) Flying V Model Yawing Moment Coefficient Before and After WLI with 95% Confidence Intervals. Corrected Left Wing Only Results.

(b) Flying V Model Yawing Moment Coefficient Delta Due to WLI. Corrected Left Wing Only Results.

Figure 4.7: Winglet Integration Effects on Yawing Moment Coefficient. Both Results are Corrected According to Section 3.1.

4.2. Rudder Deflection Effects

In this section, the aerodynamic coefficients are plotted for various rudder deflections while $\bar{\delta}_{\mathrm{CS1}}$ = $\bar{\delta}_{\mathrm{CS2}}$ = $\bar{\delta}_{\mathrm{CS3}}$ = 0% and this will answer the second research question in part. All results in this section will concern the left wing only. Looking at only the left wing will allow for a determination of the change in aerodynamic coefficients on one wing for positive and negative rudder positions. Looking at only the change in aerodynamic coefficients of the left wing due to the (left wing's) rudder deflection will separate the effect of one wing's rudder moving inward toward the wing root while the other wing's rudder moves outward. This will also be done when analyzing the effect of the CS3 deflection on the aerodynamic coefficients in Section 4.4. More information about the half-wing vs. dual-wing results can be found in Section 2.3.1. Note that in the section on rudder control derivatives, the dual-wing results will be presented as this is more appropriate for comparison to historical data and interpretation of flight implications.

4.2.1. CSR Effect on Lift Coefficient

The lift coefficient of the Flying V for various rudder positions can be seen in Figure 4.8a and the change in lift coefficient between the deflected and undeflected cases are shown in Figure 4.8b. The change/deltas in Figure 4.8b are calculated with Equation 4.2 for each of the 8 non-zero rudder deflections. The deltas for the other aerodynamic coefficients in Section 4.2 are also calculated in this way. As mentioned above, the left wing only results are plotted here to separate the effect of the one rudder moving inward and the other outward on the dual-wing aircraft. Note that the red curve labelled 'NWL' is not the same as the red curve in Figure 4.1a, as this one is only half of the wing. Furthermore, the left wing's lift coefficient after WLI is plotted in blue and labelled '$\bar{\delta}_{\mathrm{R}} = 0$' in Figure 4.8a. The lift coefficient of the left wing with its rudder at the other normalized deflections form the remaining curves in the figure.

$$\left(\Delta_{C_L}\right)_{\delta_{\mathrm{R}}\neq 0} = \left(C_L\right)_{\delta_{\mathrm{R}}\neq 0} - \left(C_L\right)_{\delta_{\mathrm{R}}=0} \tag{4.2}$$

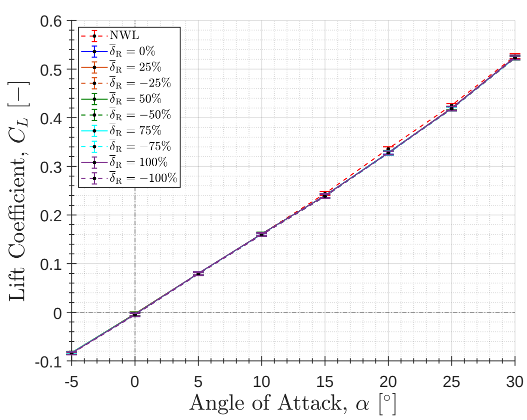

(a) Flying V Model Lift Coefficient for Various Rudder Deflections with 95% Confidence Intervals. Corrected Left Wing Only Results.

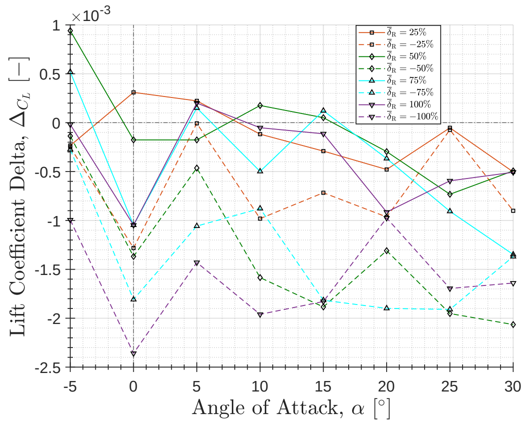

(b) Flying V Model Lift Coefficient Deltas Due to Various Rudder Deflections. Corrected Left Wing Only Results.

Figure 4.8: Flying V Lift Coefficient for Various Rudder Deflections and Their Deltas.

Note that the lift coefficient of the left wing is not the same for cases where the rudder is deflected trailing edge left (positive) or trailing edge right (negative), mainly due to asymmetry of the flow around the winglet. This is where the deltas in Figure 4.8b come in handy. When looking at negative rudder deflections (dotted lines), they all seem to decrease the lift coefficient. This is thought to occur due to flow interference. As the rudder on the left wing moves to negative deflections (toward root), the pressure on the inner winglet surface will increase. Since the suction side of the wingtip is also in this vicinity, it can be said that this increased pressure also locally increases the pressure of the main wing suction surface near the tip/winglet. Increased pressures on the suction surface will reduce the lift and can cause earlier flow separation. Conversely, only a few of the positive rudder deflections marginally increase the lift coefficient between $-5°$ and $15°$. Note that the lift is not a force that is typically adjusted by using the rudders.

4.2.2. CSR Effect on Drag Coefficient

The drag coefficient of the Flying V for various rudder positions can be seen in Figure 4.9a and the deltas in drag coefficient between the deflected and undeflected cases are shown in Figure 4.9b. As mentioned above, the left wing only results are plotted here and the deltas are calculated in the same way as the lift coefficient in Equation 4.2. For angles of attack up to $25°$, almost every negative rudder deflection (TE inward) causes more drag than the same % rudder deflection in the positive (TE outward) direction. Note that this drag imbalance causes a yawing moment which acts in the opposite direction as that induced by (the side-forces due to) rudder deflections. As mentioned in Section 4.2.1 on the rudder effect on the lift, negative rudder deflections are thought to promote separation near the main wing tip due to increased pressures on the winglet inner (and thus main wing tip suction) surface. This could explain the relatively higher drag of the inward/negative rudder deflections with respect to the outward/positive ones.

Increasing positive rudder deflections seem to neatly shift the drag delta up, with each rudder deflection delta following a similar trend with AoA. This is also the case for all the negative rudder deflections besides the -25% rudder deflection delta curve. Beyond $20°$ AoA, the trend of the -25% rudder deflection delta curve changes. At $25°$ AoA, the left wing with -25% rudder deflection has more drag than the left wing with -50% or -75% rudder deflections. Furthermore, at $30°$ AoA, the left wing with -25% rudder deflection still has more drag than that with -50% rudder deflection. As the flow field is quite complex at these higher angles of attack, it is not directly clear what is causing this phenomena. It is hypothesized that the effective camber line of the rudder with -25% rudder deflection is less aligned with the local airflow with respect to the other deflections at the mentioned angles of attack, causing higher drag.

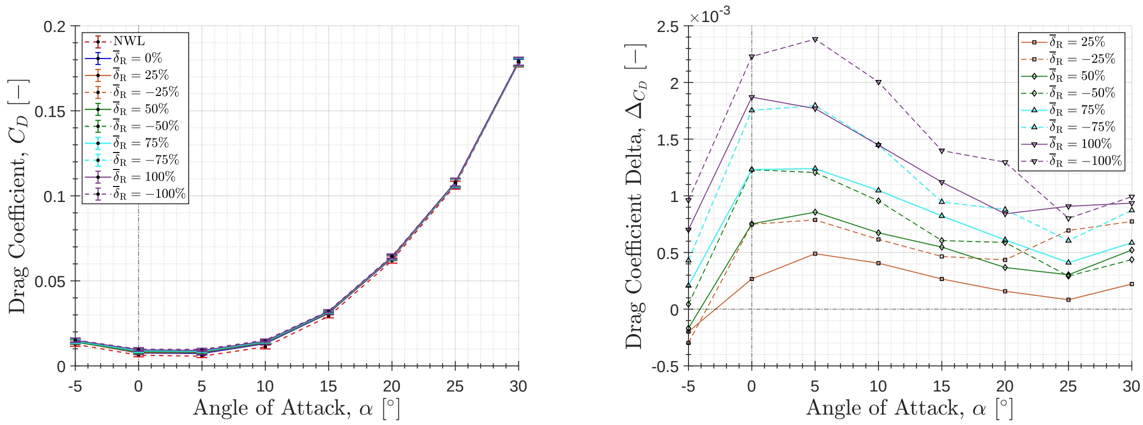

(a) Flying V Model Drag Coefficient for Various Rudder Deflections with 95% Confidence Intervals. Corrected Left Wing Only Results.

(b) Flying V Model Drag Coefficient Deltas Due to Various Rudder Deflections. Corrected Left Wing Only Results.

Figure 4.9: Flying V Drag Coefficient for Various Rudder Deflections and Their Deltas. Corrected Left Wing Only Results.

4.2.3. CSR Effect on Side-Force Coefficient

The side-force coefficients and deltas due to the rudder deflections for the *left wing* of the Flying V model are shown in Figures 4.10a and 4.10b, respectively. Looking at the figures, one can tell that the rudders are most effective at low angles of attack. This could be due to the sweep of the winglet leading edge and hinge line; as the angle of attack is increased, the winglet leading edge becomes more and more swept with respect to the oncoming flow, reducing the winglet lift curve slope and trailing edge surface (rudder) effectiveness.

As previously mentioned, a negative rudder deflection on the left wing moves the trailing edge toward the wing root, causing a negative side force increment (leftward force) and positive (nose-right) yawing moment. This is the case for most of the data in Figure 4.10b, however, as with the drag coefficient, interesting phenomena are found at the $25°$ and $30°$ angles of attack with negative rudder deflections. First, at $25°$ AoA, the -25% and -50% rudder deflections *increase* the side-force coefficient (positive delta)! Furthermore, at $30°$ AoA, a positive and negative rudder deflection of $\pm 25\%$ on the left wing *both* increase the side-force coefficient by a similar amount. As mentioned, opposite direction rudder deflections should have the opposite effect on the side-force so this phenomena will be referred to as a single wing control reversal. Finally, at $30°$ *all* negative rudder deflections increase the side-force. Note that the positive rudder deflections still generate positive side-force coefficient deltas larger in magnitude than the single wing control reversal. It is important to note that the complete/dual-wing Flying V side-force delta will equal the difference of the left wing side-force deltas for the left and right wing conditions shown in Equation 2.21. Since the magnitude of the side-force deltas due to positive deflections are larger than that of the control reversal, the complete Flying V will still generate a side-force in the intended direction by deflecting both rudder control surfaces at $30°$ AoA. This can be seen in Figure 4.14 for the dual-wing Flying V Side-Force rudder control derivative.

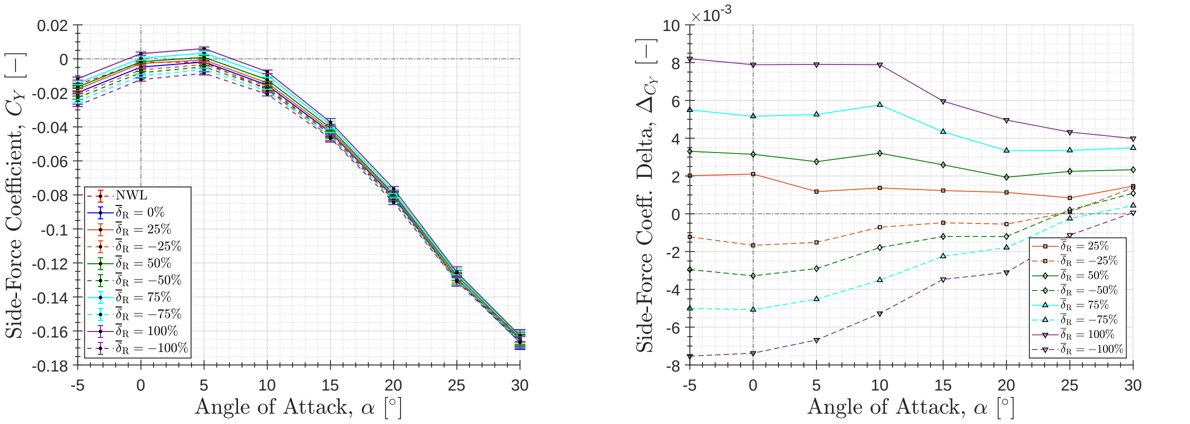

(a) Flying V Model Side-Force Coefficient for Various Rudder Deflections with 95% Confidence Intervals. Corrected Left Wing Only Results.

(b) Flying V Model Side-Force Coefficient Deltas Due to Various Rudder Deflections. Corrected Left Wing Only Results.

Figure 4.10: Flying V Side-Force Coefficient for Various Rudder Deflections and Their Deltas. Corrected Left Wing Only Results.

4.2.4. CSR Effect on Rolling Moment Coefficient

The rolling moment coefficients and deltas for various rudder deflections on the *left wing* of the Flying V model are shown in Figure 4.11a and 4.11b, respectively. Firstly, positive rudder deflections (trailing edge left) generally increase the rolling moment and negative rudder deflections generally decrease the rolling moment coefficient. This is logical, since the winglet center of pressure is above the MR and the side-force delta increases with positive rudder deflections (Figure 4.10b). Stated differently, as the left wing's rudder is deflected to positive deflections, the side-force due to the winglet/rudder above the MR is increasing, increasing the rolling moment (positive rolling moment is left wing up). The left wing rolling moment also encounters a control reversal phenomena at $30°$ AoA. Here, the smaller three of the four positive rudder deflections end up *decreasing* rolling moment coefficient at $30°$, with respect to the left wing with null rudder deflection. Like the side-force coefficient, the dual-wing Flying V rolling moment delta will equal the difference of the left wing rolling moment deltas for the left and right wing conditions shown in Equation 2.22. Since the magnitude of the rolling moment deltas due to negative deflections are larger than that of the control reversal, the complete Flying V will still generate a positive rolling moment due to rudder deflection by deflecting both rudder control surfaces at $30°$ AoA. This can be seen in Figure 4.16 by the positive dual-wing Flying V rolling moment rudder control derivative at all angles of attack.

4.2.5. CSR Effect on Pitching Moment Coefficient

The pitching moment coefficients and deltas for various rudder deflections on the *left wing* of the Flying V model are shown in Figure 4.12a and 4.12b, respectively. One can see from the figures that the rudder deflections generally increase the pitching moment. This thought to be due to two main reasons.

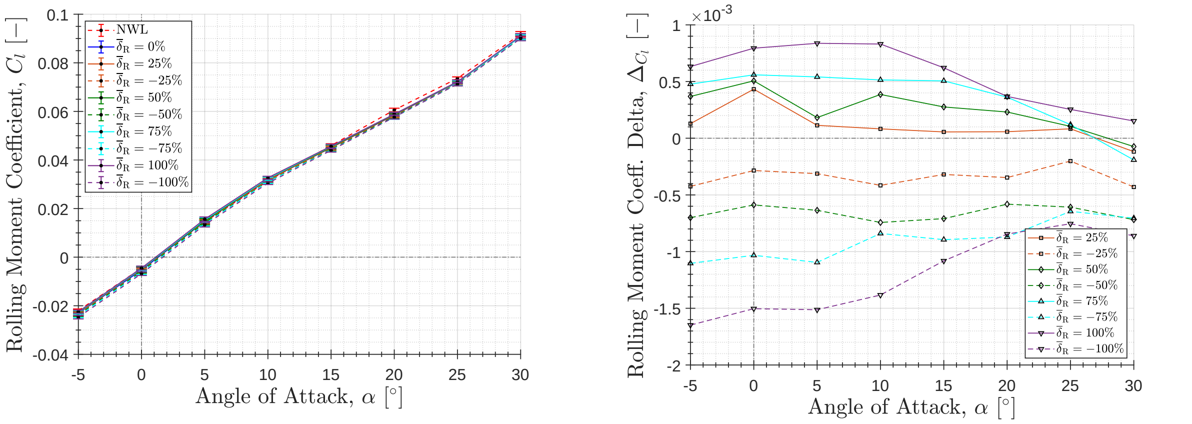

(a) Flying V Model Rolling Moment Coefficient for Various Rudder Deflections with 95% Confidence Intervals. Corrected Left Wing Only Results.

(b) Flying V Model Rolling Moment Coefficient Deltas Due to Various Rudder Deflections. Corrected Left Wing Only Results.

Figure 4.11: Flying V Rolling Moment Coefficient for Various Rudder Deflections and Their Deltas. Corrected Left Wing Only Results.

Firstly, as noted in Section 4.2.1, it was shown that rudder deflections generally reduce the lift; with negative deflections reducing the lift by larger magnitude than positive deflections in Figure 4.8b. It was hypothesized that the larger lift reduction with negative rudder deflections (TE inward) was due to interference increasing the pressure on the suction surface of the main wing tip region. Looking at the pitching moment deltas in Figure 4.12b confirms this hypothesis as the negative rudder deflections generally correspond with the higher increases in pitching moment. Secondly, the increased drag acting above the MR due to the rudder deflections in either direction, as shown in Figure 4.9b, will generally increase the pitching moment.

Interestingly, at 25° AoA, all four positive rudder deflections have been found to slightly decrease the pitching moment coefficient in Figure 4.12b. Back in Section 4.1.3 it was argued that the local flow near the winglet is somewhat aligned with the winglet around 25° AoA as the side-force delta between the configurations with and without the winglet was near-zero (Figure 4.4b). If this is indeed the case, positive rudder deflections (TE outward) could constructively interfere with local wing tip flow, causing higher suction on the main wing upper surface and thus decreasing the pitching moment. This is the opposite of the effect mentioned in the last paragraph regarding the negative rudder deflections.

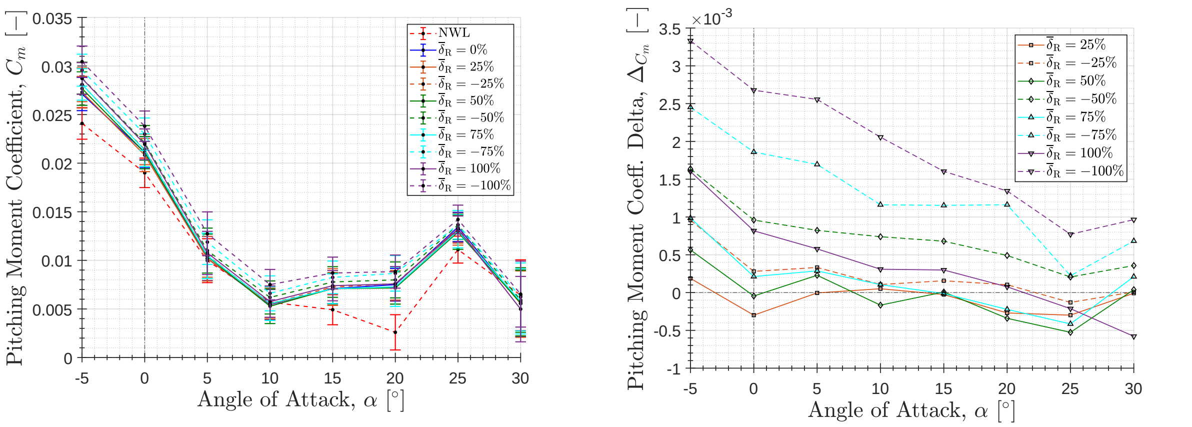

(a) Flying V Model Pitching Moment Coefficient for Various Rudder Deflections with 95% Confidence Intervals. Corrected Left Wing Only Results.

(b) Flying V Model Pitching Moment Coefficient Deltas Due to Various Rudder Deflections. Corrected Left Wing Only Results.

Figure 4.12: Flying V Pitching Moment Coefficient for Various Rudder Deflections and Their Deltas. Corrected Left Wing Only Results.

4.2.6. CSR Effect on Yawing Moment Coefficient

The yawing moment coefficients and deltas for various rudder deflections on the *left wing* of the Flying V model are shown in Figure 4.13a and 4.13b, respectively. As expected, positive rudder deflections cause a negative yawing moment coefficient (nose left) and vice-versa. Also, as the angle of attack is increased, the rudder effectiveness is reduced. This was also noted for the side force delta in Figure 4.10b. The magnitudes of the yawing moment deltas for the positive deflections are generally greater than that those for the same % negative deflection. In other words, the rudder is more effective at generating a yawing moment per unit angle of deflection when deflected in a positive direction with respect to a negative deflection. The effect of both rudders on the dual-wing aircraft yawing moment is shown in Figure 4.15, with the yawing moment rudder control derivative.

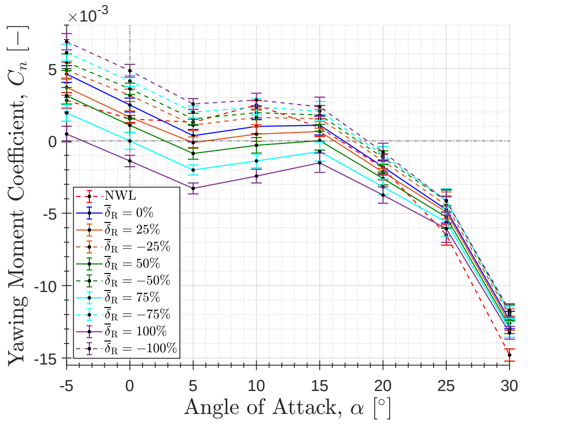

(a) Flying V Model Yawing Moment Coefficient for Various Rudder Deflections with 95% Confidence Intervals. Corrected Left Wing Only Results.

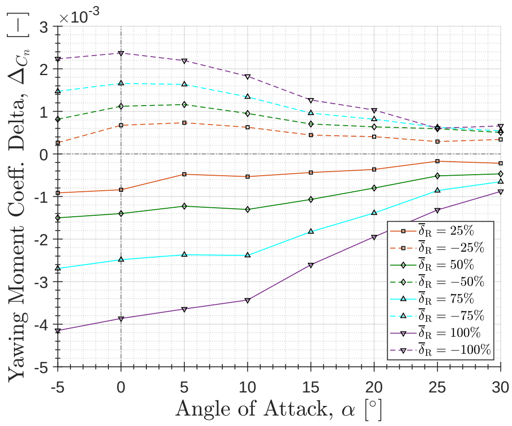

(b) Flying V Model Yawing Moment Coefficient Deltas Due to Various Rudder Deflections. Corrected Left Wing Only Results.

Figure 4.13: Flying V Yawing Moment Coefficient for Various Rudder Deflections and Their Deltas. Corrected Left Wing Only Results.

4.3. Rudder Control Derivatives

Three rudder control derivatives are extracted from the data and linearized in this section. These correspond to the changes in side-force ($C_{Y_{\delta_R}}$), yawing moment ($C_{n_{\delta_R}}$) and rolling moment ($C_{l_{\delta_R}}$) with respect to the rudder deflection. Here, the control derivatives will be for the dual-wing Flying V as this will include the rudder effect of both wings and is more appropriate for comparison to historical data and interpretation of flight implications. The dual-wing control derivatives are found by adding the deltas due to the left wing's rudder deflection to that of the right wing. Note that the rudders of the left and right wings move to the same % normalized deflection but oppositely with respect to the wing root. All results in this section consider the condition of zero CS1, CS2 and CS3 deflections.

4.3.1. Side-Force Rudder Control Derivative

The side-force control derivative for the dual-wing Flying V due to rudder deflections on both wings are shown in Figure 4.14. The solid lines are the measurements of the change in side-force due to rudder deflections at various angles of attack while the dotted lines are corresponding linear approximations. The characteristics of the linear approximations are given below in Table 4.1. For a given rudder deflection (along x-axis), both rudders move with the trailing edges in the same direction to generate side-forces in the same direction. This plot thus shows the expected change in side force on the SFTM due to rudder deflections at $0°$ sideslip conditions. As previously mentioned, if the SFTM is in a $+25\%$ rudder deflection condition, the left wing rudder moves outward and the right wing's rudder moves inward. Arriving at the dual-wing conditions from the half-wing tests has been explained in Section 2.3.1. The dual wing side-force due to a rudder deflection is essentially the distance between the lines of corresponding positive and negative rudder deflection deltas in Figure 4.10b.

It can be seen in Figure 4.14 that the change in side-force per unit rudder deflection (slope), also known as the side-force rudder control derivative ($C_{Y_{\delta_R}}$), decreases with increasing angle of attack. The last table column with label '$\Delta(C_{Y_{\delta_R}})_{\alpha=0}$' is the percent change in slope of the control derivative at that angle of attack with respect to the $0°$ AoA case. At $20°$ AoA, the effect of the rudder deflection on the dual-wing side-force coefficient is reduced by about half with respect to the $0°$ AoA case. This trend can also be seen in the plot of the single-wing side-force deltas in Figure 4.10b by the reduction in distance between corresponding positive and negative deflections with AoA. Looking at the figure and the R^2 values in Table 4.1, one can see that the linear approximation fits best for the low angles of attack and worst for the highest AoA, $30°$.

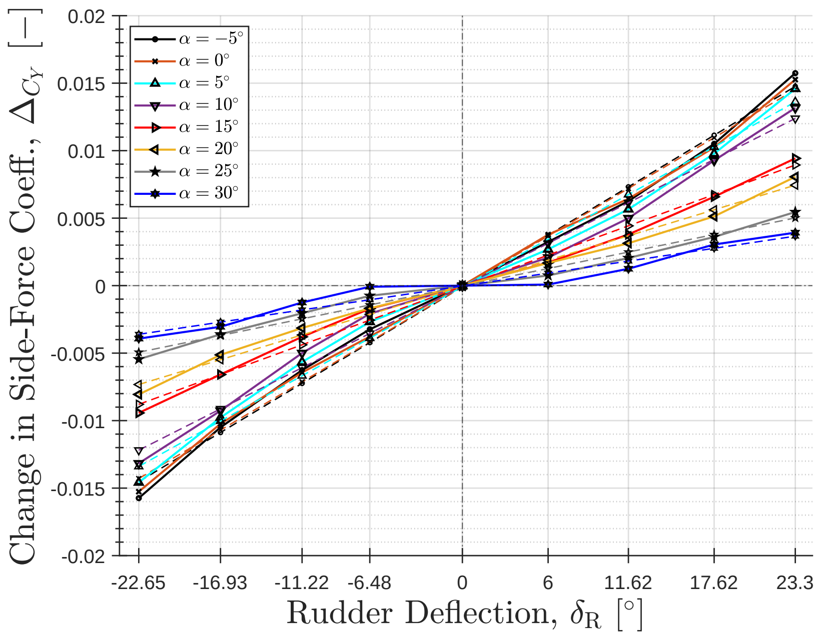

Figure 4.14: Side-Force Rudder Control Derivative for Dual-Wing Flying V. Corrected Results.

Table 4.1: Side-Force Rudder Control Derivative Linearization. The Last Column Indicates the Change in $C_{Y_{\delta_R}}$ at the Indicated AoA With Respect to That at 0 AoA in Percent.

α [°]	$C_{Y_{\delta_R}}$ [deg^{-1}]	$C_Y(\delta_R = 0)$ [−]	R^2 [−]	$\Delta\left(C_{Y_{\delta_R}}\right)_{\alpha=0}$ [%]
−5	$6.38 \cdot 10^{-4}$	$-8.92 \cdot 10^{-5}$	0.9923	1.62
0	$6.27 \cdot 10^{-4}$	$-8.78 \cdot 10^{-5}$	0.9956	0
5	$5.88 \cdot 10^{-4}$	$-8.22 \cdot 10^{-5}$	0.99	−6.29
10	$5.35 \cdot 10^{-4}$	$-7.49 \cdot 10^{-5}$	0.9873	−14.71
15	$3.86 \cdot 10^{-4}$	$-5.40 \cdot 10^{-5}$	0.9918	−38.47
20	$3.21 \cdot 10^{-4}$	$-4.50 \cdot 10^{-5}$	0.9899	−48.74
25	$2.17 \cdot 10^{-4}$	$-3.03 \cdot 10^{-5}$	0.9830	−65.47
30	$1.58 \cdot 10^{-4}$	$-2.22 \cdot 10^{-5}$	0.9496	−74.77

4.3.2. Yawing Moment Rudder Control Derivative

The yawing moment control derivative for the dual-wing Flying V due to rudder deflections on both wings are shown in Figure 4.15. The solid lines are the measurements of the change in yawing moment due to rudder deflections at various angles of attack while the dotted lines are corresponding linear approximations. The characteristics of the linear approximations are given below in Table 4.2. For a given rudder deflection (along x-axis), both rudders move with the trailing edges in the same direction to generate yawing moments in the same direction. This plot thus shows the expected change in yawing moment coefficient on the SFTM due to rudder deflections at $0°$ sideslip conditions. The dual wing yawing moment due to a rudder deflection is essentially the distance between the lines of corresponding positive and negative rudder deflection deltas in Figure 4.13b.

As mentioned earlier, positive aircraft rudder deflections generate negative yawing moments. It can be seen in Figure 4.15 that the change in yawing moment per unit rudder deflection (slope), also known as the yawing moment rudder control derivative ($C_{n_{\delta_R}}$), increases with increasing angle of attack. As the angle of attack is increased, a unit rudder deflection generates less of an increment in yawing moment. The last table column with label '$\Delta(C_{n_{\delta_R}})_{\alpha=0}$' is the percent change in slope of the control derivative at that angle of attack with respect to the $0°$ AoA case. At $20°$ AoA, the effect of the rudder deflection on the dual-wing yawing moment coefficient is again reduced by about half with respect to the $0°$ AoA case. This can also be seen in the plot of the single-wing yawing moment deltas in Figure 4.13b by the reduction in distance between corresponding positive and negative deflections with AoA. Comparing the last columns of Tables 4.1 and 4.2, the side-force and yawing moment have similar percent reductions in control power with AoA.

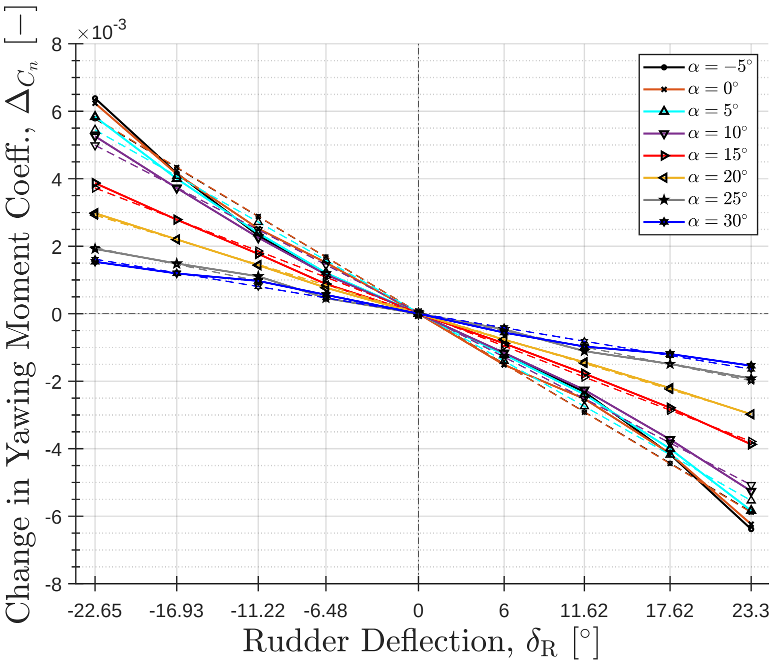

Figure 4.15: Yawing Moment Rudder Control Derivative for Dual-Wing Flying V. Corrected Results.

4.3.3. Rolling Moment Rudder Control Derivative

The rolling moment control derivative for the dual-wing Flying V due to rudder deflections on both wings are shown in Figure 4.16. The solid lines are the measurements of the change in rolling moment due to rudder deflections at various angles of attack while the dotted lines are corresponding linear approximations. The characteristics of the linear approximations are given below in Table 4.3.

For a given rudder deflection (along x-axis), both rudders move with the trailing edges in the same direction to generate yawing moments and side-forces in the same direction. As mentioned in Section 4.2.4 on the single wing effects of rudder deflections on the rolling moment, there are two main drivers for the influence of the rudder deflection on the rolling moment. First, a positive rudder deflection moves both rudders TE left and the resulting side-forces on the winglets act above the MR, generating positive rolling moments. Next, consider only the left wing; as the rudder is positively deflected (TE outward), the inner winglet surface pressures should decrease which also lowers the local pressure

Table 4.2: Yawing Moment Rudder Control Derivative Linearization. The Last Column Indicates the Change in $C_{n_{\delta_R}}$ at the Indicated AoA With Respect to That at 0 AoA in Percent.

α [°]	$C_{n_{\delta_R}}$ [deg^{-1}]	$C_n(\delta_R = 0)$ [−]	R^2 [−]	$\Delta\left(C_{n_{\delta_R}}\right)_{\alpha=0}$ [%]
−5	$-2.53 \cdot 10^{-4}$	$3.55 \cdot 10^{-5}$	0.9866	−0.28
0	$-2.54 \cdot 10^{-4}$	$3.56 \cdot 10^{-5}$	0.9940	0
5	$-2.39 \cdot 10^{-4}$	$3.35 \cdot 10^{-5}$	0.9940	−5.95
10	$-2.19 \cdot 10^{-4}$	$3.07 \cdot 10^{-5}$	0.9965	−13.81
15	$-1.63 \cdot 10^{-4}$	$2.29 \cdot 10^{-5}$	0.9981	−35.68
20	$-1.28 \cdot 10^{-4}$	$1.80 \cdot 10^{-5}$	0.9996	−49.54
25	$-8.57 \cdot 10^{-5}$	$1.20 \cdot 10^{-5}$	0.9964	−66.28
30	$-7.09 \cdot 10^{-5}$	$9.92 \cdot 10^{-6}$	0.9901	−72.12

on the main wing tip suction surface through interference. This further increases the rolling moment coefficient in a few conditions. Conversely, on the right wing under a positive rudder deflection (TE inward), the increased pressure on the inner winglet surface should increase the pressure on the main wing tip suction surface through interference. This further increases the rolling moment due to a rudder deflection. Due to these two phenomena, positive and negative rudder deflections do not have equal and opposite effects on the rolling moment delta, as shown in Figure 4.11b.

It can be seen in Figure 4.16 that the change in rolling moment per unit rudder deflection (slope), also known as the rolling moment rudder control derivative ($C_{l_{\delta_R}}$), decreases with increasing angle of attack. At 20° AoA, the effect of the rudder deflection on the dual-wing rolling moment coefficient is reduced by about 37% with respect to the 0° AoA case. This trend can also be seen in the plot of the single-wing yawing moment deltas in Figure 4.11b by the reduction in distance between corresponding positive and negative deflections with AoA. As can be seen with the R^2 values, higher angles of attack generally show increased non-linear trends of this control derivative.

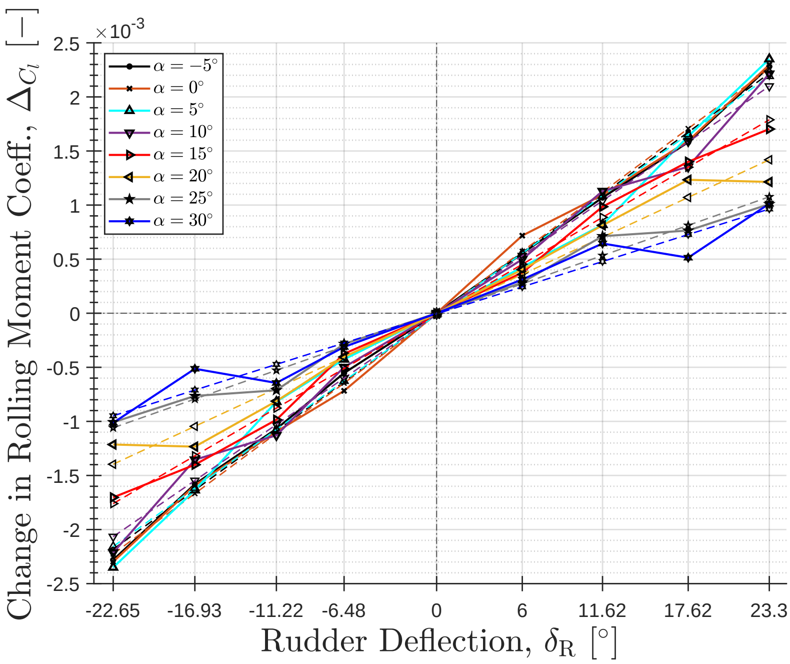

Figure 4.16: Rolling Moment Rudder Control Derivative for Dual-Wing Flying V. Corrected Results.

Table 4.3: Rolling Moment Rudder Control Derivative Linearization. The Last Column Indicates the Change in $C_{l_{\delta_R}}$ at the Indicated AoA With Respect to That at 0 AoA in Percent.

α [°]	$C_{l_{\delta_R}}$ [deg^{-1}]	$C_l(\delta_R = 0)$ [−]	R^2 [−]	$\Delta\left(C_{l_{\delta_R}}\right)_{\alpha=0}$ [%]
-5	$9.58 \cdot 10^{-5}$	$-1.34 \cdot 10^{-5}$	0.9982	-1.95
0	$9.77 \cdot 10^{-5}$	$-1.37 \cdot 10^{-5}$	0.9972	0
5	$9.47 \cdot 10^{-5}$	$-1.33 \cdot 10^{-5}$	0.9857	-3.1
10	$9.06 \cdot 10^{-5}$	$-1.27 \cdot 10^{-5}$	0.9906	-7.2
15	$7.72 \cdot 10^{-5}$	$-1.08 \cdot 10^{-5}$	0.9945	-20.93
20	$6.13 \cdot 10^{-5}$	$-8.58 \cdot 10^{-6}$	0.9784	-37.27
25	$4.65 \cdot 10^{-5}$	$-6.51 \cdot 10^{-6}$	0.9824	-52.41
30	$4.16 \cdot 10^{-5}$	$-5.83 \cdot 10^{-6}$	0.9527	-57.38

4.4. CS3 Deflection Effects

In this section, the effect of deflecting the outboard control surface (CS3) on the aerodynamic coefficients of only the left wing are presented. This is useful before describing the effects of aileron deflections on the rudder effectiveness. Since CS3 is defined to be an aileron, as one wing is deflected upward, the other is deflected downward. As mentioned in Section 4.2, only the left wing aerodynamic coefficients are presented in this section so that effects of the up and down deflections on opposite wings are separated. To prevent confusion with the aileron deflection signs, δ_{CS3} is used in this section to denote the left wing's CS3 position, positive trailing edge down. All results in this section are with the rudder and elevators at zero deflection (δ_R = δ_{CS12} = 0). Furthermore, the following results in this section are corrected: $\overline{\delta}_{\mathrm{CS3}} = 0\%$, $\overline{\delta}_{\mathrm{CS3}} = 25\%$, $\overline{\delta}_{\mathrm{CS3}} = -25\%$, $\overline{\delta}_{\mathrm{CS3}} = 50\%$ and $\overline{\delta}_{\mathrm{CS3}} = -50\%$. The $\overline{\delta}_{\mathrm{CS3}} = -75\%$, $\overline{\delta}_{\mathrm{CS3}} = 100\%$ and $\overline{\delta}_{\mathrm{CS3}} = -100\%$ are found with the gaps described in Section 3.1 closed. Finally, there is no mean or standard deviation for the $\overline{\delta}_{\mathrm{CS3}} = 75\%$ results because there is unfortunately only one run with the gaps closed consistently.

4.4.1. CS3 Effect on Lift Coefficient

The lift coefficient and deltas of only the left wing of the Flying V subject to CS3 deflections are plotted in Figures 4.17a and 4.17b, respectively. Again, the deltas in this section (4.4) are calculated with Equation 4.2, only using the conditions with CS3 deflected instead of the rudder. One can see from Figure 4.17b that positive CS3 deflections on the left wing (TE down) increase the lift coefficient in every condition besides the $\overline{\delta}_{\mathrm{CS3}} = +25\%$ deflection at the $25°$ and $30°$ angles of attack. This could be due to the slight 25% deflection stalling a larger portion of the outboard wing with respect to the undeflected case, while not increasing the pressure on the lower CS3 surface enough to overcome the loss. Similarly, almost every negative CS3 deflection (TE upward) decreases the lift, besides the -25% deflection at $20°$ AoA. Perhaps this negative deflection (TE up) reduces the local adverse pressure gradient and allows for a larger portion of attached flow, increasing the lift with respect to the undeflected case. As explained in Section 2.3.1, the dual-wing Flying V lift coefficient may be found by adding the curve of the right wing to that from the left one in Figure 4.17a. The delta of the dual-wing Flying V under an aileron input is found by adding the corresponding $\pm$ deltas in Figure 4.17b.

4.4.2. CS3 Effect on Drag Coefficient

The drag coefficient and deltas of only the left wing of the Flying V subject to CS3 deflections are plotted in Figures 4.18a and 4.18b, respectively. Looking at Figure 4.18b, one can see that at $-5°$ AoA, both positive and negative CS3 deflections decrease the drag with respect to the undeflected case. As the AoA increases, the positive CS3 deflections (TE downward) most often increase the drag much more than the corresponding negative deflection and the deltas increase with AoA. This is because positive deflections will increase the effective angle of attack and induced drag of the wing section by tilting the chord line.

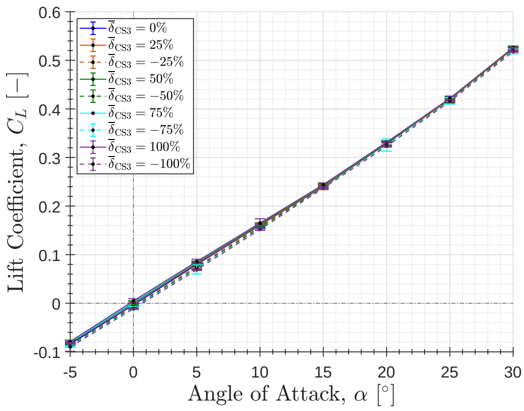

(a) Flying V Model Lift Coefficient for Various $\overline{\delta}_{CS3}$ Deflections with 95% Confidence Intervals. Left Wing Only Results.

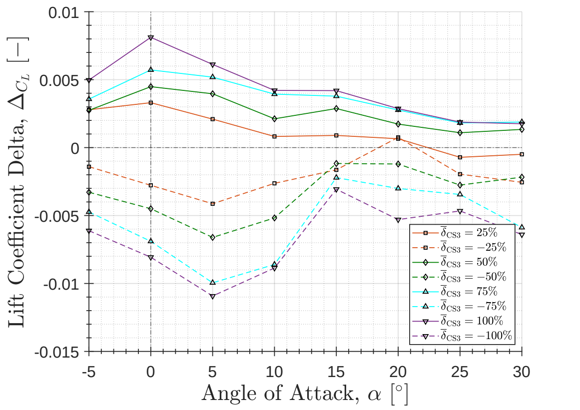

(b) Flying V Model Lift Coefficient Deltas for Various $\overline{\delta}_{CS3}$ Deflections. Left Wing Only Results.

Figure 4.17: Flying V Lift Coefficient for Various $\overline{\delta}_{CS3}$ Deflections and Their Deltas. Left Wing Only Results.

The drag coefficients of the -100% CS3 deflection at angles of attack at and below $5°$ are slightly higher than the corresponding positive deflection. This is thought to be related to the $-4.4°$ twist of the outboard wing. As mentioned in Section 4.1.3, it is reasoned that the local flow near the wing tip is aligned with the chord line of the outboard wing around $5°$ AoA. Thus, at angles below this, the outboard wing would be operating at a negative effective angle of attack. If this is the case, it makes sense that negative (TE upward) deflections increase the drag more than positive deflections as negative ones further reduce the negative effective angle of attack of the outboard wing, increasing the induced drag. The opposite effect is thought to be present for negative CS3 deflections at angles of attack beyond $5°$. With the outboard wing in a positive effective angle of attack condition, a negative CS3 deflection (TE up) will reduce the local effective angle of attack, reducing the induced drag. The profile drag is also influenced by CS3 deflection and this may be why the maximum drag reduction is found with the -75% deflection versus the -100% deflection at angles above $10°$. Here, the induced drag reduction going from -75% to -100% CS3 deflection is thought to be smaller in magnitude than the profile drag increase going from -75% to -100%.

The difference in drag for the left and right wings under corresponding $\pm$ percent CS3 deflections gives rise to a yawing moment. Looking at Figure 4.18b, when the positive deflection (solid line) has a larger delta than the corresponding percent deflection of negative sign, an adverse yawing moment occurs. For example, picture the dual-wing aircraft with a $+75\%$ aileron deflection at $5°$ AoA. As defined in Section 2.1.3, a positive aileron deflection causes a negative rolling moment (right wing up) and the intended direction is left. In this condition, the left wing has a negative CS3 deflection and the right wing a positive one. Looking at Figure 4.18b, one can see the left wing with negative deflection has lower drag than the right wing with positive deflection and this causes a positive yawing moment, nose right. Thus, the aileron input rolls the plane left while the adverse yaw due to the aileron input yaws the plane nose right. Note that increasing the aileron input from $+75\%$ to $+100\%$ at the same AoA of $5°$ changes the adverse yaw phenomena to one of proverse yaw. This is discussed further in Section 4.4.6 below.

4.4.3. CS3 Effect on Side-Force Coefficient

The side-force coefficient and deltas of only the left wing of the Flying V subject to CS3 deflections are plotted in Figures 4.19a and 4.19b, respectively. From Figure 4.19b, the positive CS3 deflections (TE down) increase the side-force coefficient (rightward force) at all angles of attack. The negative CS3 deflections decrease the side-force (leftward force) on the left wing until around $24°$ AoA, beyond which all negative deflections also increase the side-force coefficient. It is not clear why the trends at the lower angles of attack take place. At the higher angles of attack, it is hypothesized that increases in side-force due to both $\pm$ deflections are due to both control surface deflection directions diverting the flow outward, considering the sweep of the main wing control surfaces in Figure 2.1. Since the

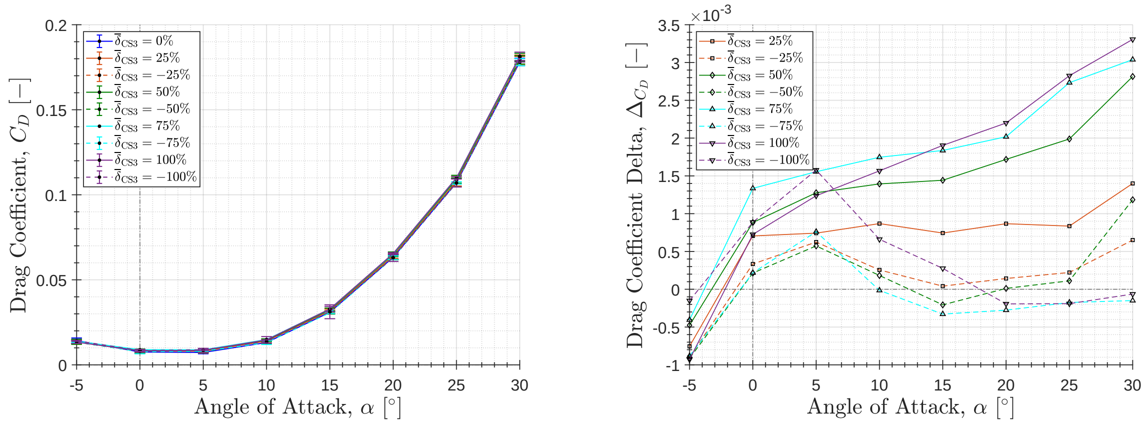

(a) Flying V Model Drag Coefficient for Various $\overline{\delta}_{CS3}$ Deflections with 95% Confidence Intervals. Left Wing Only Results.

(b) Flying V Model Drag Coefficient Deltas for Various $\overline{\delta}_{CS3}$ Deflections. Left Wing Only Results.

Figure 4.18: Flying V Drag Coefficient for Various $\overline{\delta}_{CS3}$ Deflections and Their Deltas. Left Wing Only Results.

side-force due to the $\pm$ aileron deflections are not of equal and opposite magnitude, aileron deflections will cause a side-force imbalance and thus contribute to the yawing moment.

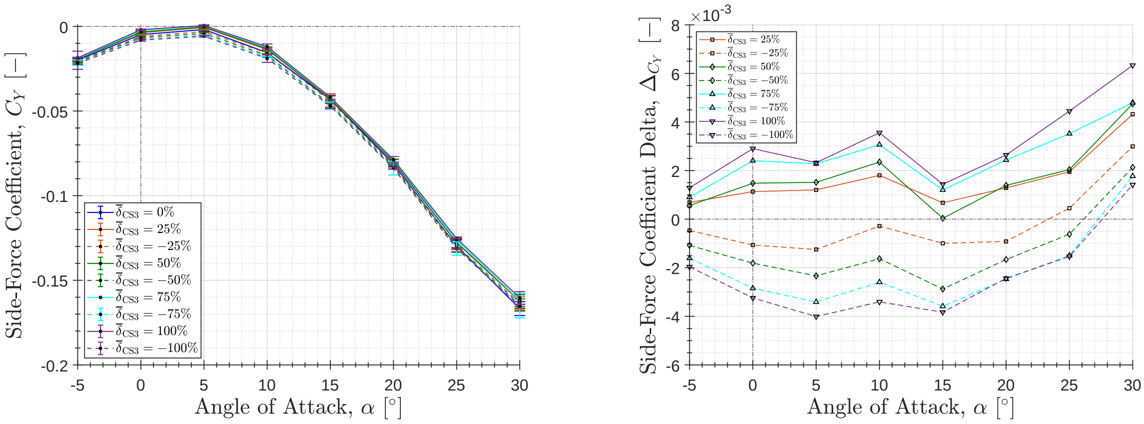

(a) Flying V Model Side-Force Coefficient for Various $\overline{\delta}_{CS3}$ Deflections with 95% Confidence Intervals. Left Wing Only Results.

(b) Flying V Model Side-Force Coefficient Deltas for Various $\overline{\delta}_{CS3}$ Deflections. Left Wing Only Results.

Figure 4.19: Flying V Side-Force Coefficient for Various $\overline{\delta}_{CS3}$ Deflections and Their Deltas. Left Wing Only Results.

4.4.4. CS3 Effect on Rolling Moment Coefficient

The rolling moment coefficient and deltas of only the left wing of the Flying V subject to CS3 deflections are plotted in Figures 4.20a and 4.20b, respectively. From Figure 4.20b, one can see that almost all of the AoA conditions with positive CS3 deflections (TE down) on the left wing increase the rolling moment (left wing up). At 30° AoA the smallest positive CS3 deflection (TE down) slightly decreases the rolling moment (left wing down), the opposite effect as intended. This could be due to this slight deflection stalling a larger portion of the outboard wing with respect to the undeflected case, while not increasing the pressure on the lower CS3 surface enough to overcome the loss. Note that a slight reduction in lift coefficient was indeed found at this condition in Figure 4.17b. For the negative CS3 deflections (TE up), these have all been found to decrease the rolling moment in Figure 4.20b, as intended. As explained in Section 2.3.1, the dual-wing Flying V rolling moment coefficient may be found by subtracting the curve of the right wing from that from the left one in Figure 4.20a. The rolling moment coefficient delta of the dual-wing Flying V under an aileron input is found by also subtracting the corresponding $\pm$ deltas in Figure 4.20b. This will form the rolling moment aileron control derivative which is not plotted in this report.

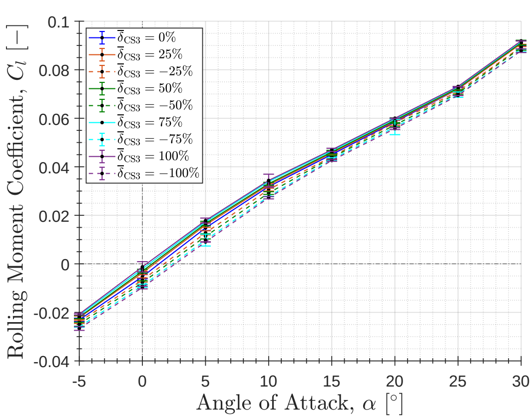

(a) Flying V Model Rolling Moment Coefficient for Various $\overline{\delta}_{CS3}$ Deflections with 95% Confidence Intervals. Left Wing Only Results.

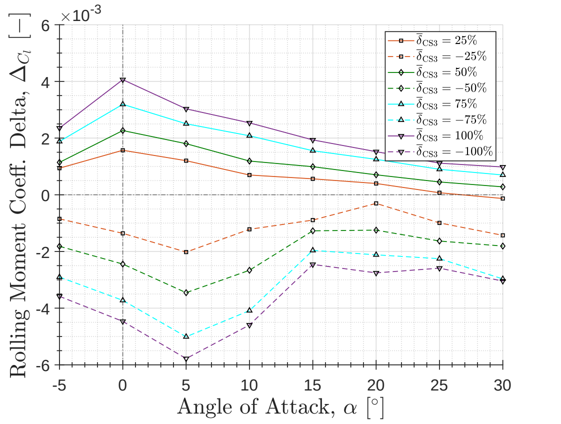

(b) Flying V Model Rolling Moment Coefficient Deltas for Various $\overline{\delta}_{CS3}$ Deflections. Left Wing Only Results.

Figure 4.20: Flying V Rolling Moment Coefficient for Various $\overline{\delta}_{CS3}$ Deflections and Their Deltas. Left Wing Only Results.

4.4.5. CS3 Effect on Pitching Moment Coefficient

The pitching moment coefficient and deltas of only the left wing of the Flying V subject to CS3 deflections are plotted in Figures 4.21a and 4.21b, respectively. One can see from both figures that positive deflections (TE down) decrease the pitching moment (nose down) at all angles of attack. For the negative CS3 deflections (TE up), the pitching moment is increased at all angles of attack, as expected. At $30°$, there is virtually no change in the pitching moment coefficient going from -75% to -100% CS3 deflection. This can also be seen with the minute changes in the lift and drag coefficient delta plots between these CS3 positions in Figures 4.17b and 4.18b, respectively.

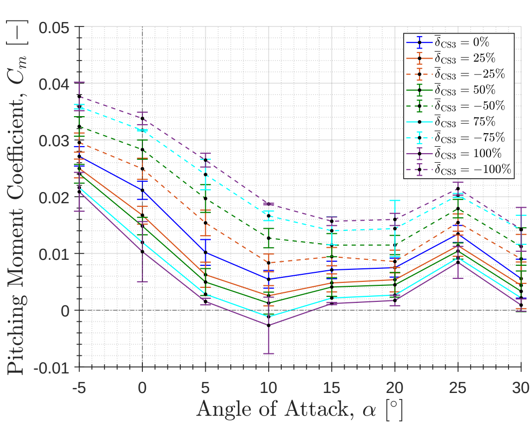

(a) Flying V Model Pitching Moment Coefficient for Various $\overline{\delta}_{CS3}$ Deflections with 95% Confidence Intervals. Left Wing Only Results.

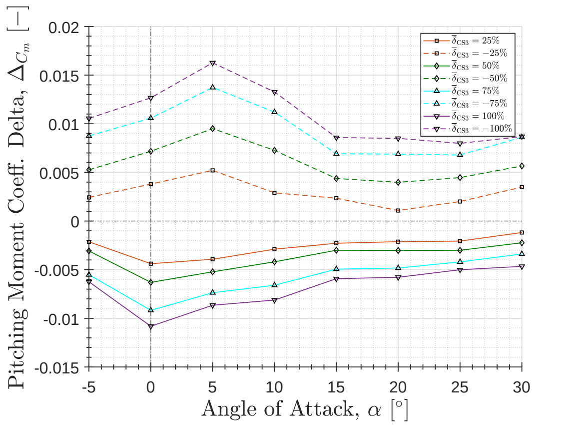

(b) Flying V Model Pitching Moment Coefficient Deltas for Various $\overline{\delta}_{CS3}$ Deflections. Left Wing Only Results.

Figure 4.21: Flying V Pitching Moment Coefficient for Various $\overline{\delta}_{CS3}$ Deflections and Their Deltas. Left Wing Only Results.

4.4.6. CS3 Effect on Yawing Moment Coefficient

The yawing moment coefficient and deltas of only the left wing of the Flying V subject to CS3 deflections are plotted in Figures 4.22a and 4.22b, respectively. Figure 4.22b is best read when looking at two corresponding $\pm$ deflections. Assuming the dual-wing aircraft has a $+25\%$ aileron deflection (right wing up), the left wing has a negative (TE up) and the right wing has a positive (TE down) CS3 deflection. As discussed in section 2.3.1, the dual-wing yawing moment is found by subtracting the right wing (solid line) from the left wing yawing moment coefficient. For the $\overline{\delta}_A = +25\%$ (roll left) example, the dual-wing yawing moment will be positive (nose right) for all angles of attack besides $30°$. These are conditions of adverse yaw mentioned in Section 4.4.2. The adverse yaw is due to the drag and side-force imbalances of the left and right wings under negative and positive CS3 deflections under a dual-wing aileron input. The adverse yaw due to aileron input is shown later in Section 4.5.2 when discussing the effect of aileron deflections on the yawing moment rudder control derivative. When looking at the $\overline{\delta}_A = +25\%$ example for the $30°$ AoA, there is proverse yaw. As can be seen in Figure 4.22b, the state of adverse or proverse yaw for the dual-wing aircraft depends on both the aileron deflection and angle of attack.

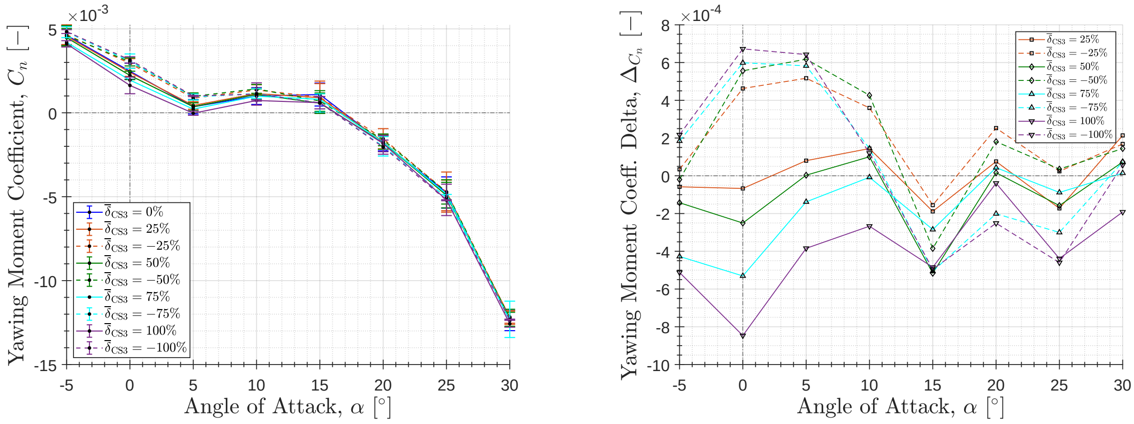

(a) Flying V Model Yawing Moment Coefficient for Various $\overline{\delta}_{\mathrm{CS3}}$ Deflections with 95% Confidence Intervals. Left Wing Only Results.

(b) Flying V Model Yawing Moment Coefficient Deltas for Various $\overline{\delta}_{\mathrm{CS3}}$ Deflections. Left Wing Only Results.

Figure 4.22: Flying V Yawing Moment Coefficient for Various $\overline{\delta}_{\mathrm{CS3}}$ Deflections and Their Deltas. Left Wing Only Results.

4.5. Aileron Effect on Rudder Control Derivatives

In this section, the rudder control derivatives from Section 4.3 are recalculated and plotted for various aileron deflections to answer the third research question. In this report, a $+25\%$ aileron deflection is referring to the left wing having a -25% CS3 deflection and the right wing having a $+25\%$ CS3 deflection. Like Section 4.3, the rudder control derivatives subject to aileron inputs will be plotted for the dual-wing Flying V to examine the effect of both wing control surfaces on aircraft behavior. All results in this section consider the condition of zero CS1 and CS2 deflections. Previously, the rudder effectiveness for all rudder positions and angles of attack were added to one plot. Now, since there are 8 angles of attack, 9 rudder positions and 9 aileron positions, only a number of these conditions will be plotted in this section. Here, each of the rudder effectiveness plots will be for one angle of attack and will include all rudder and aileron deflections. These plots will only be given for the $0°$, $10°$, $20°$ and $30°$ angles of attack to limit the number of plots added.

4.5.1. Aileron Effect on Side-Force Rudder Control Derivative

Rudder side-force control derivatives under aileron deflections for four angles of attack are shown in Figures 4.23a through 4.24b. All four plots have the same scale on the y axis to aid visual interpretation. The thin solid lines are linearizations of the control derivatives at each aileron position. In Table 4.4, the linearized rudder control derivatives for various aileron positions are tabulated for the $10°$ AoA. Only the $10°$ values are included to keep the table of a reasonable size and this angle is close to the cruise AoA. The last column labelled '$\Delta(C_{Y_{\delta_\mathrm{R}}})_{\overline{\delta}_\mathrm{A}=0}$' is the percent change in slope of that specific control derivative with respect to that with null aileron deflection and partly answers the third research question. The maximum increase in the side-force rudder effectiveness due to aileron deflections is by only 2.3% at this angle of attack and is with the $\pm 25\%$ aileron deflection.

As with the rudder control derivatives for null aileron deflection in Section 4.3.1, the rudder effectiveness reduces with angle of attack. When looking at any of the four figures in this section, one can see an increment in side-force coefficient due to aileron deflections with 0% rudder deflection. Positive aileron deflections (roll left) cause a negative side-force on the dual-wing aircraft (leftward force), inducing a positive yawing moment (nose right). The yawing moment is covered in the next section. Previously, the side-force due to aileron deflection was mentioned as one of the sources of adverse yaw, next to

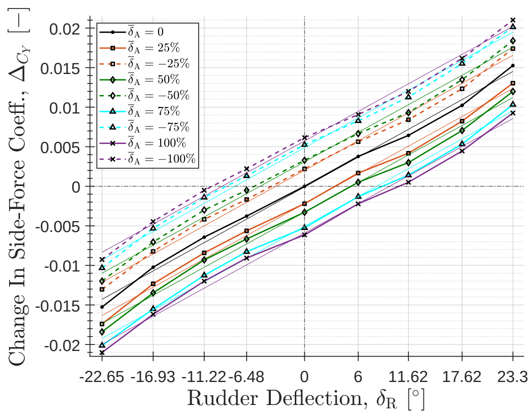

(a) Side-Force Rudder Control Derivative for Various Aileron Positions at $\alpha = 0°$. Dual-Wing Results.

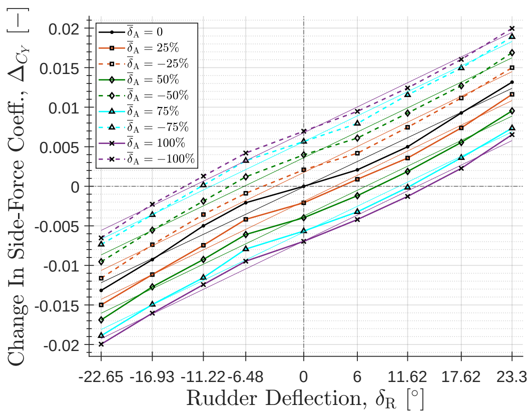

(b) Side-Force Rudder Control Derivative for Various Aileron Positions at $\alpha = 10°$. Dual-Wing Results.

Figure 4.23: Side-Force Rudder Control Derivatives for Various Aileron Positions at Two AoA's. Dual-Wing Results.

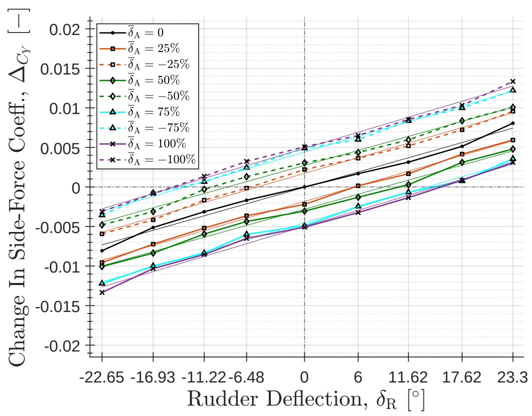

(a) Side-Force Rudder Control Derivative for Various Aileron Positions at $\alpha = 20°$. Dual-Wing Results.

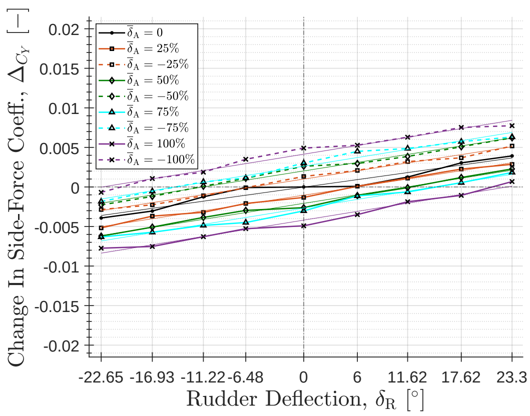

(b) Side-Force Rudder Control Derivative for Various Aileron Positions at $\alpha = 30°$. Dual-Wing Results.

Figure 4.24: Side-Force Rudder Control Derivatives for Various Aileron Positions at Two AoA's. Dual-Wing Results.

Table 4.4: Side-Force Rudder Control Derivative Linearization For Various Normalized Aileron Deflections. $\alpha = 10°$. The Last Column Indicates the Change in $C_{Y_{\delta_R}}$ for the Indicated Aileron Deflection With Respect to That With Zero Aileron Deflection, in Percent.

$\bar{\delta}_A$ [%]	$C_{Y_{\delta_R}}$ [deg^{-1}]	$C_Y(\delta_R = 0)$ [−]	R^2 [−]	$\Delta\left(C_{Y_{\delta_R}}\right)_{\bar{\delta}_A=0}$ [%]
-100	$5.45 \cdot 10^{-4}$	0.0068	0.9942	1.85
-75	$5.44 \cdot 10^{-4}$	0.0056	0.9939	1.68
-50	$5.42 \cdot 10^{-4}$	0.0036	0.9931	1.39
-25	$5.47 \cdot 10^{-4}$	0.0017	0.9933	2.27
0	$5.35 \cdot 10^{-4}$	$-7.49 \cdot 10^{-5}$	0.9873	0
25	$5.47 \cdot 10^{-4}$	-0.0019	0.9930	2.26
50	$5.42 \cdot 10^{-4}$	-0.0038	0.9933	1.40
75	$5.44 \cdot 10^{-4}$	-0.0058	0.9935	1.66
100	$5.45 \cdot 10^{-4}$	-0.0069	0.9944	1.86

the drag differential due to an aileron input. The implication of the aileron input induced side-force is that this aircraft will exhibit a coupling with the rolling and yawing motion of the aircraft. Thus, the flight control system could account for this by coupling rudder inputs to aileron inputs. For example, consider the $10°$ AoA case with $+50\%$ aileron deflection. If the rudder is at 0% deflection, there will be a negative side-force and thus a normalized rudder deflection of around $+25\%$ is needed to balance it.

Going from $0°$ to $10°$, one can see that the slope of the rudder control derivative lines decrease while the side-forces induced by the aileron controls with the rudder at null deflection slightly increase. Also, the curves become more non-linear. Going from $10°$ to $20°$, both the slopes of the rudder control derivative for all aileron positions and the induced side-forces for null rudder deflection decrease. Also, the control derivative curves for all aileron positions except for $\pm 100\%$ deflections are more linear at $20°$ AoA. Finally, going from $20°$ to $30°$ AoA, the slopes of the rudder control derivatives and the induced side-forces due to aileron inputs are reduced. At $30°$ the linearizations all have lower R^2 than at $20°$ suggesting less linearity. In conclusion, the aileron inputs mainly shift the rudder effectiveness curves up or down by around the amount of the aileron input induced side-force for zero rudder deflection. There is a small change in the rudder effectiveness with aileron input.

4.5.2. Aileron Effect on Yawing Moment Rudder Control Derivative

Rudder yawing moment control derivatives under aileron deflections for four angles of attack are shown in Figures 4.25a through 4.26b. Note that the y-axis scales are again the same in the four plots. Only one half of the control derivative plots will be given to zoom deeper into the plots. Note that the control derivative data are symmetric about the origin, which can be seen in the previous Figure 4.23a. For example, the side-force in the flight condition with $+25\%$ aileron deflection and $+50\%$ rudder deflection is equal in magnitude and of opposite sign with respect to that in the condition with -25% aileron deflection and -50% rudder deflection. This is also the case for the rolling moment and yawing moment. Note that the linearizations are slightly different for the corresponding $\pm\overline{\delta}_{\mathrm{A}}$ deflections. In Table 4.5, the linearized rudder control derivatives for various aileron positions are tabulated for the $10°$ AoA. The maximum change to the rudder yawing moment effectiveness due to aileron deflections is a reduction of about 1.3%, for the $\pm 100\%$ aileron conditions.

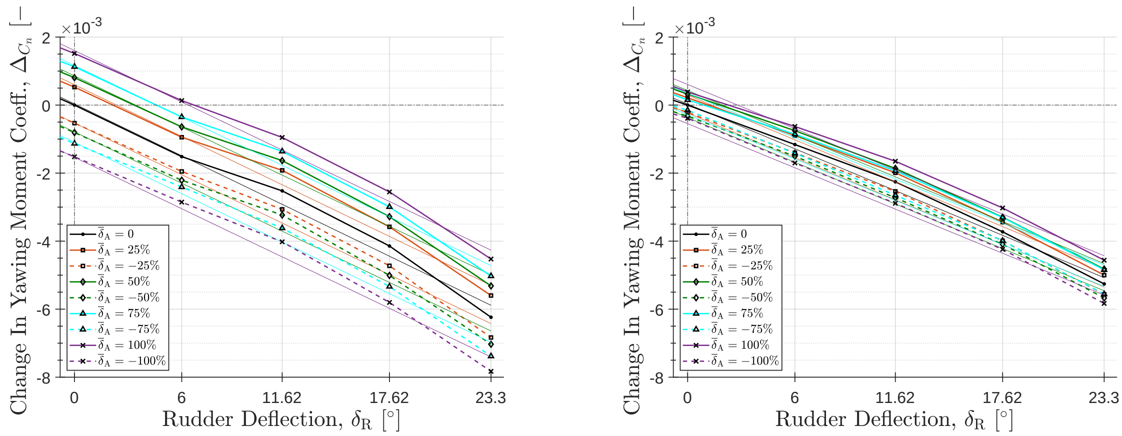

(a) Yawing Moment Rudder Control Derivative for Various Aileron Positions at $\alpha = 0°$. Dual-Wing Results.

(b) Yawing Moment Rudder Control Derivative for Various Aileron Positions at $\alpha = 10°$. Dual-Wing Results.

Figure 4.25: Yawing Moment Rudder Control Derivatives for Various Aileron Positions at Two AoA's. Dual-Wing Results.

Considering Figure 4.25a with the angle of attack equal to $0°$, one can see the increment in yawing moment coefficient due to aileron deflections with 0% rudder deflection. This is the yawing moment induced by the aileron deflection and it is the largest magnitude for the lowest AoA of $0°$. As previously mentioned, positive aileron deflections (roll left) cause a positive yawing moment coefficient (nose right) on the dual-wing aircraft at low angles of attack and this is known as adverse yaw. Recall that the adverse yaw is due to the side-force and drag imbalances on the left and right wings due to aileron inputs. The aileron induced yawing moment is small relative to the control power of the rudders. This is

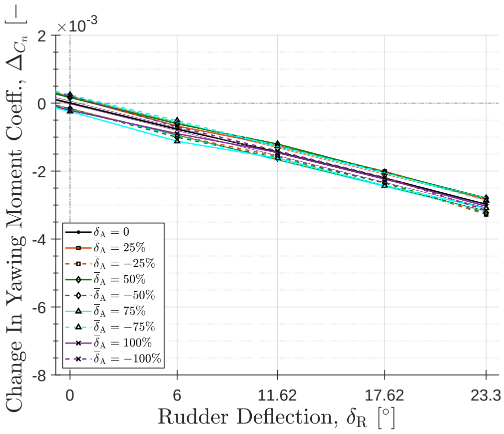

(a) Yawing Moment Rudder Control Derivative for Various Aileron Positions at $\alpha = 20°$. Dual-Wing Results.

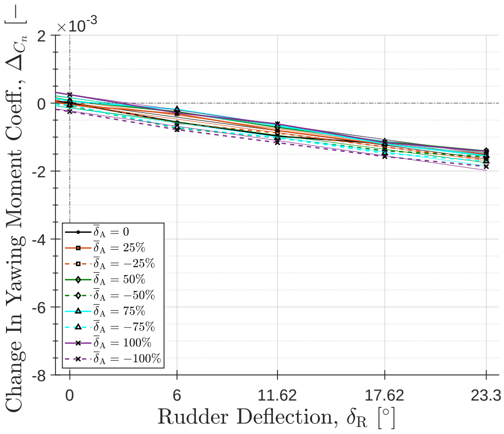

(b) Yawing Moment Rudder Control Derivative for Various Aileron Positions at $\alpha = 30°$. Dual-Wing Results.

Figure 4.26: Yawing Moment Rudder Control Derivatives for Various Aileron Positions at Two AoA's. Dual-Wing Results.

Table 4.5: Yawing Moment Rudder Control Derivative Linearization For Various Aileron Positions. $\alpha = 10°$. The Last Column Indicates the Change in $C_{n_{\delta_R}}$ for the Indicated Aileron Deflection With Respect to That With Zero Aileron Deflection, in Percent.

$\overline{\delta}_A$ [%]	$C_{n_{\delta_R}}$ [deg^{-1}]	$C_n(\delta_R = 0)$ [−]	R^2 [−]	$\Delta\left(C_{n_{\delta_R}}\right)_{\overline{\delta}_A=0}$ [%]
−100	$-2.16 \cdot 10^{-4}$	$-5.46 \cdot 10^{-4}$	0.9967	−1.28
−75	$-2.17 \cdot 10^{-4}$	$-2.84 \cdot 10^{-4}$	0.9968	−1.07
−50	$-2.19 \cdot 10^{-4}$	$-3.68 \cdot 10^{-4}$	0.9966	−0.25
−25	$-2.19 \cdot 10^{-4}$	$-2.34 \cdot 10^{-4}$	0.9963	0.18
0	$-2.19 \cdot 10^{-4}$	$3.07 \cdot 10^{-4}$	0.9965	0
25	$-2.19 \cdot 10^{-4}$	$2.95 \cdot 10^{-4}$	0.9961	0.16
50	$-2.18 \cdot 10^{-4}$	$4.29 \cdot 10^{-4}$	0.9963	−0.27
75	$-2.17 \cdot 10^{-4}$	$3.44 \cdot 10^{-4}$	0.9960	−1.11
100	$-2.16 \cdot 10^{-4}$	$6.06 \cdot 10^{-4}$	0.9958	−1.32

seen in Figure 4.25a, with the $+100\%$ aileron deflection condition only requiring around $+25\%$ rudder deflection to balance the adverse yaw.

As with the rudder control derivatives for null aileron deflection in Section 4.3.2, the rudder effectiveness reduces with increasing angle of attack. Going from $0°$ to $10°$, one can see that the slopes and distances between various δ_A curves have reduced. Thus, the rudder is losing effectiveness with AoA and the effect of the aileron deflection on the yawing moment is reducing (as shown in Figure 4.22b). As the angle of attack is further increased, these trends continue. Furthermore, the curves begin to cross at higher angles of attack. This is due to the balance of the side-forces (Figure 4.19b) and drag coefficients (Figure 4.18b) on the left and right wings with varying AoA and CS3 position.

4.5.3. Aileron Effect on Rolling Moment Rudder Control Derivative

Rudder rolling moment control derivatives under aileron deflections for four angles of attack are shown in Figures 4.27a through 4.28b. All four plots have the same scale on the y axis to aid visual interpretation. Here, one can see the effects of both the aileron deflection and the rudder deflection on the rolling moment. In Table 4.6, the linearized rudder control derivatives for various aileron positions are tabulated for the $10°$ AoA. The maximum change to the rudder rolling moment effectiveness due to aileron deflections is a reduction of about 4.8%, for the $\pm75\%$ aileron conditions.

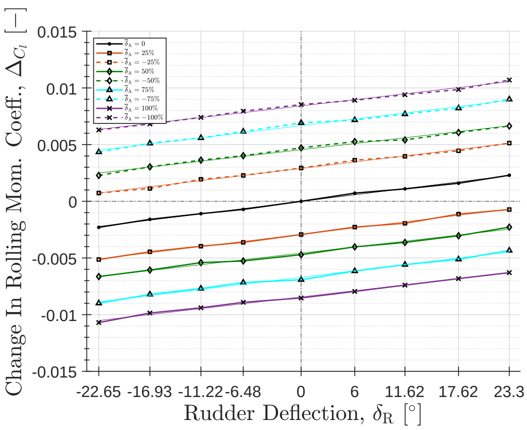

(a) Rolling Moment Rudder Control Derivative for Various Aileron Positions at $\alpha = 0°$. Dual-Wing Results.

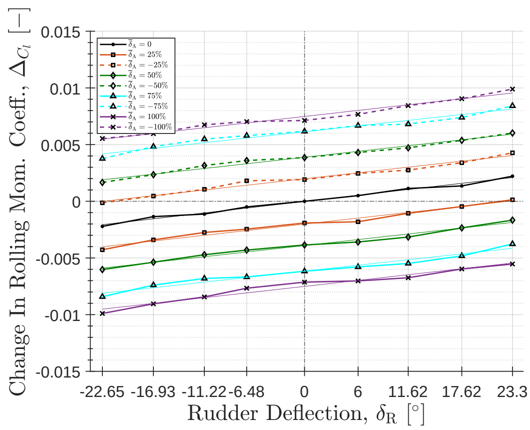

(b) Rolling Moment Rudder Control Derivative for Various Aileron Positions at $\alpha = 10°$. Dual-Wing Results.

Figure 4.27: Rolling Moment Rudder Control Derivatives for Various Aileron Positions at Two AoA's. Dual-Wing Results.

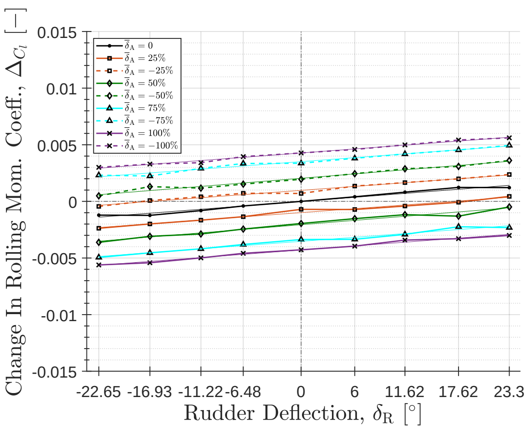

(a) Rolling Moment Rudder Control Derivative for Various Aileron Positions at $\alpha = 20°$. Dual-Wing Results.

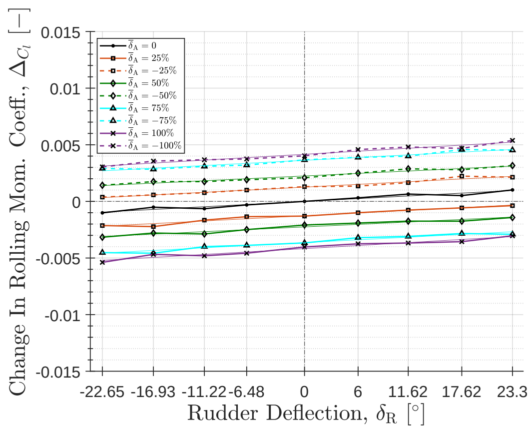

(b) Rolling Moment Rudder Control Derivative for Various Aileron Positions at $\alpha = 30°$. Dual-Wing Results.

Figure 4.28: Rolling Moment Rudder Control Derivatives for Various Aileron Positions at Two AoA's. Dual-Wing Results.

Table 4.6: Rolling Moment Rudder Control Derivative Linearization For Various Aileron Positions. $\alpha = 10°$. The Last Column Indicates the Change in $C_{l_{\delta_R}}$ for the Indicated Aileron Deflection With Respect to That With Zero Aileron Deflection, in Percent.

$\overline{\delta}_A$ [%]	$C_{l_{\delta_R}}$ [deg^{-1}]	$C_l(\delta_R = 0)$ [−]	R^2 [−]	$\Delta\left(C_{l_{\delta_R}}\right)_{\overline{\delta}_A=0}$ [%]
-100	$8.88 \cdot 10^{-5}$	0.0075	0.9720	-1.98
-75	$8.63 \cdot 10^{-5}$	0.0061	0.9615	-4.75
-50	$8.77 \cdot 10^{-5}$	0.0039	0.9833	-3.26
-25	$8.81 \cdot 10^{-5}$	0.0020	0.9795	-2.81
0	$9.06 \cdot 10^{-5}$	$-1.27 \cdot 10^{-5}$	0.9906	0
25	$8.82 \cdot 10^{-5}$	-0.0020	0.9818	-2.7
50	$8.77 \cdot 10^{-5}$	-0.0039	0.9847	-3.19
75	$8.64 \cdot 10^{-5}$	-0.0062	0.9639	-4.63
100	$8.86 \cdot 10^{-5}$	-0.0075	0.9663	-2.27

One can see that the aileron and rudder deflections are most effective at generating rolling moments at the lower angles of attack. For zero rudder deflection, positive aileron deflections have been found to cause negative rolling moments and negative aileron deflections cause positive rolling moments, as intended. Considering the $10°$ and $20°$ AoA's with -25% aileron deflection, the positive rolling moment reverses and becomes negative as the rudder deflection nears -100%. In these conditions, the rudder effect on the rolling moment is larger than that of the aileron. Due to symmetry about the origin, this is also the case for $+25\%$ aileron deflection as the rudder deflection nears $+100\%$. This is not the case at $30°$ because the rudders are less effective at changing the rolling moment (Figure 4.11b) and is not the case at $0°$ because the ailerons are more effective at changing the rolling moment (Figure 4.20b).

4.6. Airspeed Effect on Rudder Control Derivatives

In this section, the effect of changing the airspeed on the rudder control derivatives will be briefly mentioned. As in Sections 4.3 and 4.5, the results in this section are for the dual-wing Flying V. The tested airspeeds are 18 m/s, 20 m/s, 25 m/s and 28 m/s. The angles of attack considered in this section are from $0°$ to $15°$ because $15°$ is the maximum AoA for the highest tested airspeed of 28 m/s. The main wing control surfaces (CS1, CS2, CS3) are all at zero deflection. With changes to the airspeed, the Reynolds number and the dynamic pressure acting on the model will change. Reynolds number changes influence the boundary layer behavior and dynamic pressure changes (for a given AoA) will influence the model loading and elastic deflections.

4.6.1. Airspeed Effect on Side-Force Rudder Control Derivative

Rudder side-force control derivatives for various airspeeds and four angles of attack are shown in Figures 4.29a through 4.30b. These four plots have the same y-axis limits to show the changes in slope with angle of attack. The data are also summarized in Table 4.7, with the last column labelled '$\Delta(C_{Y_{\delta_R}})_{V_\infty=18}$ [%]' representing the percent change in slope of that specific control derivative with respect to that of 18 m/s and the same AoA. For $0°$ AoA, increasing the airspeed slightly increases the slope (effectiveness) of the side-force control derivative. At $0°$ AoA, going from 18 to 28 m/s increases the rudder effectiveness by around 8.4%. Similarly, this increase in effectiveness due to airspeed is around 9.6% for the $5°$ AoA.

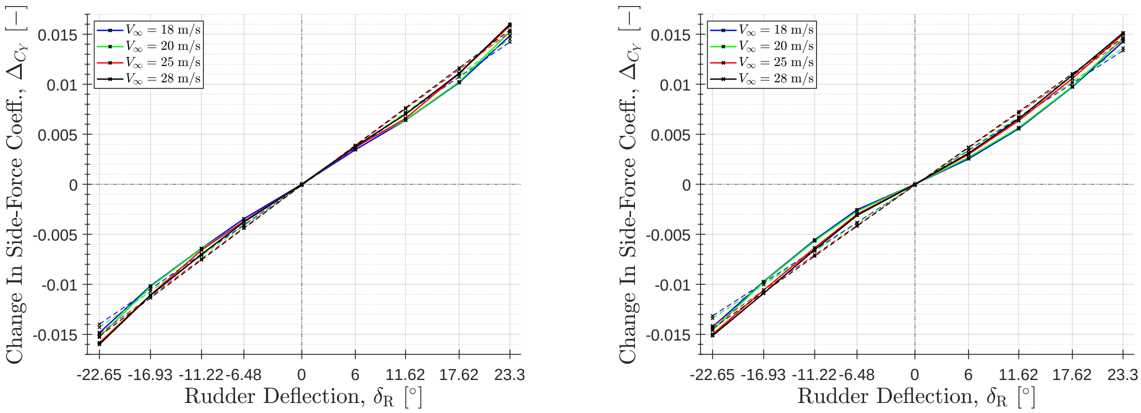

(a) Side-Force Rudder Control Derivative for Various Airspeeds at $\alpha = 0°$. Dual-Wing Results.

(b) Side-Force Rudder Control Derivative for Various Airspeeds at $\alpha = 5°$. Dual-Wing Results.

Figure 4.29: Side-Force Rudder Control Derivatives for Various Airspeeds at Two Angles of Attack. Dual-Wing Results.

Generally, as the Reynolds number increases, boundary layers thin and control surfaces become more effective. This is seen in the $0°$ and $5°$ AoA plots in this section. As the angle of attack is increased to $10°$, the rudder effectiveness at 25 m/s has become slightly stronger than that of the higher airspeed, 28 m/s. At the highest angle of $15°$, the airspeeds ordered from the lowest to highest slopes are 20, 25, 18 then 28 m/s as seen in Table 4.7. Changes to the Reynolds number change the vortical flow behavior and this could explain the changed order of the slopes of the control derivatives at the higher angles of attack. The maximum change to the rudder effectiveness in the airspeed range tested is around 11%.

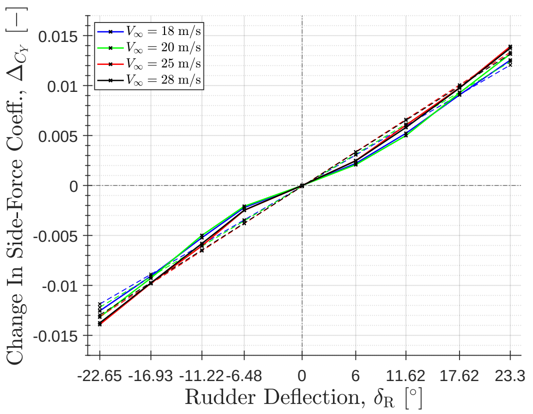

(a) Side-Force Rudder Control Derivative for Various Airspeeds at $\alpha = 10°$. Dual-Wing Results.

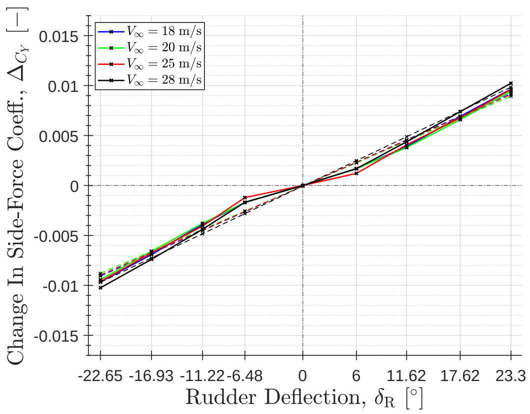

(b) Side-Force Rudder Control Derivative for Various Airspeeds at $\alpha = 15°$. Dual-Wing Results.

Figure 4.30: Side-Force Rudder Control Derivatives for Various Airspeeds at Two Angles of Attack. Dual-Wing Results.

Table 4.7: Side-Force Rudder Control Derivative Linearization For Various Airspeeds and Angles of Attack. The Last Column Indicates the Change in $C_{Y_{\delta_R}}$ for the Indicated Airspeed With Respect to That at 18 m·s^{-1}, in Percent.

α [°]	V_∞ [m·s^1]	$C_{Y_{\delta_R}}$ [deg^{-1}]	$C_Y(\delta_R = 0)$ [−]	R^2 [−]	$\Delta\left(C_{Y_{\delta_R}}\right)_{V_\infty=18}$ [%]
0	18	$6.14 \cdot 10^{-4}$	$-8.59 \cdot 10^{-5}$	0.9964	0
0	20	$6.27 \cdot 10^{-4}$	$-8.78 \cdot 10^{-5}$	0.9956	2.16
0	25	$6.56 \cdot 10^{-4}$	$-9.19 \cdot 10^{-5}$	0.9959	6.90
0	28	$6.66 \cdot 10^{-4}$	$-9.32 \cdot 10^{-5}$	0.9972	8.43
5	18	$5.77 \cdot 10^{-4}$	$-8.08 \cdot 10^{-5}$	0.9900	0
5	20	$5.88 \cdot 10^{-4}$	$-8.23 \cdot 10^{-5}$	0.9900	1.82
5	25	$6.21 \cdot 10^{-4}$	$-8.69 \cdot 10^{-5}$	0.9949	7.60
5	28	$6.33 \cdot 10^{-4}$	$-8.86 \cdot 10^{-5}$	0.9959	9.63
10	18	$5.21 \cdot 10^{-4}$	$-7.29 \cdot 10^{-5}$	0.9926	0
10	20	$5.35 \cdot 10^{-4}$	$-7.49 \cdot 10^{-5}$	0.9873	2.76
10	25	$5.76 \cdot 10^{-4}$	$-8.06 \cdot 10^{-5}$	0.9937	10.63
10	28	$5.69 \cdot 10^{-4}$	$-7.96 \cdot 10^{-5}$	0.9932	9.24
15	18	$3.98 \cdot 10^{-4}$	$-5.57 \cdot 10^{-5}$	0.9915	0
15	20	$3.86 \cdot 10^{-4}$	$-5.40 \cdot 10^{-5}$	0.9918	−2.97
15	25	$3.93 \cdot 10^{-4}$	$-5.50 \cdot 10^{-5}$	0.9866	−1.18
15	28	$4.25 \cdot 10^{-4}$	$-5.95 \cdot 10^{-5}$	0.9921	6.86

4.6.2. Airspeed Effect on Yawing Moment Rudder Control Derivative

Rudder yawing moment control derivatives for various airspeeds and four angles of attack are shown in Figures 4.31a through 4.32b. Again, the y-axis limits are the same in the four plots and like Section 4.5.2, only half of the plots are shown to zoom in. The data are also summarized in Table 4.8, with the last column labelled '$\Delta(C_{n_{\delta_R}})_{V_\infty=18}$' representing the percent change in slope of that specific control derivative with respect to that of 18 m/s and the same AoA. For 0° and 5° AoA, increasing the airspeed again slightly increases the slope (effectiveness) of the yawing moment control derivative by a maximum of around 12% going from 18 to 28 m/s. This agrees with the effect of increasing the Reynolds number mentioned in the last section.

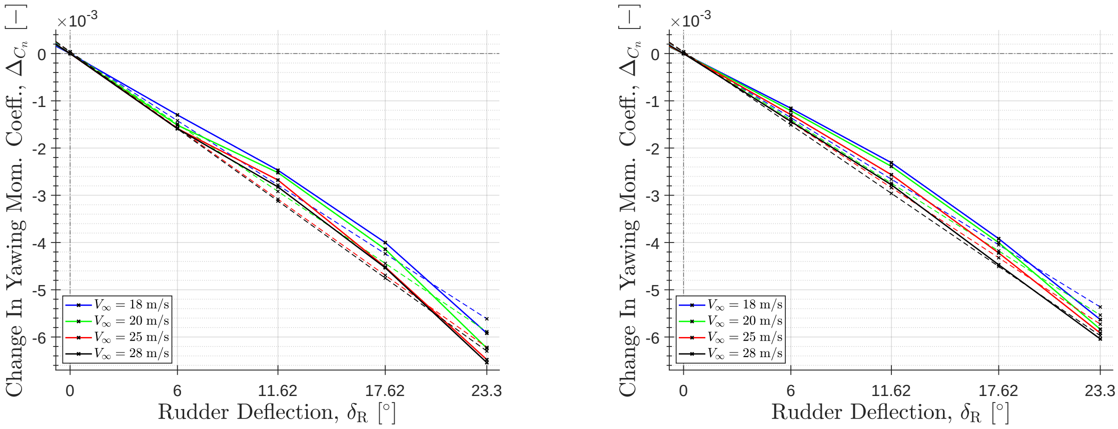

(a) Yawing Moment Rudder Control Derivative for Various Airspeeds at $\alpha = 0°$. Dual-Wing Results.

(b) Yawing Moment Rudder Control Derivative for Various Airspeeds at $\alpha = 5°$. Dual-Wing Results.

Figure 4.31: Yawing Moment Rudder Control Derivatives for Various Airspeeds at Two AoA's. Dual-Wing Results.

At $10°$ AoA, the slope of the 25 m/s curve has again become slightly larger than that of the higher airspeed, 28 m/s. At the highest angle of attack of $15°$, the airspeeds ordered from the lowest to highest slopes are 20, 25, 18 then 28 m/s, just like the side-force control derivative in the previous section.

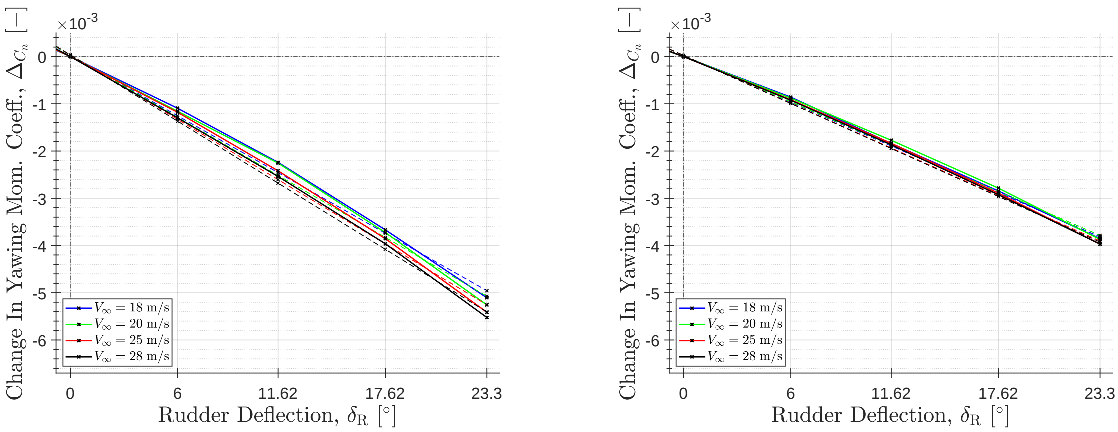

(a) Yawing Moment Rudder Control Derivative for Various Airspeeds at $\alpha = 10°$. Dual-Wing Results.

(b) Yawing Moment Rudder Control Derivative for Various Airspeeds at $\alpha = 15°$. Dual-Wing Results.

Figure 4.32: Yawing Moment Rudder Control Derivatives for Various Airspeeds at Two AoA's. Dual-Wing Results.

4.6.3. Airspeed Effect on Rolling Moment Control Derivative

Rudder rolling moment control derivatives for various airspeeds and four angles of attack are shown in Figures 4.33a through 4.34b. Again, the y-axis limits are the same in the four plots. The data are also summarized in Table 4.9, with the last column labelled '$\Delta(C_{Y_{\delta_R}})_{V_\infty=18}$' representing the percent change in slope of that specific control derivative with respect to that of 18 m/s and the same AoA. At $0°$ AoA, the rolling moment increment for a given rudder deflection slightly increases with airspeed, as seen in the last column of Table 4.9. This agrees with the effect of increasing the Reynolds number mentioned in Section 4.6.1.

Table 4.8: Yawing Moment Rudder Control Derivative Linearization For Various Airspeeds and Angles of Attack. The Last Column Indicates the Change in $C_{n_{\delta_R}}$ for the Indicated Airspeed With Respect to That at 18 m·s^{-1}, in Percent.

α [°]	V_∞ [m·s^1]	$C_{Y_{\delta_R}}$ [deg^{-1}]	$C_Y(\delta_R = 0)$ $[-]$	R^2 $[-]$	$\Delta\left(C_{Y_{\delta_R}}\right)_{V_\infty=18}$ [%]
0	18	$-2.42 \cdot 10^{-4}$	$3.39 \cdot 10^{-5}$	0.9948	0
0	20	$-2.54 \cdot 10^{-4}$	$3.56 \cdot 10^{-5}$	0.9940	4.83
0	25	$-2.69 \cdot 10^{-4}$	$3.76 \cdot 10^{-5}$	0.9960	10.76
0	28	$-2.72 \cdot 10^{-4}$	$3.81 \cdot 10^{-5}$	0.9970	12.16
5	18	$-2.32 \cdot 10^{-4}$	$3.24 \cdot 10^{-5}$	0.9942	0
5	20	$-2.39 \cdot 10^{-4}$	$3.35 \cdot 10^{-5}$	0.9940	3.19
5	25	$-2.47 \cdot 10^{-4}$	$3.46 \cdot 10^{-5}$	0.9967	6.76
5	28	$-2.58 \cdot 10^{-4}$	$3.61 \cdot 10^{-5}$	0.9987	11.30
10	18	$-2.14 \cdot 10^{-4}$	$3.00 \cdot 10^{-5}$	0.9968	0
10	20	$-2.19 \cdot 10^{-4}$	$3.07 \cdot 10^{-5}$	0.9965	2.36
10	25	$-2.27 \cdot 10^{-4}$	$3.18 \cdot 10^{-5}$	0.9972	6.03
10	28	$-2.33 \cdot 10^{-4}$	$3.27 \cdot 10^{-5}$	0.9984	9.08
15	18	$-1.65 \cdot 10^{-4}$	$2.31 \cdot 10^{-5}$	0.9985	0
15	20	$-1.63 \cdot 10^{-4}$	$2.29 \cdot 10^{-5}$	0.9981	-0.85
15	25	$-1.69 \cdot 10^{-4}$	$2.36 \cdot 10^{-5}$	0.9985	2.24
15	28	$-1.70 \cdot 10^{-4}$	$2.37 \cdot 10^{-5}$	0.9988	2.84

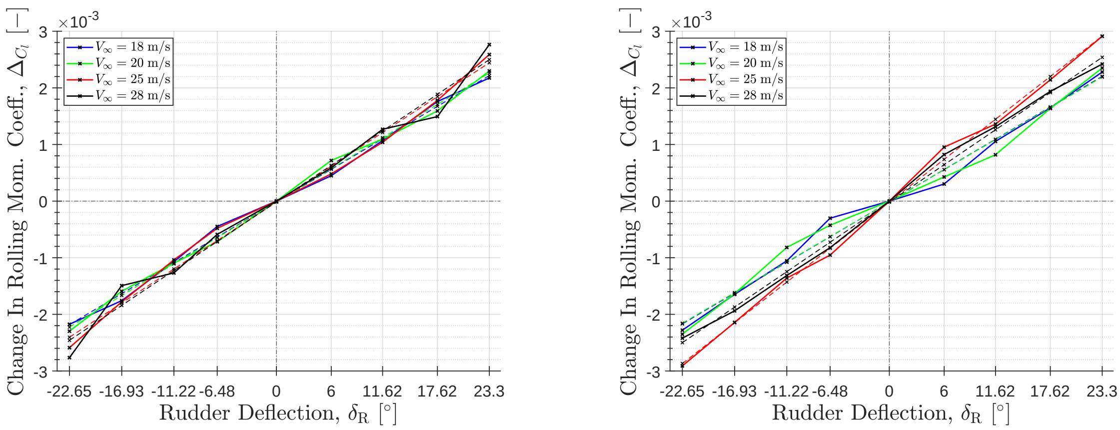

(a) Rolling Moment Rudder Control Derivative for Various Airspeeds at $\alpha = 0°$. Dual-Wing Results.

(b) Rolling Moment Rudder Control Derivative for Various Airspeeds at $\alpha = 5°$. Dual-Wing Results.

Figure 4.33: Rolling Moment Rudder Control Derivatives for Various Airspeeds at Two AoA's. Dual-Wing Results.

At 5° AoA, the slope of the control derivative at the tunnel speed of 25 m/s has increased since the last angle of attack and eclipsed that of the higher speed. At 5° AoA, the rudder effectiveness increases an astounding 32% by increasing the airspeed from 18 to 25 m/s. Also, the rolling moment control derivative for the 28 m/s curve increases in slope going from 0° to 5° AoA. For the other airspeeds and angles of attack, the slopes of the control derivatives reduce with AoA.

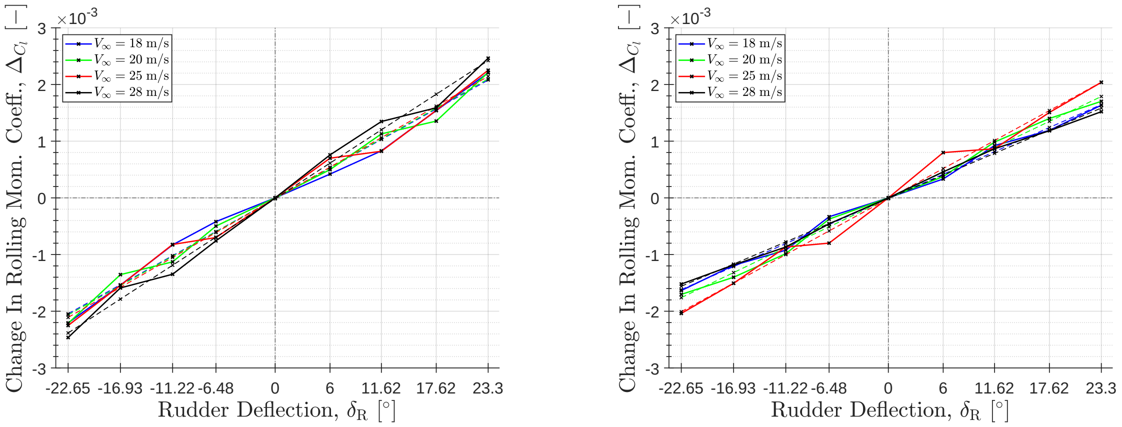

(a) Rolling Moment Rudder Control Derivative for Various Airspeeds at $\alpha = 10°$. Dual-Wing Results.

(b) Rolling Moment Rudder Control Derivative for Various Airspeeds at $\alpha = 15°$. Dual-Wing Results.

Figure 4.34: Rolling Moment Rudder Control Derivatives for Various Airspeeds at Two AoA's. Dual-Wing Results.

Table 4.9: Rolling Moment Rudder Control Derivative Linearization For Various Airspeeds and Angles of Attack. The Last Column Indicates the Change in $C_{l_{\delta_\mathrm{R}}}$ for the Indicated Airspeed With Respect to That at 18 m·s^{-1}, in Percent.

α [°]	V_∞ [m·s^1]	$C_{Y_{\delta_\mathrm{R}}}$ [deg^{-1}]	$C_Y(\delta_\mathrm{R}=0)$ [−]	R^2 [−]	$\Delta\left(C_{Y_{\delta_\mathrm{R}}}\right)_{V_\infty=18}$ [%]
0	18	$9.58 \cdot 10^{-5}$	$-1.34 \cdot 10^{-5}$	0.9960	0
0	20	$9.77 \cdot 10^{-5}$	$-1.37 \cdot 10^{-5}$	0.9972	2.0
0	25	$1.06 \cdot 10^{-4}$	$-1.48 \cdot 10^{-5}$	0.9919	10.18
0	28	$1.08 \cdot 10^{-4}$	$-1.51 \cdot 10^{-5}$	0.9805	12.68
5	18	$9.51 \cdot 10^{-5}$	$-1.33 \cdot 10^{-5}$	0.9894	0
5	20	$9.47 \cdot 10^{-5}$	$-1.33 \cdot 10^{-5}$	0.9857	-0.53
5	25	$1.26 \cdot 10^{-4}$	$-1.76 \cdot 10^{-5}$	0.9975	32.27
5	28	$1.10 \cdot 10^{-4}$	$-1.54 \cdot 10^{-5}$	0.9969	15.26
10	18	$8.97 \cdot 10^{-5}$	$-1.26 \cdot 10^{-5}$	0.9900	0
10	20	$9.06 \cdot 10^{-5}$	$-1.27 \cdot 10^{-5}$	0.9906	0.99
10	25	$9.25 \cdot 10^{-5}$	$-1.30 \cdot 10^{-5}$	0.9895	3.10
10	28	$1.05 \cdot 10^{-4}$	$-1.46 \cdot 10^{-5}$	0.9920	16.54
15	18	$7.10 \cdot 10^{-5}$	$-9.94 \cdot 10^{-6}$	0.9946	0
15	20	$7.72 \cdot 10^{-5}$	$-1.08 \cdot 10^{-5}$	0.9945	8.73
15	25	$8.81 \cdot 10^{-5}$	$-1.23 \cdot 10^{-5}$	0.9893	24.05
15	28	$6.84 \cdot 10^{-5}$	$-9.58 \cdot 10^{-6}$	0.9974	-3.67

5 Conclusions

Winglet integration effects on the Flying V aircraft were identified with a 4.6% scale, half-wing wind tunnel model. Also, the effects of deflecting the rudder and the outboard control surface (CS3) on the aerodynamic coefficients have been found. Furthermore, the effects of deflecting the ailerons and changing the airspeed on the rudder effectiveness have been analyzed in this report.

Without control surface deflections, the winglet integration has been found to slightly increase the lift coefficient by a maximum of about 0.0035 for angles of attack below $10°$ and slightly decrease the lift coefficient by a maximum of about 0.016 for higher angles. The winglet has been found to increase the drag of the model by a maximum of about 0.004 until around $28°$ angle of attack. The winglet has reduced the maximum untrimmed lift-to-drag ratio from around 14.4 to 12.3 at $10°$ angle of attack. The winglet increases the pitching moment acting on the model for most of the tested angles of attack. Considering only the left wing of the model, for angles of attack below $5°$ and above $25°$, the winglet has reduced the side-force acting on the left wing and increased the side-force for angles of attack between these. The results imply that the local flow near the winglet is closely aligned with the winglet chord near $5°$ angle of attack. Below $2.5°$ and above $20°$ angle of attack, the winglet has been found to increase the yawing moment of the left wing while decreasing it between $2.5°$ and $15°$.

Almost all of the rudder deflections have been found to reduce the lift coefficient at all angles of attack, by a maximum of around 0.0024 when considering the left wing. There are only a few conditions in which deflecting the rudder marginally increases the lift. Rudder deflections have been found to increase the drag coefficient at all positive angles of attack, by a maximum of around 0.0024 when considering the left wing. Positive and negative rudder deflections oppositely affect the side-force of the left wing until higher angles of attack. Beyond about $25°$ angle of attack, the smaller three of the four negative rudder deflections have the opposite effect on the half-wing side-force coefficient than desired. The Flying V does not encounter a control reversal condition here because the other wing still generates larger magnitude increments in side-force in the intended direction at these angles of attack. The maximum change in side-force coefficient due to one wing's rudder deflection is around 0.008.

Positive and negative rudder deflections also oppositely affect the rolling moment of the left wing until higher angles of attack. For almost all rudder deflections and angles of attack, both rudder deflection directions increase the pitching moment coefficient. Negative rudder deflections provide larger increases in pitching moment than positive ones. The maximum increase in the aircraft pitching moment due to one rudder is around 0.0035. Finally, positive and negative rudder deflections oppositely affect the yawing moment of the left wing for all angles of attack, as expected. The maximum change to the yawing moment due to one wing's rudder deflection is around 0.004 and positive rudder deflections cause a larger change in yawing moment than negative ones.

With the wing control surfaces at null deflection, the side-force, yawing moment and rolling moment rudder control derivatives have been extracted from the data and linearized. Increases to the angle of attack have been found to significantly reduce the slopes of these control derivatives (effectiveness) in a non-linear fashion. Going from $0°$ to $20°$ AoA, yields 49%, 50% and 37% reductions in the side-force, yawing moment and rolling moment rudder control derivatives, respectively.

Positive CS3 deflections have been found to increase the lift coefficient and negative deflections reduce the lift in all but three CS3 and angle of attack conditions. The largest magnitude change to the lift coefficient due to one wings CS3 deflection is a reduction of around 0.011. For positive angles of attack, positive CS3 deflections always increase the drag coefficient while negative CS3 deflections have been found to reduce the drag of the model for angles of attack above $10°$. This drag imbalance causes an adverse yawing moment on the dual-wing model when the ailerons are deflected. Opposite CS3 deflections have an opposite effect on the half-wing pitching moment coefficient, as intended. One wing's CS3 deflection has been found to increase the pitching moment by a maximum of around 0.016 at $5°$ AoA.

Dual-wing aileron deflections have been found to shift the curves of rudder control derivatives up or down, depending on the sign of the aileron input. The slopes of the control derivatives are largely unaffected by aileron deflections, only decreasing by a maximum of 4.8% with respect to the undeflected case at $10°$ AoA. Increasing the airspeed has been found to moderately increase the rudder effectiveness at low angles of attack. The maximum changes in side-force, yawing moment and rolling moment rudder control derivatives due to airspeed are around 11%, 12% and 32%, respectively.

5.1. Recommendations

This research shows that the aircraft has sufficient lateral and directional control while at $0°$ sideslip angle. Since the scaled flight test model will encounter non-zero sideslip conditions during flight, it is recommended to computationally (or experimentally) model the Flying V in these conditions to investigate flight dynamics and stability and control properties. If the Flying V is also modelled at different roll angles, there would, in principle, be enough data for the construction of a 6 degree of freedom flight dynamics model which could be used for pilot training and additional research. It is also recommended to consider correlating the SFTM free flight results with that of the various models. Another potential research topic is an investigation of the aerodynamic effects of deploying the landing gear.

References

[1] Benad, J., “Design of a commercial aircraft for high-subsonic speed as a flying wing configuration,” Technical report, Airbus, Berlin, 2015.

[2] Faggiano, F., “Aerodynamic Design Optimization of a Flying V Aircraft,” Msc. thesis, Delft University Of Technology, 2016.

[3] Jacobs, P. F., Flechner, S. G., and Montoya, L. C., “Effect of Winglets on a First-Generation Jet Transport Wing. 1: Longitudinal Aerodynamic Characteristics of a Semispan Model at Subsonic Speeds,” 1977.

[4] Flechner, S. G., Jacobs, P. F., and Whitcomb, R. T., “A High Subsonic Speed Wind-Tunnel Investigation of Winglets on a Representative Second-Generation Jet Transport Wing,” 1976.

[5] Alons, H., “OJF External Balance Documentation,” Nationaal Lucht- en Ruimtevaartlaboratorium, 2008.

[6] Martinez-Val, R., “Flying Wings. A New Paradigm for Civil Aviation?” *Acta Polytechnica*, Vol. 47, No. 1, 2007.

[7] Qin, N., Vavalle, A., Le Moigne, A., Laban, M., Hackett, K., and Weinerfelt, P., “Aerodynamic Studies for Blended Wing Body Aircraft,” *9th AIAA/ISSMO Symposium on Multidisciplinary Analysis and Optimization*, 2002, pp. 1–11.

[8] Torenbeek, E., “BLENDED WING BODY AND ALL-WING AIRLINERS,” *8th European Workshop on Aircraft Design Education*, 2007, pp. 1–9.

[9] Faggiano, F., Vos, R., Baan, M., and Van Dijk, R., “Aerodynamic Design of a Flying V Aircraft,” *17th AIAA Aviation Technology, Integration, and Operations Conference*, 2017, pp. 3589.

[10] Rubio Pascual, B., “Engine-Airframe Integration for the Flying V,” Msc. thesis, Delft University of Technology, 2018.

[11] Palermo, M., “The Longitudinal Static Stability and Control Characteristics of a Flying V Scaled Model,” Msc. thesis, Delft University of Technology, 2019.

[12] Viet, R., “Analysis of the flight characteristics of a highly swept cranked flying wing by means of an experimental test,” Msc. thesis, Delft University of Technology, 2019.

[13] Ruiz Garcia, A., “Aerodynamic Model Identification Of The Flying V using Wind Tunnel Data,” Msc. thesis, Delft University of Technology, 2019.

[14] van Empelen, S., “Engine Integration of the Flying V: Quantification of Engine Integration Effects Using Wind Tunnel Experiments,” Msc. thesis, Delft University of Technology, 2020.

[15] McCormick, B. W., *Aerodynamics, Aeronautics and Flight Mechanics*, John Wiley & Sons, 2nd ed., 1995.

[16] Whitcomb, R. T., “A Design Approach and Selected Wind Tunnel Results at High Subsonic Speeds for Wing-Tip Mounted Winglets,” 1976.

[17] Nangia, R. K., Palmer, M. E., and Doe, R. H., “Aerodynamic Design Studies of Conventional & Unconventional Wings With Winglets,” *24th Applied Aerodynamics Conference*, 2006.

[18] Jacobs, P. F. and Flechner, S. G., “The Effect of Winglets on the Static Aerodynamic Stability Characteristics of a Representative Second Generation Jet Transport Model,” 1976.

[19] Montoya, L. C., Jacobs, P. F., and Flechner, S. G., "Effect of Winglets on a First-Generation Jet Transport Wing. 3: Pressure and Spanwise Load Distributions for a Semispan Model at Mach 0.30," 1977.

[20] Montoya, L. C., Flechner, S. G., and Jacobs, P. F., "Effect of Winglets on a First-Generation Jet Transport Wing. 2: Pressure and Spanwise Load Distributions for a Semispan Model at High Subsonic Speeds." 1977.

[21] Jacobs, P. F., "Effect of Winglets on a First-Generation Jet Transport Wing. 5: Stability Characteristics of a Full-Span Wing With a Generalized Fuselage at High Subsonic Speeds," 1978.

[22] Montoya, L. C., Flechner, S. G., and Jacobs, P. F., "Effect of an Alternate Winglet on the Pressure and Spanwise Load Distributions of a First-Generation Jet Transport Wing," 1978.

[23] Meyer Jr, R. R., "Effect of Winglets on a First-Generation Jet Transport Wing. 4: Stability Characteristics for a Full-Span Model at Mach 0.30," 1978.

[24] Takenaka, K., Hatanaka, K., Yamazaki, W., and Nakahashi, K., "Multidisciplinary Design Exploration for a Winglet," *Journal of Aircraft*, Vol. 45, No. 5, 2008.

[25] de Mattos, B. S., Macedo, A. P., and da Silva Filho, D. H., "Considerations about Winglet Design," *21st AIAA Applied Aerodynamics Conference*, 2003.

[26] Weierman, J. and Jacob, J. D., "Winglet Design and Optimization for UAVs," *28th AIAA Applied Aerodynamics Conference*, 2010.

[27] Heyson, H. H., Riebe, G. D., and Fulton, C. L., "Theoretical Parametric Study of the Relative Advantages of Winglets and Wing-Tip Extensions," 1977.

[28] Mulder, J., van Staveren, W., van der Vaart, J., de Weerdt, E., de Visser, C., in't Veld, A., and Mooij, E., "Lecture Notes AE3202: Flight Dynamics," 2013.

[29] Dekking, F., Kraaikamp, C., Lopuhaä, H., and Meester, L., *A Modern Introduction to Probability and Statistics*, Springer, Delft, 2005.

[30] van Uitert, J., "Experimental Investigation of The Effect of Aerodynamic Add-ons on the Pitching Moment Behavior of the Flying V [Working Title]," Msc. thesis (not yet published), Delft University of Technology.

[31] Potsdam, M., Page, M., and Liebeck, R., "Blended Wing Body Analysis and Design," *15th Applied Aerodynamics Conference*, AIAA, 1997.

[32] Cerón-Muñoz, H. D., Diaz-Izquierdo, D. O., Bravo-Mosquera, P. D., Catalano, F. M., and De Santana, L. D., "Experimental Analyses of Droop, Wingtips and Fences on a BWB Model," *30th Congress of the International Council of the Aeronautical Sciences*, 2016, pp. 1–7.

A

Additional Plots

In this Appendix, additional plots are given which have been briefly mentioned in the main matter of this report.

A.1. Gap Effects

In this section, the plots of the gap effects to be used in correcting the results obtained with the open holes are given. The gap effects for the lift, drag, side-force, rolling moment, pitching moment and yawing moment are given in Figures A.1a through A.3b, respectively. The gap effect is derived from and applied to half-wing results and is explained in Section 3.1 of this report.

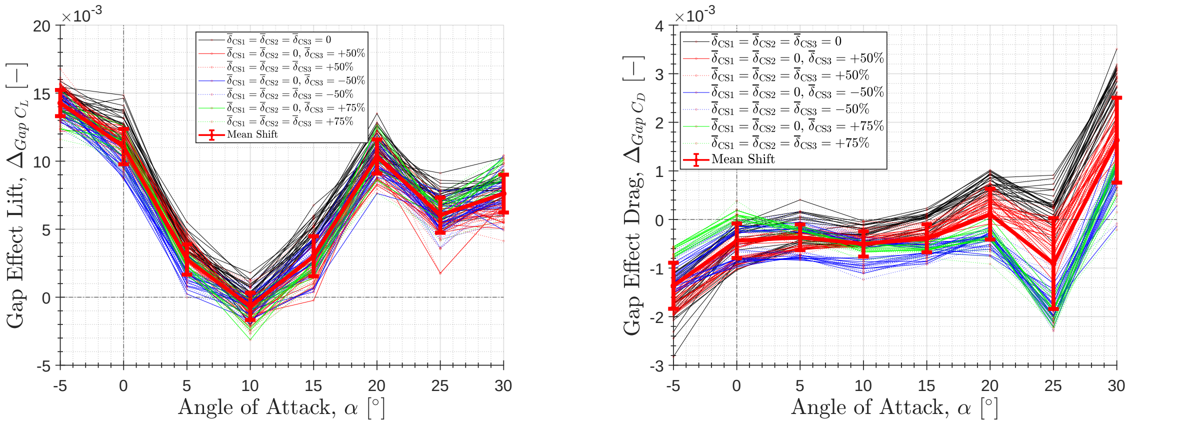

(a) Gap Effect on Lift Coefficient. Error Bars are One Standard Deviation From the Means.

(b) Gap Effect on Drag Coefficient. Error Bars are One Standard Deviation From the Means.

Figure A.1: Lift and Drag Gap Effects

A.2. Open, Corrected and Closed Results

In this section, the the plots showing the results before and after correcting the results for the gaps are plotted. The results before correcting are referred to as 'open' results and those after correcting are referred to as 'corrected'. Finally, 'closed' results are also given, and these are the results after the gaps have been closed. The correction is accurate when the 'corrected' results are close to the 'closed' results. These plots are presented for three cases; $\overline{\delta}_{\mathrm{CS1}}$ = $\overline{\delta}_{\mathrm{CS2}}$ = $\overline{\delta}_{\mathrm{CS3}}$ = 0%, $\overline{\delta}_{\mathrm{CS1}}$ = $\overline{\delta}_{\mathrm{CS2}}$ = $\overline{\delta}_{\mathrm{CS3}}$ = $+50\%$ and $\overline{\delta}_{\mathrm{CS1}}$ = $\overline{\delta}_{\mathrm{CS2}}$ = $\overline{\delta}_{\mathrm{CS3}}$ = -50%. In all cases, the rudder deflection is 0 and 95% confidence intervals calculated using the t-distribution are given. Note that the 'closed' results have a larger confidence interval than the 'corrected' results in some cases due to the lower sample size ($N = 2$) for the closed runs. This is only the case for the $\overline{\delta}_{\mathrm{CS1}}$ = $\overline{\delta}_{\mathrm{CS2}}$ = $\overline{\delta}_{\mathrm{CS3}}$ = $+50\%$ and $\overline{\delta}_{\mathrm{CS1}}$ = $\overline{\delta}_{\mathrm{CS2}}$ = $\overline{\delta}_{\mathrm{CS3}}$ = -50% configurations. The gaps are explained in Section 3.1 of this report.

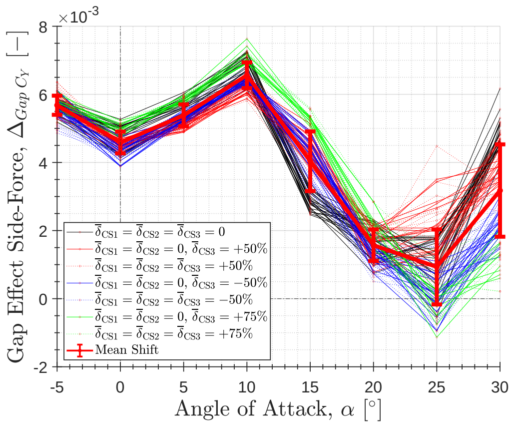

(a) Gap Effect on Side-Force Coefficient. Error Bars are One Standard Deviation From the Means.

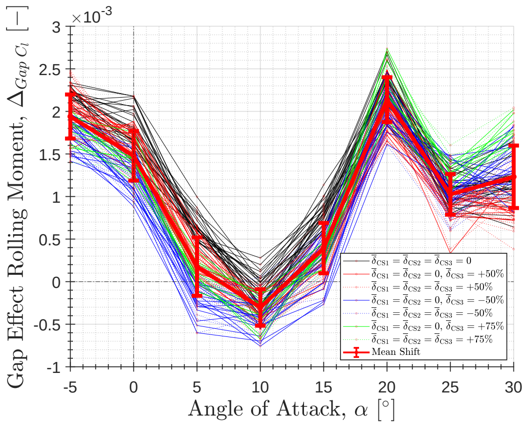

(b) Gap Effect on Rolling Moment Coefficient. Error Bars are One Standard Deviation From the Means.

Figure A.2: Side-Force and Rolling Moment Gap Effects

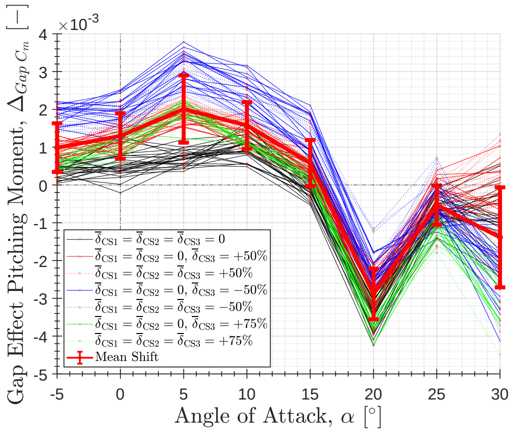

(a) Gap Effect on Pitching Moment Coefficient. Error Bars are One Standard Deviation From the Means.

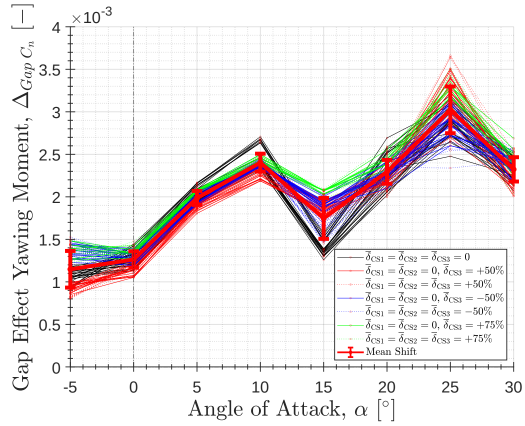

(b) Gap Effect on Yawing Moment Coefficient. Error Bars are One Standard Deviation From the Means.

Figure A.3: Pitching and Yawing Moment Gap Effects

The uncorrected ('open'), corrected and actual ('closed') results for the case with $\bar{\delta}_{\mathrm{CS1}}$ = $\bar{\delta}_{\mathrm{CS2}}$ = $\bar{\delta}_{\mathrm{CS3}}$ = 0% are shown in Figures A.4a through A.6b. Those for the case with $\bar{\delta}_{\mathrm{CS1}}$ = $\bar{\delta}_{\mathrm{CS2}}$ = $\bar{\delta}_{\mathrm{CS3}}$ = $+50$ are shown in Figures A.7a through A.9b and finally, those for the case with $\bar{\delta}_{\mathrm{CS1}}$ = $\bar{\delta}_{\mathrm{CS2}}$ = $\bar{\delta}_{\mathrm{CS3}}$ = -50 are shown in Figures A.10a through A.12b. Note that the means and confidence intervals for the asymmetric forces/moments (C_Y, C_l, C_n) are plotted for only the left wing for the reasons explained in Section 2.3.1.

A.3. Pitching Moment Coefficient (FWD CG Position)

in Figure A.13a, the pitching moment coefficient for the Flying V wind tunnel model is shown, using a CG/reference position 1.33 m aft of the nose. Note that the main matter of the report uses a reference position of $x_{MR} = 1.36$ m. Moving the CG forward yields pitching moment equilibrium ($C_m = 0$) around $10°$ AoA without the use of CS1, CS2 or CS3 for trimming.

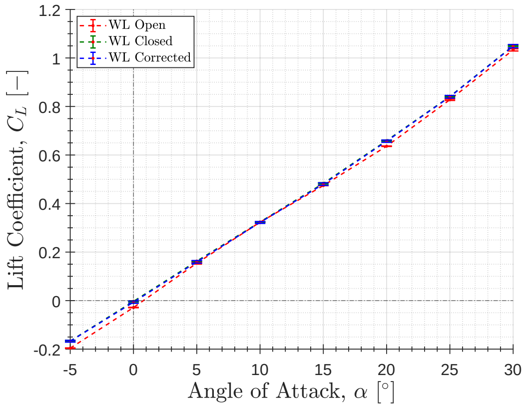

(a) Open, Corrected and Closed Lift Coefficient with 95% Confidence Intervals. Dual-Wing Results. $\overline{\delta}_{\mathrm{CS1}} = \overline{\delta}_{\mathrm{CS2}} = \overline{\delta}_{\mathrm{CS3}} = 0\%$, $\overline{\delta}_{\mathrm{R}} = 0\%$.

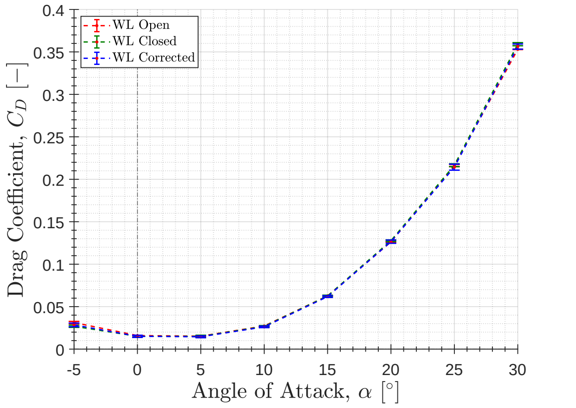

(b) Open, Corrected and Closed Drag Coefficient with 95% Confidence Intervals. Dual-Wing Results. $\overline{\delta}_{\mathrm{CS1}} = \overline{\delta}_{\mathrm{CS2}} = \overline{\delta}_{\mathrm{CS3}} = 0\%$, $\overline{\delta}_{\mathrm{R}} = 0\%$.

Figure A.4: Lift and Drag Coefficients Before and After Correcting. $\overline{\delta}_{\mathrm{CS1}} = \overline{\delta}_{\mathrm{CS2}} = \overline{\delta}_{\mathrm{CS3}} = 0\%$, $\overline{\delta}_{\mathrm{R}} = 0\%$.

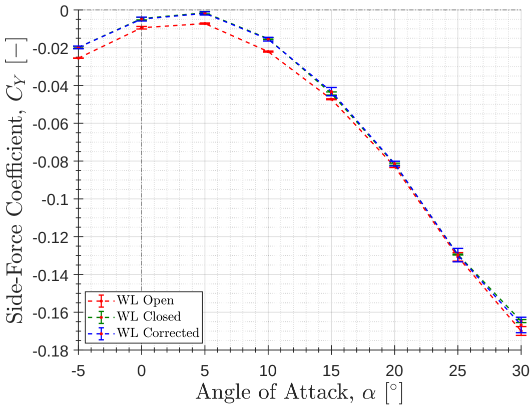

(a) Open, Corrected and Closed Side-Force Coefficient with 95% Confidence Intervals. Left Wing Only Results. $\overline{\delta}_{\mathrm{CS1}} = \overline{\delta}_{\mathrm{CS2}} = \overline{\delta}_{\mathrm{CS3}} = 0\%$, $\overline{\delta}_{\mathrm{R}} = 0\%$.

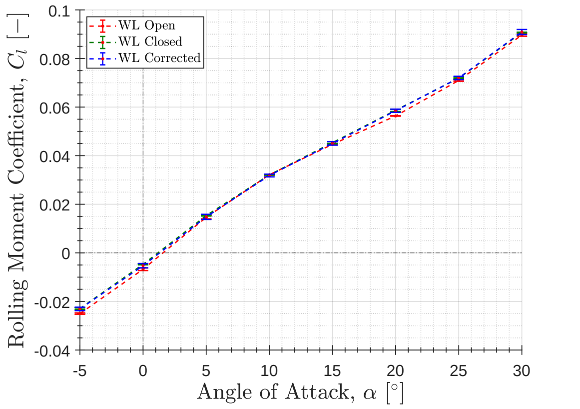

(b) Open, Corrected and Closed Rolling Moment Coefficient with 95% Confidence Intervals. Left Wing Only Results. $\overline{\delta}_{\mathrm{CS1}} = \overline{\delta}_{\mathrm{CS2}} = \overline{\delta}_{\mathrm{CS3}} = 0\%$, $\overline{\delta}_{\mathrm{R}} = 0\%$.

Figure A.5: Side-Force and Rolling Moment Coefficients Before and After Correcting. $\overline{\delta}_{\mathrm{CS1}} = \overline{\delta}_{\mathrm{CS2}} = \overline{\delta}_{\mathrm{CS3}} = 0\%$, $\overline{\delta}_{\mathrm{R}} = 0\%$.

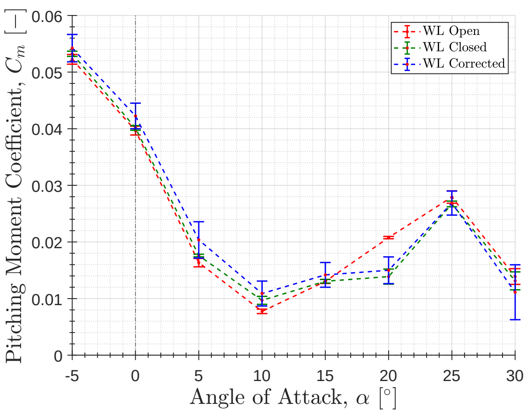

(a) Open, Corrected and Closed Pitching Moment Coefficient with 95% Confidence Intervals. Dual-Wing Results. $\overline{\delta}_{\mathrm{CS1}} = \overline{\delta}_{\mathrm{CS2}} = \overline{\delta}_{\mathrm{CS3}} = 0\%$, $\overline{\delta}_{\mathrm{R}} = 0\%$.

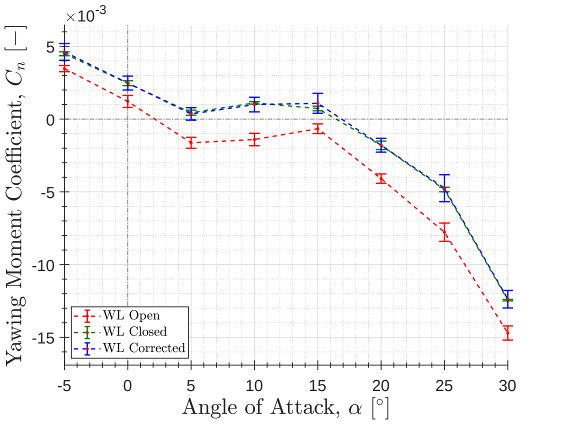

(b) Open, Corrected and Closed Yawing Moment Coefficient with 95% Confidence Intervals. Left Wing Only Results. $\overline{\delta}_{\mathrm{CS1}} = \overline{\delta}_{\mathrm{CS2}} = \overline{\delta}_{\mathrm{CS3}} = 0\%$, $\overline{\delta}_{\mathrm{R}} = 0\%$.

Figure A.6: Pitching and Yawing Moment Coefficients Before and After Correcting. $\overline{\delta}_{\mathrm{CS1}} = \overline{\delta}_{\mathrm{CS2}} = \overline{\delta}_{\mathrm{CS3}} = 0\%$, $\overline{\delta}_{\mathrm{R}} = 0\%$.

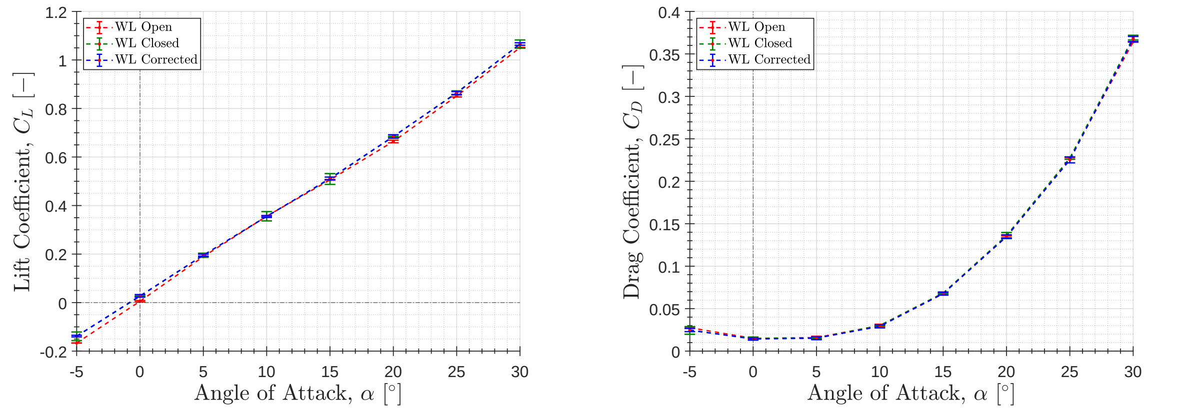

(a) Open, Corrected and Closed Lift Coefficient with 95% Confidence Intervals. Dual-Wing Results. $\overline{\delta}_{\mathrm{CS1}}$ = $\overline{\delta}_{\mathrm{CS2}}$ = $\overline{\delta}_{\mathrm{CS3}}$ = +50%, $\overline{\delta}_{\mathrm{R}}$ = 0%.

(b) Open, Corrected and Closed Drag Coefficient with 95% Confidence Intervals. Dual-Wing Results. $\overline{\delta}_{\mathrm{CS1}}$ = $\overline{\delta}_{\mathrm{CS2}}$ = $\overline{\delta}_{\mathrm{CS3}}$ = +50%, $\overline{\delta}_{\mathrm{R}}$ = 0%.

Figure A.7: Lift and Drag Coefficients Before and After Correcting. $\overline{\delta}_{\mathrm{CS1}}$ = $\overline{\delta}_{\mathrm{CS2}}$ = $\overline{\delta}_{\mathrm{CS3}}$ = +50%, $\overline{\delta}_{\mathrm{R}}$ = 0%.

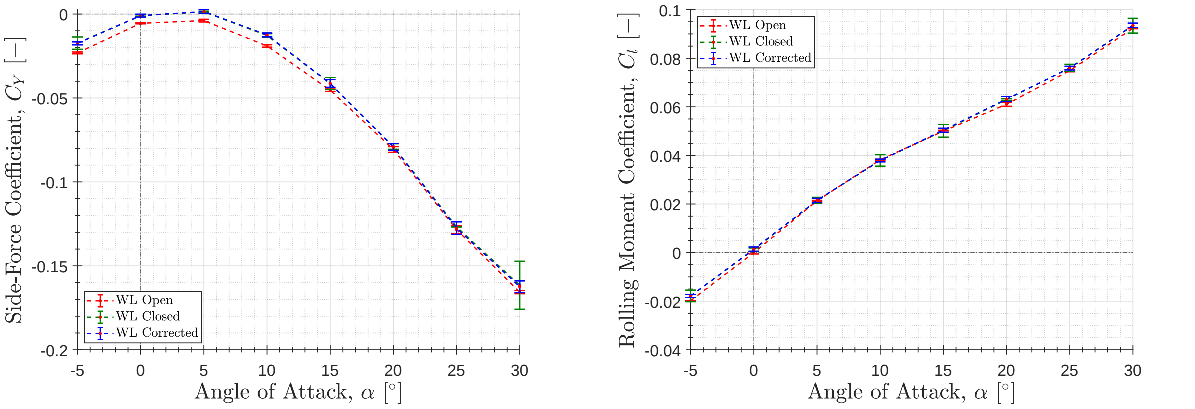

(a) Open, Corrected and Closed Side-Force Coefficient with 95% Confidence Intervals. Left Wing Only Results. $\overline{\delta}_{\mathrm{CS1}}$ = $\overline{\delta}_{\mathrm{CS2}}$ = $\overline{\delta}_{\mathrm{CS3}}$ = +50%, $\overline{\delta}_{\mathrm{R}}$ = 0%.

(b) Open, Corrected and Closed Rolling Moment Coefficient with 95% Confidence Intervals. Left Wing Only Results. $\overline{\delta}_{\mathrm{CS1}}$ = $\overline{\delta}_{\mathrm{CS2}}$ = $\overline{\delta}_{\mathrm{CS3}}$ = +50%, $\overline{\delta}_{\mathrm{R}}$ = 0%.

Figure A.8: Side-Force and Rolling Moment Coefficients Before and After Correcting. $\overline{\delta}_{\mathrm{CS1}}$ = $\overline{\delta}_{\mathrm{CS2}}$ = $\overline{\delta}_{\mathrm{CS3}}$ = +50%, $\overline{\delta}_{\mathrm{R}}$ = 0%.

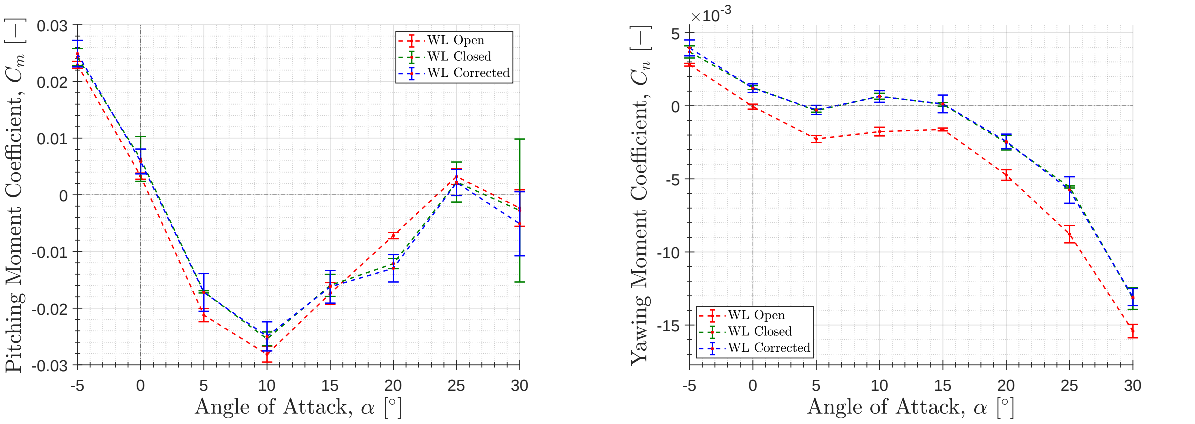

(a) Open, Corrected and Closed Pitching Moment Coefficient with 95% Confidence Intervals. Dual-Wing Results. $\overline{\delta}_{\mathrm{CS1}}$ = $\overline{\delta}_{\mathrm{CS2}}$ = $\overline{\delta}_{\mathrm{CS3}}$ = +50%, $\overline{\delta}_{\mathrm{R}}$ = 0%.

(b) Open, Corrected and Closed Yawing Moment Coefficient with 95% Confidence Intervals. Left Wing Only Results. $\overline{\delta}_{\mathrm{CS1}}$ = $\overline{\delta}_{\mathrm{CS2}}$ = $\overline{\delta}_{\mathrm{CS3}}$ = +50%, $\overline{\delta}_{\mathrm{R}}$ = 0%.

Figure A.9: Pitching and Yawing Moment Coefficients Before and After Correcting. $\overline{\delta}_{\mathrm{CS1}}$ = $\overline{\delta}_{\mathrm{CS2}}$ = $\overline{\delta}_{\mathrm{CS3}}$ = +50%, $\overline{\delta}_{\mathrm{R}}$ = 0%.

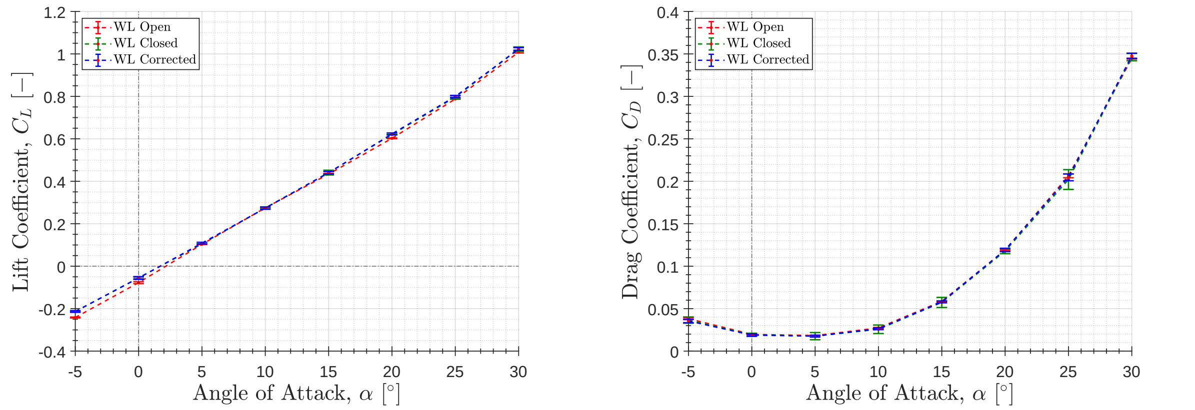

(a) Open, Corrected and Closed Lift Coefficient with 95% Confidence Intervals. Dual-Wing Results. $\overline{\delta}_{\mathrm{CS1}} = \overline{\delta}_{\mathrm{CS2}} = \overline{\delta}_{\mathrm{CS3}} = -50\%$, $\overline{\delta}_{\mathrm{R}} = 0\%$.

(b) Open, Corrected and Closed Drag Coefficient with 95% Confidence Intervals. Dual-Wing Results. $\overline{\delta}_{\mathrm{CS1}} = \overline{\delta}_{\mathrm{CS2}} = \overline{\delta}_{\mathrm{CS3}} = -50\%$, $\overline{\delta}_{\mathrm{R}} = 0\%$.

Figure A.10: Lift and Drag Coefficients Before and After Correcting. $\overline{\delta}_{\mathrm{CS1}} = \overline{\delta}_{\mathrm{CS2}} = \overline{\delta}_{\mathrm{CS3}} = -50\%$, $\overline{\delta}_{\mathrm{R}} = 0\%$.

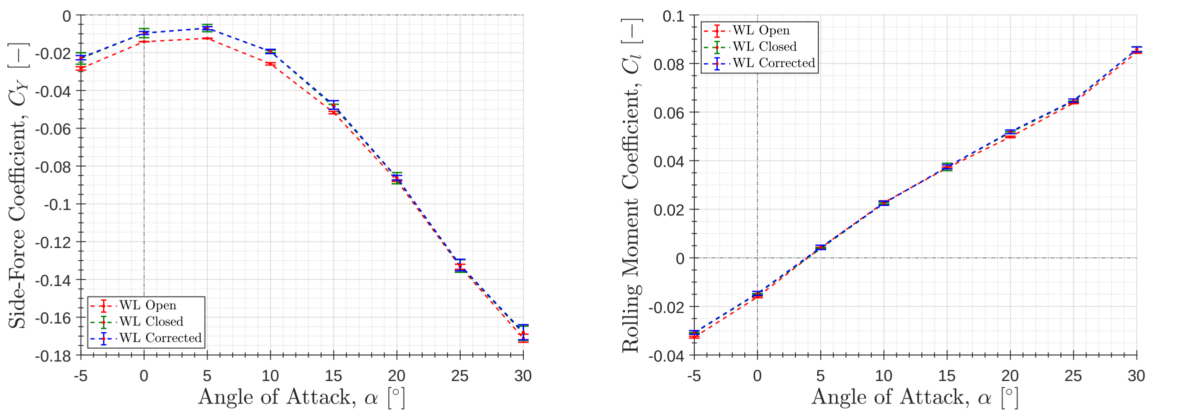

(a) Open, Corrected and Closed Side-Force Coefficient with 95% Confidence Intervals. Left Wing Only Results. $\overline{\delta}_{\mathrm{CS1}} = \overline{\delta}_{\mathrm{CS2}} = \overline{\delta}_{\mathrm{CS3}} = -50\%$, $\overline{\delta}_{\mathrm{R}} = 0\%$.

(b) Open, Corrected and Closed Rolling Moment Coefficient with 95% Confidence Intervals. Left Wing Only Results. $\overline{\delta}_{\mathrm{CS1}} = \overline{\delta}_{\mathrm{CS2}} = \overline{\delta}_{\mathrm{CS3}} = -50\%$, $\overline{\delta}_{\mathrm{R}} = 0\%$.

Figure A.11: Side-Force and Rolling Moment Coefficients Before and After Correcting. $\overline{\delta}_{\mathrm{CS1}} = \overline{\delta}_{\mathrm{CS2}} = \overline{\delta}_{\mathrm{CS3}} = -50\%$, $\overline{\delta}_{\mathrm{R}} = 0\%$.

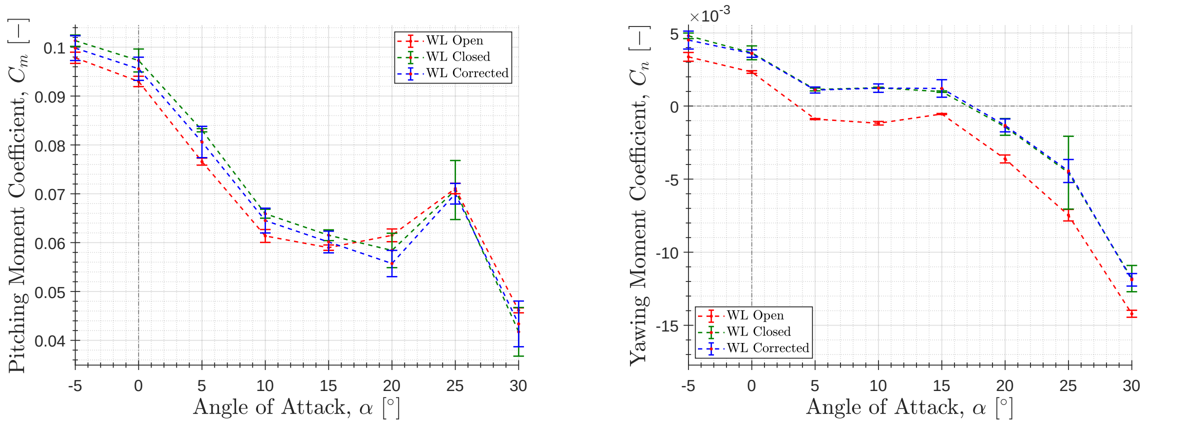

(a) Open, Corrected and Closed Pitching Moment Coefficient with 95% Confidence Intervals. Dual-Wing Results. $\overline{\delta}_{\mathrm{CS1}} = \overline{\delta}_{\mathrm{CS2}} = \overline{\delta}_{\mathrm{CS3}} = -50\%$, $\overline{\delta}_{\mathrm{R}} = 0\%$.

(b) Open, Corrected and Closed Yawing Moment Coefficient with 95% Confidence Intervals. Left Wing Only Results. $\overline{\delta}_{\mathrm{CS1}} = \overline{\delta}_{\mathrm{CS2}} = \overline{\delta}_{\mathrm{CS3}} = -50\%$, $\overline{\delta}_{\mathrm{R}} = 0\%$.

Figure A.12: Pitching and Yawing Moment Coefficients Before and After Correcting. $\overline{\delta}_{\mathrm{CS1}} = \overline{\delta}_{\mathrm{CS2}} = \overline{\delta}_{\mathrm{CS3}} = -50\%$, $\overline{\delta}_{\mathrm{R}} = 0\%$.

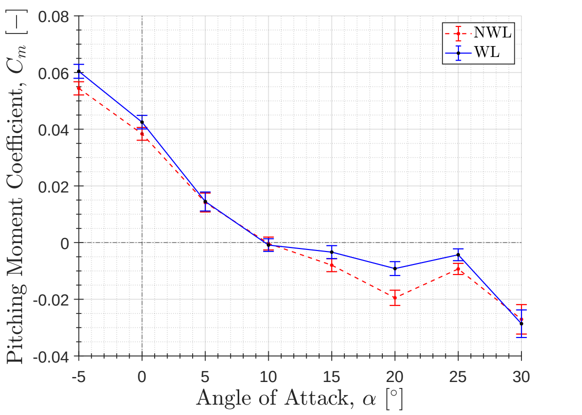

(a) Flying V Model Pitching Moment Coefficient Before and After WLI with 95 % Confidence Intervals. Corrected Dual-Wing Results. x_{MR} = 1.33 m.

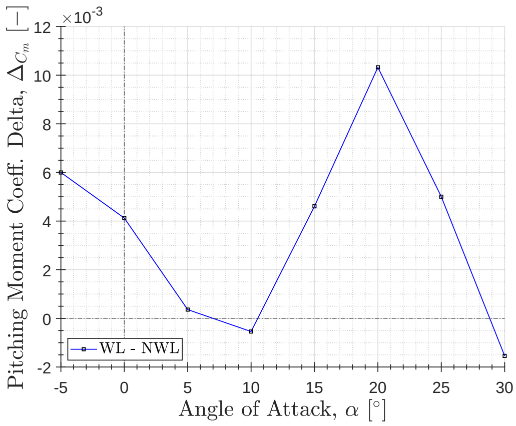

(b) Flying V Model Pitching Moment Coefficient Delta Due to WLI. Corrected Dual-Wing Results. x_{MR} = 1.33 m.

Figure A.13: Winglet Integration Effects on Pitching Moment Coefficient. Both Results are Corrected According to Section 3.1. x_{MR} = 1.33 m.

B

Additional Photos

In this Appendix, additional photos are given which have been briefly mentioned in the main matter of this report.

B.1. Gaps in Reflection Plate

The front and rear gaps in the reflection plate are shown in Figures B.1 and B.2, respectively. The effects of these holes have been covered in Section 3.1.

Figure B.1: Photo of the Front Gap in the Reflection Plate Before Closure. The Gap is Circled in Red Which Also Shows the Exposed Aluminum Attachment Plate.

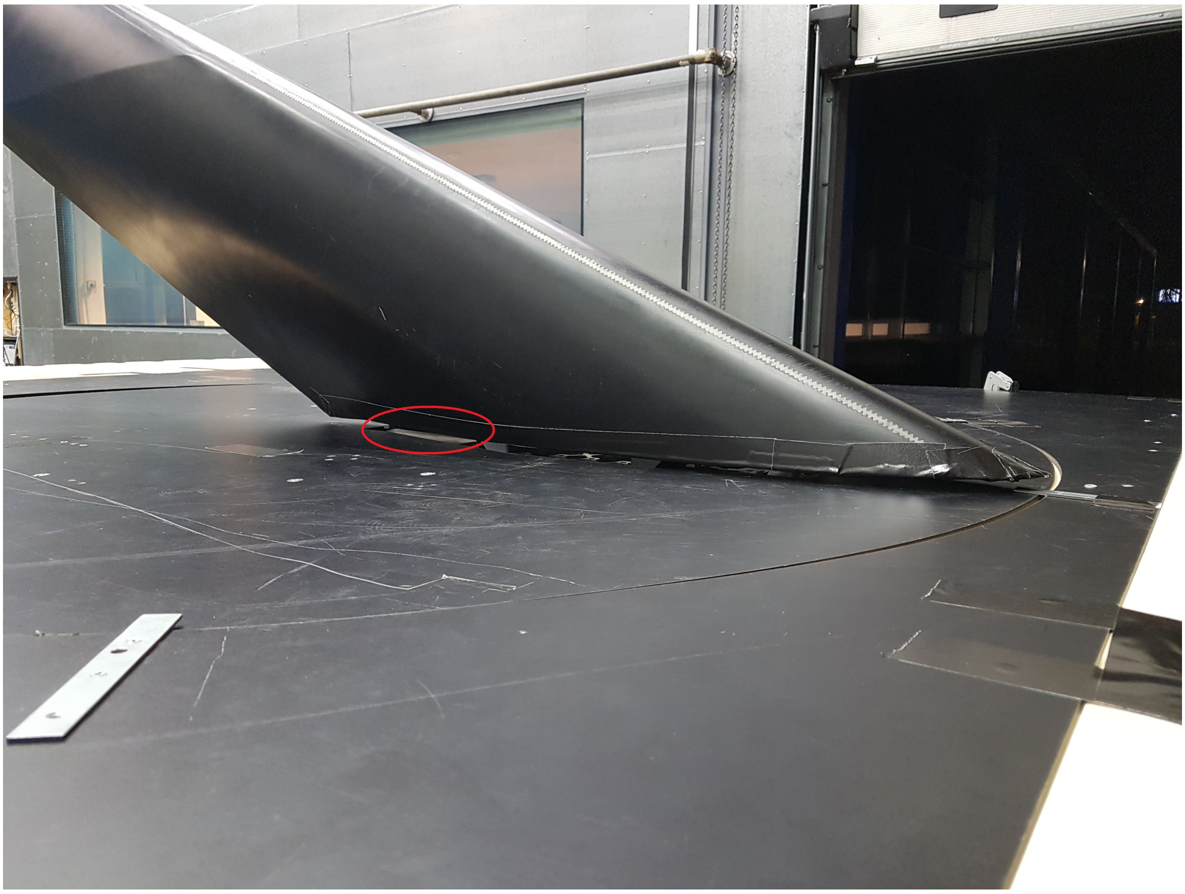

Figure B.2: Photo Showing the Closed Rear Gap in the Reflection Plate. The Area That was Closed is Circled in Red. The Boikon Connection Structure is Just Ahead of This.